

December 2019

Underwater Particle Image Velocimetry (PIV) Measurement of Turbulence Over Mussel Bed in a Deepsite of Lake Michigan

Tong Jin
University of Wisconsin-Milwaukee

Follow this and additional works at: <https://dc.uwm.edu/etd>



Part of the [Civil Engineering Commons](#), and the [Environmental Engineering Commons](#)

Recommended Citation

Jin, Tong, "Underwater Particle Image Velocimetry (PIV) Measurement of Turbulence Over Mussel Bed in a Deepsite of Lake Michigan" (2019). *Theses and Dissertations*. 2313.
<https://dc.uwm.edu/etd/2313>

This Dissertation is brought to you for free and open access by UWM Digital Commons. It has been accepted for inclusion in Theses and Dissertations by an authorized administrator of UWM Digital Commons. For more information, please contact open-access@uwm.edu.

UNDERWATER PARTICLE IMAGE VELOCIMETRY(PIV)
MEASUREMENT OF TURBULENCE OVER MUSSEL BED IN A DEEPSITE OF LAKE
MICHIGAN

by

Tong Jin

A Dissertation Submitted in
Partial Fulfillment of the
Requirements for the Degree of

Doctor of Philosophy
in Engineering

at

The University of Wisconsin-Milwaukee

December 2019

ABSTRACT

UNDERWATER PARTICLE IMAGE VELOCIMETRY(PIV) MEASUREMENT OF TURBULENCE OVER MUSSEL BED IN A DEEPSITE OF LAKE MICHIGAN

by

Tong Jin

The University of Wisconsin-Milwaukee, 2019
Under the Supervision of Associate Professor Qian Liao

The influence of the benthic filter feeders, such as bivalves, on ecosystem plankton, and nutrient dynamics is considered significant in shallow marine and freshwater systems. Recent indirect evidence showed that the profundal quagga mussels (*Dreissena rostriformis bugensis*) have fundamentally altered energy flow and dynamics of nutrients and phytoplankton in Lake Michigan and other Great Lakes. To investigate the phytoplankton grazing rate of the quagga mussel and the mussel siphon currents induced bio-mixing, a self-contained *in situ* Underwater Particle Image Velocimetry was developed to measure the turbulence structure and the turbulent diffusion coefficient immediately above the profundal quagga mussel covered substrate in the deep-water site located in Lake Michigan. The system was deployed from July to October 2018, and 500 sets of datasets were acquired with 400 snaps of 2D velocity and particle concentration maps for each set. The diffusion coefficients were estimated and compared from multiple methods with measurements of turbulence and particle density. Field data analysis suggested that in the low energetic deep lake benthic boundary, mussels' siphon currents are the major source of turbulence. Turbulent diffusivity/viscosity varied between 10^{-6} to 10^{-5} ($m^2 s^{-1}$), which seemed

to correlate with the ambient particle concentration. Collective pumping rates of mussels were also estimated from measured near-bed turbulent flux of particles. Data also showed that near-bed turbulent diffusivity increases linearly with mussels' pumping rate. This empirical linear relation was applied to a one-D numerical model. Simulation results proved the hypothesis that profundal mussels can maximize their grazing efficiently by the enhanced near-bed turbulence due to siphon currents. Modeling simulation also suggested that an optimal collective pumping rate may exist, which varied between about 1 to 5 liters per day per individual, depending on the ambient mixing condition.

© Copyright by Tong Jin, 2019
All Rights Reserved

To
my wife
Lingling Yang

TABLE OF CONTENTS

	Page
ABSTRACT.....	ii
TABLE OF CONTENTS.....	vi
LIST OF TABLES.....	viii
LIST OF FIGURES.....	ix
ACKNOWLEDGMENTS.....	xiii
Chapter 1. Introduction.....	1
1.1 Background and Motivation.....	1
1.2 Documented mussel mixing studies and hypotheses.....	5
1.3 Particle Image Velocimetry (PIV) and Underwater PIV(UW-PIV).....	7
1.4 Structure of the thesis.....	11
Chapter 2. Methods.....	13
2.1 Instrumentation: an Underwater-Particle Image Velocimetry (UW-PIV) system.....	13
2.2 Components of the UW-PIV system.....	16
2.3 Deployment locations and timings.....	19
2.4 Companion measurements, Micro-profile coupled with PIV.....	25
2.5 PIV interrogation and post-processing.....	26
2.6 Analysis of particle concentration data.....	29
Chapter 3. Measurement results and data analysis.....	33
3.1 The uncertainties of the mean flow direction and instrument perturbation.....	33
3.2 Turbulent diffusivity estimation.....	39
3.2.1 Direct method.....	39
3.2.2 Reynolds averaging method (Covariance method).....	39
3.2.3 k-epsilon method.....	40
3.3 TKE and Reynolds stress estimation.....	41
3.3.1 Random wave-induced fluctuation removal.....	41
3.3.2 Low-pass filtering method.....	42
3.3.2.1 Data processing procedures.....	45
3.3.3 Second-order structure function method.....	46
3.3.4 Correlation analysis.....	52
3.3.4.1 Turbulent kinetic energy (TKE) calculation.....	52
3.4 TKE dissipation rate estimation.....	58
3.4.1 Direct method.....	59

3.4.2	Linear-Fit in Inertial Subrange of a 1-D Velocity Spectra	60
3.4.3	Structure-function fitting method	62
3.4.4	Large Eddy PIV method	63
3.4.5	Comparison and conclusion	66
3.5	Results and correlation analysis of turbulent diffusivity	72
3.5.1	Time series result and data selection	72
3.5.2	Analysis of the selected data	74
3.5.3	Filtration rate of mussels	77
Chapter 4.	Testing Hypotheses with Modeling Analysis	80
4.1	One D advection-diffusion model for phytoplankton transport.....	80
4.2	Analytical framework with constant diffusivity	81
4.2.1	Boundary conditions considering mussels' grazing	81
4.2.2	Analytical solution with constant diffusivity and finite water depth	83
4.3	Enhanced Mussel Grazing due to Bio-Mixing: A Numerical Modeling Test	88
4.4	Soluble reactive phosphorus flux estimation	95
Chapter 5.	Conclusions.....	99
BIBLIOGRAPHY		103
APPENDIX. Selected time Interval.....		108
Curriculum Vitae		110

LIST OF TABLES

Table	Page
Table 2.1 UWPIV hardware list.....	19
Table 2.2 Deployment sites information.....	21
Table 2.3 UW-PIV deployment date	24
Table 3.1 List of the slopes of the linear regression in Figure 3.10.....	53
Table 4.1 Optimal mussel pumping rate under different background diffusivity and the corresponding grazing efficiency.....	94
Table 4.2 SRP flux estimation from PIV and microprofiler measurements. Estimated SRP fluxes on 8/23/19 and 7/11/19 were averaged between two replicate deployed microprofilers.	97

LIST OF FIGURES

Figure	Page
Figure 1.1 Quagga mussel, from NOAA website(Glassner-Shwayder and Myers, n.d.).	3
Figure 1.2 Literature review of the underwater PIV	9
Figure 2.1 Structural configuration of the Underwater PIV system.	15
Figure 2.2 The dimensions of the UW-PIV frame.	15
Figure 2.3 Particle images captured during daytime and night.	16
Figure 2.4 Inside the Camera-Computer unit.	18
Figure 2.5 UW-PIV synchronization signal flow chart	18
Figure 2.6 Profundal mussel density in 55m site of Lake Michigan, Photo from Bootsma Team, UWM	20
Figure 2.7 UW-PIV deployment locations.	21
Figure 2.8 Deploying UW-PIV on Lake Michigan.	22
Figure 2.9 Histogram of the velocity measured by an ADV at the height of 25cm above the lake bottom.	23
Figure 2.10 Sample images of deployments.	25
Figure 2.11 The membrane tube attached in the UWMPIV frame	26
Figure 2.12 An example of PIV pre-process, interrogation result and post-process (adaptive median test) result.	28
Figure 2.13 An example that illustrates the particle identification algorithm.	31
Figure 2.14 The particle counting results	32
Figure 3.1 Near bottom velocity distribution measured by ADV (Acoustic Doppler Velocimeter) on the site of AW55 in August 2017.	34
Figure 3.2 Histogram of the velocity magnitude from ADCP measurement, Aug 2017.	35
Figure 3.3 Time series of the streamwise velocity at $z = 5\text{cm}$.	37

Figure 3.4 Velocity spectrum analysis of the velocities on Figure 3.3	38
Figure 3.5 Time series of the streamwise velocity at $z = 5$ cm from data set AW55-0023.....	42
Figure 3.6 Reynolds normal stress calculated from mean velocity and low pass velocity.....	44
Figure 3.7 Lowpass method data processing steps	46
Figure 3.8 Structure function Dr_1 at $z = 3$ cm, 4cm, 6cm and 8cm.	49
Figure 3.9 (a)(b) Reynolds normal stress and (c) Reynolds shear stress by second-order structure function method and the lowpass filter method.	51
Figure 3.10 TKE comparison of the lowpass filter method and the structure function method, (a) lowpass filter =1, (b) lowpass filter = 5, (c) lowpass filter = 9, (d) lowpass filter = 11.	54
Figure 3.11 Reynolds shear stress comparison of the lowpass filter method and the structure function method.....	56
Figure 3.12 Particle concentration flux $w'c'$ estimation comparison of the lowpass filter method and the structure function method.	57
Figure 3.13 (a) TKE dissipation rate calculated by Hinze's direct method. (b) TKE dissipation rate calculated by Doron's direct method. The dataset is AW55-0023.	60
Figure 3.14 Spatial spectral analysis of the velocity.....	61
Figure 3.15 log linear fitting of the velocity spectrum.	61
Figure 3.16 Ratio of the linear fitting methods by horizontal and vertical velocity spectrum.	62
Figure 3.17 Secondary structure-function and the linear fit of the $\log D_{11}$ and $\log(r_{11})$	63
Figure 3.18 Distribution of TKE dissipation rate ϵ_{LEP}	66
Figure 3.19 Dissipation rate estimation difference between the two direct methods	67
Figure 3.20 Dissipation rate estimation comparison between the direct method and LEP method	68
Figure 3.21 Comparison of the direct method and the SF11method	69
Figure 3.22 Comparison of the direct method and the LF33 method.....	70
Figure 3.23 Comparison of the direct method and the SF method	71
Figure 3.24 Comparison of the LEP method and the LF11 method.....	71

Figure 3.25 Time series of results.....	74
Figure 3.26 Comparison of the turbulent viscosity and turbulent diffusivity.....	75
Figure 3.27 Comparison of the mean velocity and the turbulent diffusivity.....	76
Figure 3.28 Comparison of the particle concentration and the eddy viscosity.....	77
Figure 3.29 Time series of estimate mussel collective pumping rate (converted to m/day) and near-bed diffusivity.....	78
Figure 3.30 Correlation between turbulent diffusivity and mussels' collective pumping rate. Dashed lines and equations in the figure represent linear regression of $DT = \gamma Q$	79
Figure 3.31 Correlation between turbulent viscosity and mussels' collective pumping rate. Dashed lines and equations in the figure represent linear regression of $vT = \gamma Q$	79
Figure 4.1 Illustration of mussel "porosity" β , which represents the fraction of total areas of mussels' incurrent siphons per unit area of the lake bottom. Parameter $\alpha \equiv 1-\beta$ thus represents the fraction of areas including the lakebed sediment and mussel shells (minus incurrent siphons).....	83
Figure 4.2 Analytical solution of phytoplankton concentration profiles in a 1-meter water column under varying ambient mixing coefficient D and mussels' collective pumping rate Q	85
Figure 4.3 Mussels' grazing efficiency as a function of pumping rate and background turbulent diffusivity. Here the efficiency was defined as the ration of grazing rate QCB to the passive settling $wsCH$	87
Figure 4.4 Illustration of the one-d FVM grid structure.	89
Figure 4.5 Illustration of the "four layers" structure.....	90
Figure 4.6 Results of numerical simulation for the phytoplankton concentration profile (left) and grazing rate (right) with varying collective pumping rate (Q) and background diffusivity (DB), with and without bio-mixing effects (i.e., $Dsiphon$). Solid and colored lines represent concentration profiles with bio-mixing under different pumping rates. Dashed and colored lines are those without bio-mixing. The difference in Q is represent by different colors.....	93
Figure 4.7 Profiles of SRP from microprofiler measurement (circles) and from model solution (solid line), with the SRP flux FDP and bottom concentration $CDP0$ estimated with nonlinear fitting. Distribution of diffusivity $D(z)$ is modeled with average diffusivity measured by PIV during the same time period of SPR microprofiling measurements.....	97
Figure 4.8 Profiles of SRP from microprofiler measurement (circles) and from model solution (solid line), with the SRP flux FDP, bottom concentration $CDP0$ and the diffusivity Dz all	

estimated with nonlinear fitting, since PIV data were not available during the
microprofiling measurements.97

Figure 4.9 Estimated SRP flux vs collected mussel pumping rate according to PIV and microprofiler
measurements on 7/31/18, 8/16/18 and 8/23/18.98

ACKNOWLEDGMENTS

It is a great pleasure to acknowledge my deepest thanks gratitude to my advisor Professor Qian Liao, for the continuous support of my Ph.D. study and related research, for his patience, motivation, and immense knowledge. His guidance helped me in all the time of research and writing of this thesis. I could not have imagined having a better advisor and mentor for my Ph.D study. It would be never too much to express my gratitude for his help. I have learned so much from him as a scientist and a professional.

Many thanks to the Professor Harvey Bootsma, without him, I can never finish the field experiments. He provided me with so many insights and guidance on my research work. Thank you so much to the other committee members, Professor Hector Bravo, Professor Yin Wang and Professor Zeyun Yu who provided a lot of comments and suggestion to better my work.

I am so grateful to my collaborators in this project, Rae-Ann MacLellan-Hurd, and David. Cannon. Thank you for helping me in the field works, and it was a great pleasure to work with you. I also want thank the crews of the R/V *Neeskay* and the team of Harvey Bootsma for the help with field experiments.

I am so grateful to my colleagues in Environmental Hydraulics Lab, Dr. Chunqi Sheng, Dr. Wei Li, and Dr. Liuhong Chang , for their companion and help on the work.

At last, I would like to thank my parents and my wife Lingling Yang, without your supports, I will not be able to finish the study. I love you!

CHAPTER 1. INTRODUCTION

1.1 Background and Motivation

During the past several decades, the Dreissenid mussels continue to spread in the Great Lakes and have successfully established a large population in the most bottom areas (Fahnenstiel et al., 2010b; Karatayev et al., 2015). Two invasive dreissenid mussels (i.e., zebra and quagga mussels), were major focus of research at Great Lakes region during past decades (Ackerman et al., 2001; Fanslow et al., 1995; Nalepa et al., 2009). Zebra mussel and quagga mussel spread from Europe to the Great Lakes in the late 1980s and early 1990s, zebra mussels first dominate the shallow rocky nearshore region while quagga mussels restricted to the offshore deep waterbed due to the better tolerance of cold water and less food. Quagga mussel can survive in the deepwater because of the tolerance of low temperature (around 4 °C) (Baldwin et al., 2002), ability to survive in most surfaces of deep site (Cuhel and Aguilar, 2013), and the lower metabolic rate (Stoeckmann, 2003). Zebra mussels had been displaced by quagga mussels in most benthos of the Great Lakes in recent decades (Nalepa et al., 2010).

The quagga mussel has a high filtering rate compared to its size, and coupled with its high density in the Great Lakes, has a significant impact in the ecosystem. G. Fahnenstiel et al. analyzed the data sampled in the past 30 years at two offshore sites of south Lake Michigan and found that the phytoplankton depletion was related to the mussel density, the large decrease (66-87%) of phytoplankton occurred in 2007-2008 compared to 1995-1998 and 1983-1987. He also predicted that the changes of phytoplankton communities will change while the profundal mussel density turns to be stable (Fahnenstiel et al., 2010b). Kerfoot et al. (Kerfoot et al., 2008) also

found a large decrease in chlorophyll in the offshore region, which confirmed with the result published by Fahnenstiel. Fahnenstiel summarized the related papers and concluded that the lower food web of the Lake Michigan and the other Great Lakes has been significantly altered by the invasion of the mussels (Fahnenstiel et al., 2010a).

Figure 1.1 shows the picture of a quagga mussel in the clear water tank, the picture was downloaded from the NOAA website. The two tubes that protrude from the mussel shell are siphons, which are mainly used to inhale water containing food and exhale the filtered water. The mussel uses hair-like cilia on its gills to pull water containing impurities into its shell through the inhalant siphon, the collected impurities which can be easily ingest are then selected for ingestion inside, and the impurities which are hard for ingest or toxic are then rejected through the siphon. The current, moves over the gills, also utilized for respiration, can provide oxygen for the mussels. The filtered water then expelled via the exhalant siphon to the higher levels of the water body for avoiding the contamination of the food source. The expelled filtered water contains higher value of dissolved phosphorus (after digestion) and a lower value of dissolved oxygen (by respiratory). As showing in , the inhalant siphon is longer than the exhalant siphon, the long siphon could let the mussel to access higher water level with higher food abundance.

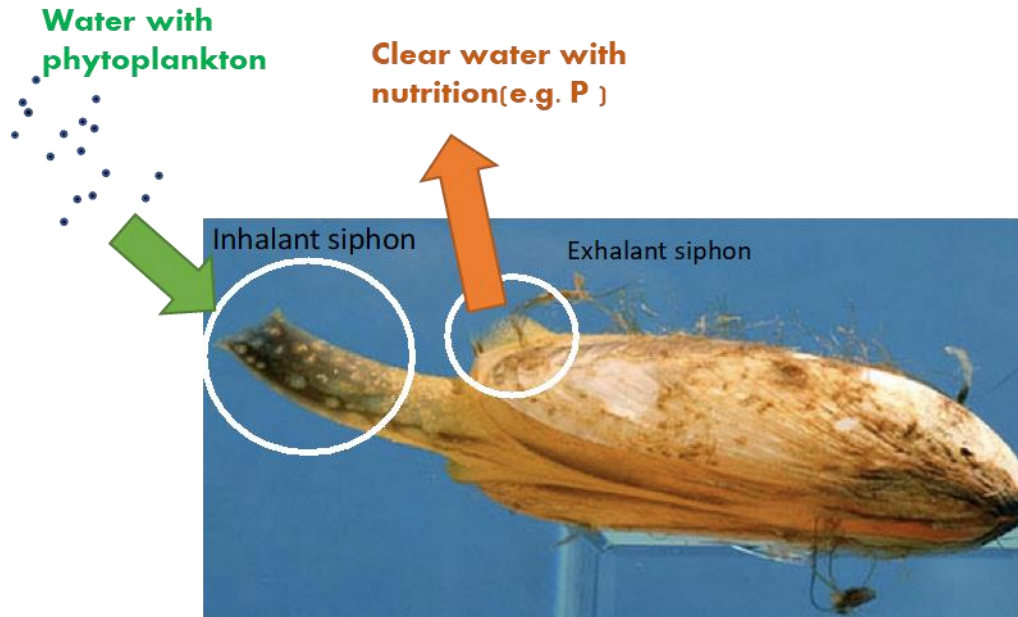


Figure 1.1 Quagga mussel, from NOAA website(Glassner-Shwayder and Myers, n.d.).

Studies of impacting of dreissenid mussels to the eco-system of the Great Lakes were mainly focused on the mussels impact on the shallow nearshore areas, where they have been found with more dense population (Qualls et al., 2007; Vanderploeg et al., 2009) back then and the vertical mixing is sufficient to let the mussel grazing accessing the whole water column in the shallow-water areas. Hecky introduced the hypothetical construct of “nearshore shunt” that the phytoplankton harvested by the nearshore mussels might originated partly in the offshore water that transferred by advection (Hecky et al., 2004). Karatayev (Karatayev et al., 2018) found that profundal habitant quagga mussel may have very limited impacts on the ecosystem due to both severe food depletion and cold temperature.

However, Mosley argued that profunda quagga mussels in offshore still played an important role due to the much greater distribution in the whole lake. The recent studies have provided indirect evidence that the quagga mussels have fundamentally changed the dynamics of nutrients and phytoplankton in Lake Michigan and other Great Lakes (Mida et al., 2010;

Turschak and Bootsma, 2015). There are some papers applying numerical methods in the phytoplankton research (Bravo et al., 2019; Rowe et al., 2017, 2015; Shen et al., 2018). Rowe et al. built the FVCOM modeling analysis and found that the quagga mussels have had a significant influence to the ecosystem that both the spatial and temporal distribution of phytoplankton abundance were altered by the mussel grazing (Rowe et al., 2017, 2015). Mosley (Mosley and Bootsma, 2015) measured and found that the profundal quagga mussel phosphorus grazing rate is several times larger than the phosphorus passive settling, and suggest that passive settling is no longer the primary mechanism to deliver phytoplankton to the bottom. If this indeed the case, the accelerated delivery rate to the lakebed is caused by the joint impact from the depletion of phytoplankton density by mussel grazing and the transport of the Benthic boundary layer by vertical mixing. Bootsma et al. suggested that more observational data need to be measured for calibrating the models by the changes of the situation (Bootsma et al., 2015).

1.2 Documented mussel mixing studies and hypotheses

Because the activities of the mussels are highly limited by the local mixing of the Bottom Boundary Layer (BBL) (Ackerman et al., 2001), a variety of studies have been conducted to study the effect of benthic bivalves on the mixing of BBL. The majority of these works were carried out in simulated laboratory settings or Computational Fluid Mechanics (CFD).

Some works indicate that the bottom roughness element increase on BBL hydrodynamics due to the patch of bivalves (Ciutat et al., 2007; Folkard and Gascoigne, 2009; Quinn and Ackerman, 2015; van Duren et al., 2006). Ciutat performed a flume experiment and found that the patch of the bivalves increased the Reynolds shear stress and further enhanced the sediment disturbance and resuspension (Ciutat et al., 2007). Folkard studied the heterogeneous arrangements of mussel patches, the results implied that the increase of the patch gaps enhanced the near bottom TKE (Folkard and Gascoigne, 2009).

Some other works indicate that the exhalant jet from the mussels contains momentum that can enhance turbulent mixing at BBL (Lassen et al., 2006; Nishizaki and Ackerman, 2017; Riisgård and Larsen, 2017; Widdows et al., 2009). Lassen performed the experiment in the flume with mussel activities triggered by the concentration of the phytoplankton, the result shows that the mussel activities enhanced the near-bottom turbulent mixing not only for the slow flow but also the fast flow. But Duren conducted a similar experiment with the result that the enhancement of turbulent mixing is significant only when the flow velocity is low. H F E Jones et al. found that the bed shear stress was enhanced with the bivalve activity (*Austrovenusstutchburyi*) at three different background current speeds, with the enhancement ratio decreased with the increase of current in their laboratory experiment (Jones et al., 2011). Nishizaki applied Particle Image Velocimetry(PIV) observation in the lab around mussel

aggregations, the result from the flow visualization indicated that the siphonal jets can increase mixing around and above the aggregations in the low flow condition (Nishizaki and Ackerman, 2017).

In sum, the mussel patch and the siphonal jets both enhanced the turbulent mixing immediately above the bottom. The enhancement from the bottom roughness depended on the ambient velocity. When the enhancement from the bottom roughness decreases as the velocity decreases, the part from the siphonal jet will become significant compared to the bottom roughness.

From the conclusions from the literature listed above, the exhalant jets of mussel may support higher productivity at low-speed flows, which indicates that the mussel exhalant jet may be the main source of the turbulent mixing in the deep water with the low-speed condition. Thus, we hypothesize that profundal mussels can enhance near-bed turbulence due to siphonal currents, thereby maximizing food capture rate by keeping particles in suspension in a thin layer immediately above the mussel bed in the low energy flow condition.

The objectives of the thesis are to quantify the impact of the profundal mussel activities on the eco-system of Lake Michigan during the summertime, when the study site was in the stratified period of the lake, the bottom of the study site is in low energy states without strong ambient turbulence. The goal is to resolve the high-resolution vertical structures of mean flow, Reynolds shear stress, turbulent intensity, eddy viscosity/diffusivity and other statistics of turbulence that response to the mussel patches and filtration effect.

To address the hypotheses and reach the goal above, a new designed in-situ Underwater Particle Image Velocimetry (UWPIV) was deployed at the bottom of Lake Michigan routinely through the summer of 2018 to the fall of 2019. with hydrodynamics measurement and particle

concentration analysis, the UWPIV could extract turbulent structure and phytoplankton concentration immediately above the mussel colonies with high spatial and temporal resolution.

1.3 Particle Image Velocimetry (PIV) and Underwater PIV(UW-PIV)

Human eyes are exceptionally well adapted to recognize moving things, which by evolutionary theory, can capture food and avoid vulnerability. One can throw a piece of a tree branch to a river surface to evaluate the velocity of the running water and detect the flow structures. Followed by this idea, scientists in the 19th century used particles as the tracer to visualize turbulence in fluid in flumes and wind tunnels with photography (Raffel et al., 1998), however, quantitative data could not be obtained during that time. Thanks to the advances of the digital image recording and processing techniques which replaced the analog techniques, image-based velocity measurement techniques like Particle Image Velocimetry (PIV) or Particle Tracking Velocimetry (PTV) have become increasingly popular for quantitative flow visualization in fluid mechanics in the last three decades.

PIV can obtain instantaneous velocity distributions and related properties in fluids by the image pairs of particles which suspended in the fluid. Compare to standard measurement techniques such as Hot Wire Anemometry (HWA) and Laser Doppler Velocimeter (LDV) which only allow to extract the flow velocity at a single point, PIV can extract information about the spatial organization of the flow, which can satisfy the requirement of spatial statistical methods (Adrian, 2005; Raffel et al., 2017; Willert and Gharib, 1991), and offers the capability of extrapolation of Turbulent kinetic energy (TKE), Reynolds stresses, production and dissipation of TKE. Westerweel (Westerweel et al., 2013) claimed that PIV has largely superseded LDV and HWA even they beat PIV in some applications.

PIV has become the dominant approach in experimental fluid mechanics in the three decades since it was introduced. While most of the experiments were limited to lab studies, it is reasonable to question whether one can extrapolate real natural behavior from the laboratory (i.e., which measured in a flume). It is technically feasible although challenging to deploy the PIV in the natural aquatic field, and some configurations for field work need to be conducted. A team led by Dr. Katz from Johns Hopkins University devised a submersible oceanic PIV system for turbulence measurements in Bottom Boundary Layer (BBL) of coastal oceans (Bertuccioli et al., 1999a; Nimmo Smith et al., 2002; Smith, 2007). Katz team found that the natural seeding in the ocean is sufficient for obtaining high-quality PIV data like the laboratory applications which mostly seeded with microscopic tracer particles. The oceanic PIV was submersed into the ocean and mounted on a hydraulic scissor-jack to enable obtaining the turbulence characteristics like production and dissipation of Turbulent Kinematic Energy (TKE) and true spatial turbulence at various elevations above the seafloor.

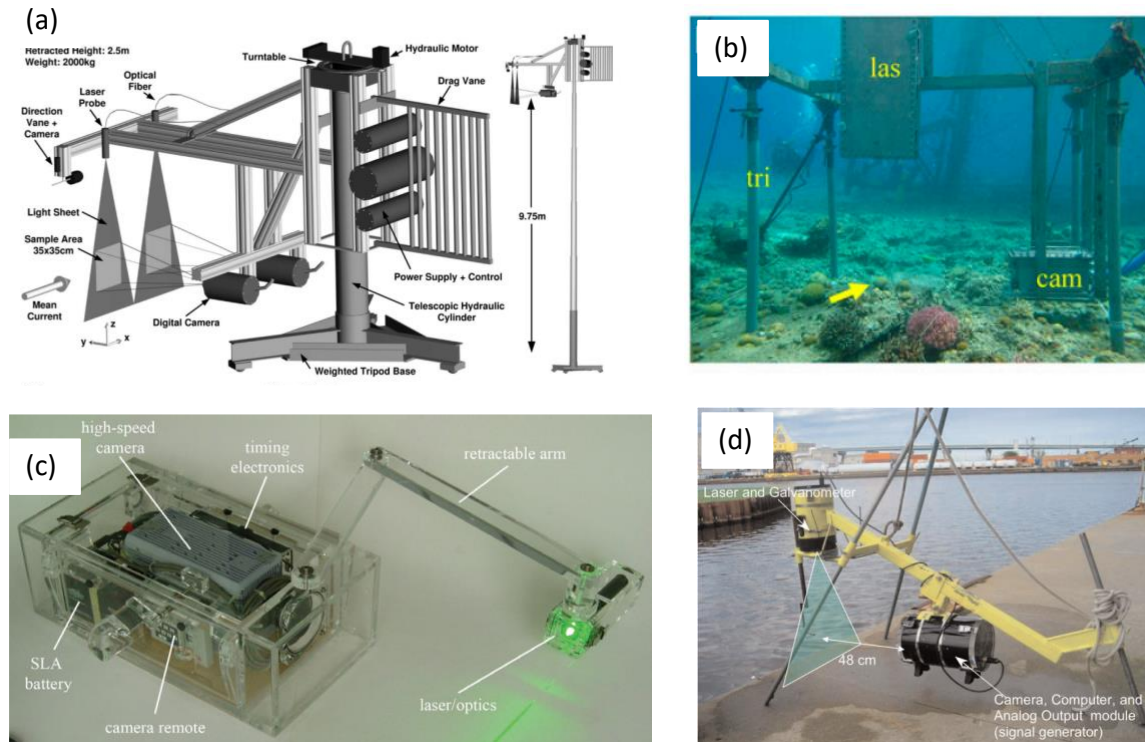


Figure 1.2 Literature review of the underwater PIV.

(a) is the Ocean PIV made by Katz team(Doron et al., 2001), (b) is the UPIV by Kremien(Kremien et al., 2013) (c) is the SCUVA system by Dabiri team, Stanford University(Katija and Dabiri, 2008) (d) is the previous version of the UWPIV in our lab(Liao et al., 2009).

Katija and Dabiri developed the Self-contained Underwater Velocimetry Apparatus (SCUVA) (see Figure 2.2(c)) for investigating the natural real behavior of animal's swimming motions in field. The portable design of the SCUVA system enables a single SCUBA (Katija and Dabiri, 2009, 2008) and robot diver (Katija et al., 2015) to make in-situ PIV measurements of animal-fluid interaction in the field. The measurement concluded that the animal swimming generated turbulence is comparable to the levels caused by winds and tides.

Liao and Wang developed a low-cost self-contained in situ underwater PIV system and applied it in the region near bottom and air-water interfaces (Liao et al., 2015, 2009; Wang et al., 2015; Wang and Liao, 2016a), and upgraded to a dual-beam dual-camera system for fast flow

measurement (Wang et al., 2012). However, Underwater PIV measurements in the field are limited by its spatial extension due to the large dimension of environmental flow. It is thus only useful for the investigation of very specific problems, focusing on turbulent transport near environmental interfaces, such as the water-air and water-sediment interfaces. Moreover, environmental flows are much more complicated than simulated laboratory conditions. Flows are usually transient, and external driving terms (such as surface gravity gradient, winds, and waves) affect the transport process over a wide range of temporal and spatial scales. Canonical theories of turbulence analysis, such as the Law-of-Wall (LOW) and an equilibrium boundary layer TKE budget, may not apply well in analyzing realistic environmental flows (Liao et al., 2009; Wang and Liao, 2016a). Questions remain on how to extract meaningful mixing and transport parameters from PIV-resolved velocity distribution in 2D or even 3D spaces. One major objective of this dissertation is to explore analytical methods to estimate turbulence statistics for parameterizing environmental transport models that evaluate flux across environmental interfaces where canonical boundary layer theories may not apply.

1.4 Structure of the thesis

Chapter 1 introduced the quagga mussel caused eco-system problems, and the researches related to this problem. From the literature review of the papers published, we hypothesize that profundal mussels can enhance near-bed turbulence due to siphonal currents, thereby maximizing food capture fate by keeping particles in suspension in a thin layer immediately above the mussel bed in the low energy flow condition. The main task of this thesis is to verify this hypothesis and to quantitatively measure the turbulent mixing rate above the mussels to further estimate the environmental impact of mussels. The PIV technology applied in the measurement is also introduced in this chapter.

In chapter 2, the experiment methods are introduced including the information of the experiment site, hardware of the instrument, the digital image processing methods for the postprocessing. The measurements carried out with our PIV measurement also introduced in this chapter.

Chapter 3 shows the turbulence feature extraction methods and results. The methods for Turbulence Kinetic Energy (TKE, TKE dissipation rate, and turbulent diffusivity estimation are discussed. The correlations between the turbulent features and the other parameters, e.g. mean velocity and particle concentration were also discussed in this chapter.

Chapter 4 is the hypotheses testing by modeling analysis. Both the analytical and numerical modeling analysis was applied in the One-D advection-diffusion model for phytoplankton concentration. The Soluble Reactive Phosphorus (SRP) flux been estimated from the turbulent diffusivity and the measured SRP profile.

Chapter 5 contains the conclusion and discussion. The result of the hypothesis testing and the impact of the mussel on the environment are discussed. And the limitations of the measurements and the modeling are also discussed in the discussion section.

CHAPTER 2. METHODS

2.1 Instrumentation: an Underwater-Particle Image Velocimetry (UW-PIV) system

Taking the advantages of PIV measurements, which can resolve instantaneous spatial structures as well as temporal evolutions of turbulent flows, the focus of this thesis study is to quantify turbulence structures in the benthic boundary layer of Lake Michigan. Due to the extreme low Reynolds number, mussels' bioturbation, and very low seeding density in the benthic lake, it is challenging to evaluate turbulent mixing parameters with traditional acoustic instruments (e.g., ADV). Classic theories, such as the Law-of-Wall (LOW), may not be applied in such hydrodynamic conditions. One main objective of my thesis work is to explore practical procedures to parameterize mixing processes using 2D PIV analysis, specifically, to extract the Reynolds stress, Turbulent Kinetic Energy (TKE), TKE dissipation rate, and turbulent viscosity/diffusivity from spatial-temporal filtering of velocity maps resolved from particle image pairs.

A detailed description of the working principle of a battery-powered UnderWater PIV (UW-PIV) system can be found in Liao et al. (2009). In the present study, the construction of the UW-PIV system is similar in concept with a free-floating PIV (FPIV) system developed by Wang et al. (Wang et al., 2013), for measuring near-surface turbulence measurement. In their study, the system was designed to be sealed in two waterproof housings, i.e., a camera-computer unit, and a laser-battery unit, which was connected through 8-pin bulkhead connectors for signal transfer and power supply. The current UW-PIV system was updated by using three underwater housings: a laser housing was arranged at the top to introduce the "laser sheet" to the lake bottom; an imaging system housing was arranged near the lake bottom to view the "laser sheet"

from an orthogonal angle; and a battery housing was mounted on the top of the frame for easy access, tuning, and recharging, and to avoid reconfiguration of the laser and camera between consecutive deployments. The three housing units are mounted on a rigid platform made of cast iron water pipes connected with galvanized pipe couplers and fittings (see Figure 2.1), which are easy to assemble and position housings in field deployments. The three units were connected through two underwater eight-pin cables and coupling water proof bulk-head connectors (SubConn Inc.) for electricity and signal transmission. Specifically, the computer-camera unit was connected to the battery unit for the power supply and laser unit for signal synchronization and power supply. Communication to the imaging unit from a host computer was made through a SubConn underwater Gigabit Ethernet bulkhead connector, thus the host computer can access the imaging system via the Secure Shell (SSH) protocol for configuration, tuning and data download. Batteries were wired to a timer switch in the battery housing for the convenience of charging and setting deployment duty cycles. The dimensions of the UW-PIV system are shown in Figure 2.2.

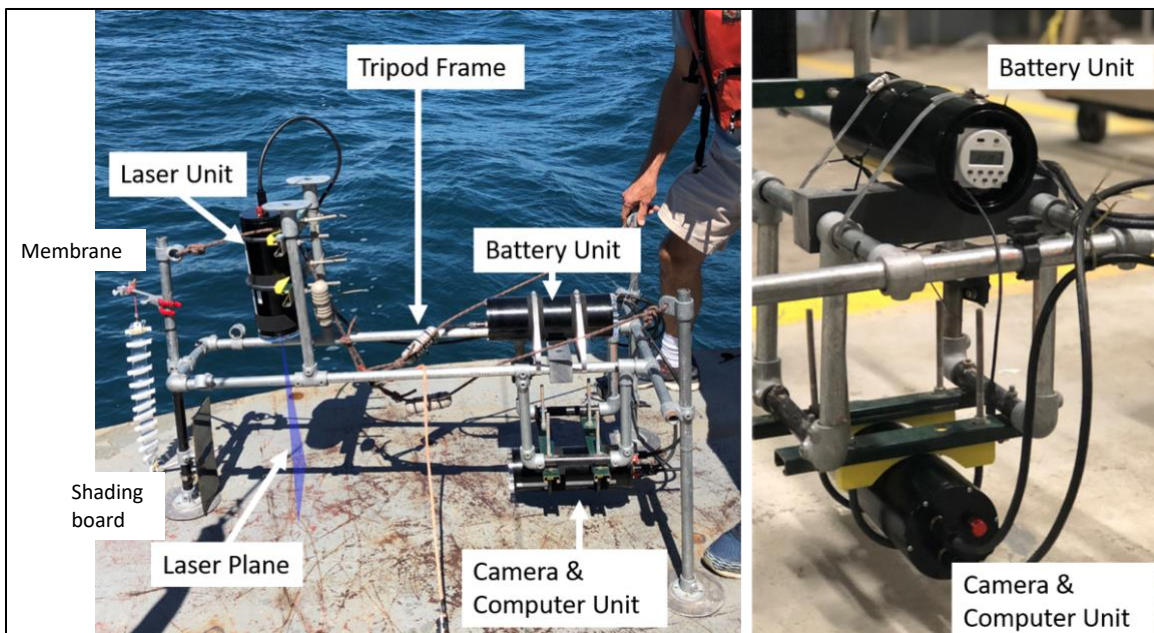


Figure 2.1 Structural configuration of the Underwater PIV system.

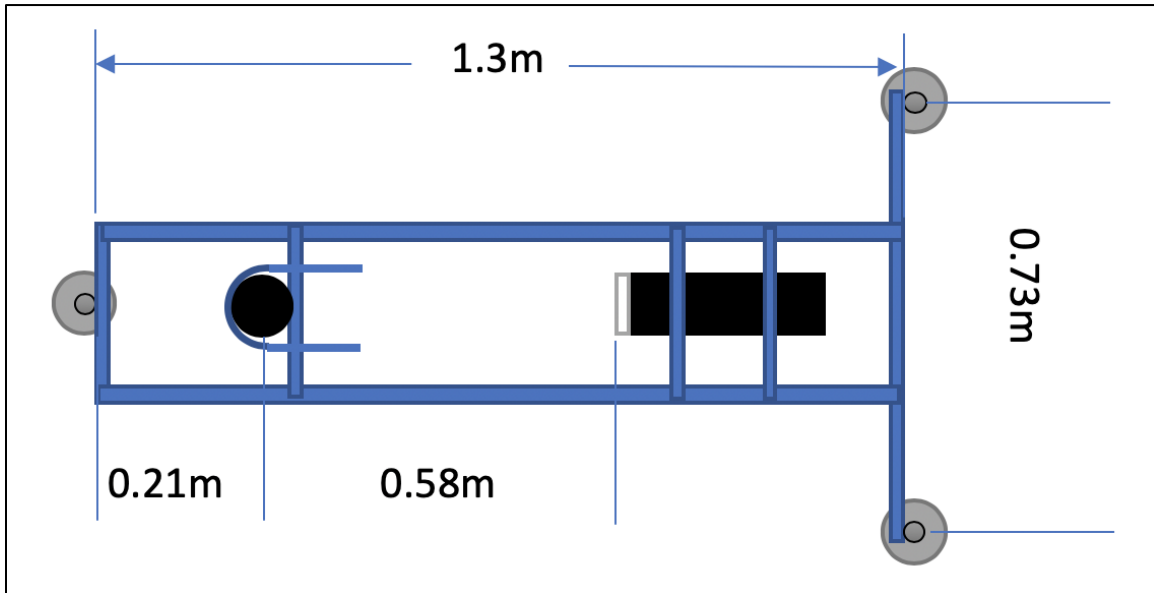


Figure 2.2 The dimensions of the UW-PIV frame.

The overall size of the UW-PIV frame is 0.73m*1.3m*0.77m; the distance between the FOV and front of the camera-computer unit is 0.58m; the distance from the background board to the FOV is about 0.21m.

Since the invasion and expansion of zebra and quagga mussels in Great Lakes over the past thirty years, their filtration activities have reduced the biomass (primarily phytoplankton) in the water column significantly. This has resulted in an increase in water clarity. Preliminary tests showed that light intensity from solar radiation during summer daytime is strong even at the 55-m deployment site for this study. Since the camera in the UW-PIV system is not a specialized PIV camera, the inter-frame transfer time is limited by the maximum frame rate, i.e., it is not possible to maintain a short exposure duration and a short interval time simultaneously between two consecutive exposures. A “throttle” approach was applied to adjust the PIV inter-exposure time (Δt) with the timing of laser-firing (Liao et al., 2009). Consequently, the camera exposure time has to be set as the reciprocal of the maximum frame rate, e.g., 33 ms of minimum exposure for a 30Hz of maximum framerate. Such a long exposure time results in over-exposed images

during daytime deployment even at the 55-m depth and with a narrow-band optical filter (50 nm width centered at the laser’s optical wavelength) applied to the camera. To partially overcome the over-exposure problem, a “shading” board (i.e., a background blackboard) was attached on the front leg of the platform (see Figure 2.1) to prevent scattered sunlight from entering the camera lens orthogonally during daytime measurements. The size of the “shading board” is about 20 cm high and 10 cm wide. The effectiveness of the shading board can be demonstrated in Figure 2.3. It should be noted that the shading board could not completely solve the over-exposure problem, particularly on sunny days around noon.

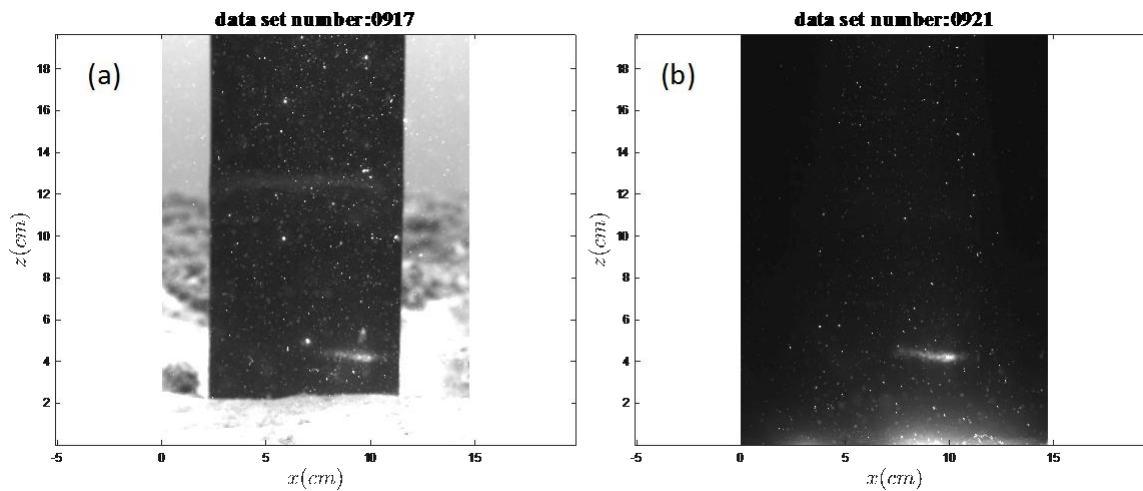


Figure 2.3 Particle images captured during daytime and night. The comparison shows that the background board shows excellent performance of blocking the sunlight.

2.2 Components of the UW-PIV system

A major upgrade of the UW-PIV system had been made to minimize its perturbation to the flow field. The sizes of both the Camera-computer unit and Laser unit were reduced significantly compared to the previous version (Liao et al., 2009). The size reduction was

achieved through adopting a new set of electronic components centered on an Arm-Linux based single-board computer Odroid-XU4 with USB 3.0 and Gigabit Ethernet I/O interfaces. The Odroid-XU4 boasts sufficient data transfer speeds for camera streaming demand. The data acquisition card which synchronizes camera triggering and laser triggering were developed from an open-source microcontroller Arduino Due. The synchronizing method was referred to mode (g) PIV imaging configuration (Raffel et al., 1998). Due to the recent development of diode lasers, more power-efficient lasers in the 440~450 nm wavelength are available. A 15W 445 nm (nominal) continuous-wave (CW) laser was selected, replacing the 2W CW laser in the previous version of UW-PIV system. Since the turbulence/current level in benthic Lake Michigan is typically low, it is affordable to choose a relative long inter-exposure time ($\Delta t = 5\sim 20$ ms) for PIV imaging. Meanwhile, the enhanced laser power allows longer exposure time for each “pulse” without causing serious “motion blurring” effects. Therefore, laser “sheet” was generated through the classic and straightforward cylindrical lens setting, eliminating the need for the scanning mirror component in the previous UW-PIV system (Liao et al., 2007). With Ubuntu Linux running on the PIV computer, the computer could be remotely accessed as a server via SSH. Through the Ethernet socket in the computer and camera unit, the user can download recorded images by bash scripts running on a host laptop. A CMOS machine-vision camera with USB3 interface (Point Gray Research GS2-U3-32S4M-C) was selected for PIV imaging, primarily due to its support with Arm-Linux based host computer. Image acquisition software was developed with the camera’s SDK in C language and compiled into a dynamic library on the Arm-Linux platform. A python program was written to call the image acquisition library and to communicate with the signal generation system (the Arduino Due module) for system synchronization.

Major imaging components and their layout in the waterproof housing is shown in Figure 2.4. The signal flows among major components is illustrated in Figure 2.5. The specifications of major hardware components adopted for the UW-PIV system are listed in Table 2.1.

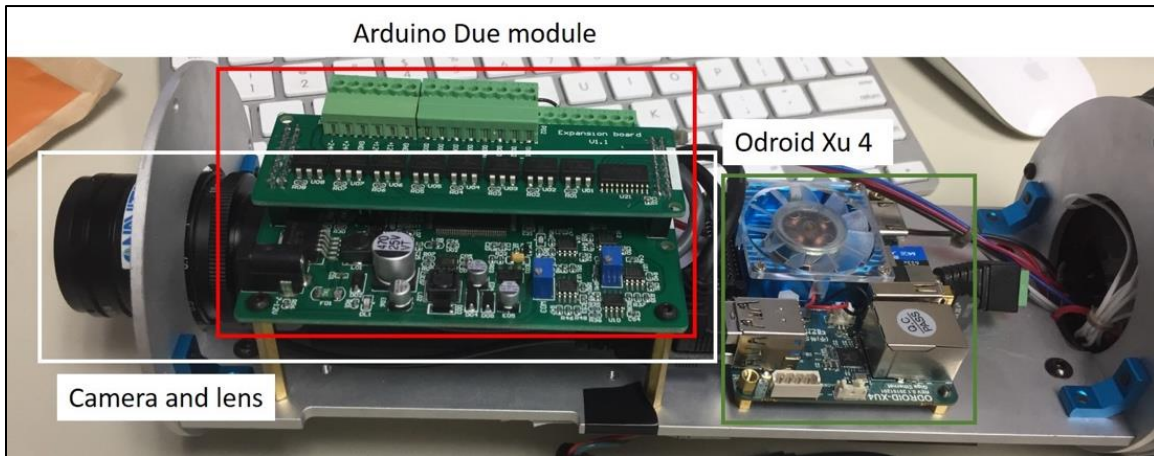


Figure 2.4 Inside the Camera-Computer unit.
The circuit board and camera were arranged compactly by Solidworks for fitting the 4-inch housing provided by Blue Robotics.

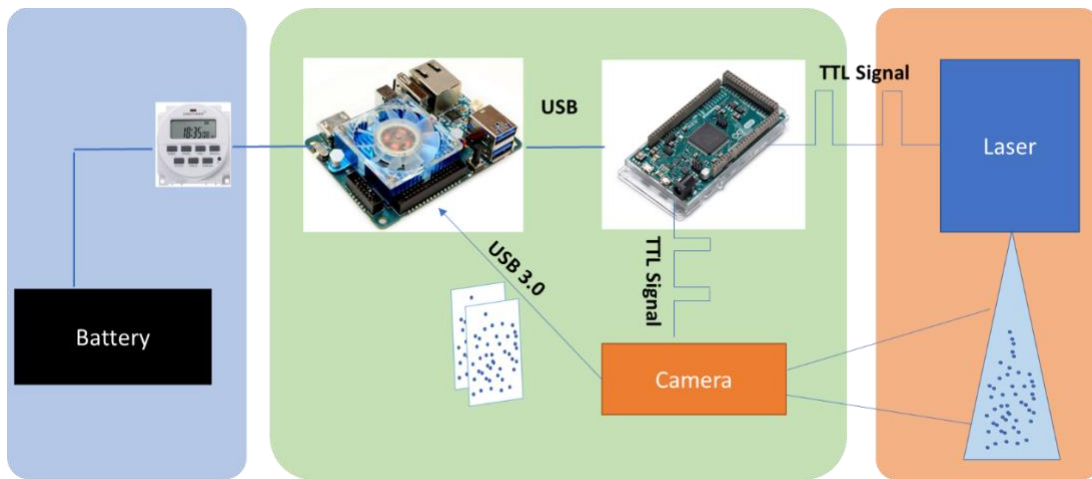


Figure 2.5 UW-PIV synchronization signal flow chart

Table 2.1 UWPIV hardware list

Equipment list	
Computer	Odroid XU4, Ubuntu 18.04, USB 3, 1000Gb/s Ethernet (GigE supported)
Synchronizer	Arduino Due, Clock speed: 84 MHz
Laser	Power: 15Watts, Wavelength: 445nm, Pulsed mode control: TTL+
Camera	Point Grey GS2-U3-32S4M-C, Frame rate: 121 FPS, Color: Mono, Resolution: 2048×1536, With a C-mount 16mm lens, the $FOV = 29^\circ \times 19^\circ$
Battery	Li-po 15AH,12V
Housing	Blue Robotics aluminum enclosures (4" series and 3" series)
Cables	SubConn 8 pin underwater cables, SubConn Ethernet cables

2.3 Deployment locations and timings

Multiple versions of in-situ Underwater Particle Image Velocimetry systems have been routinely deployed in coastal waters of Lake Michigan near the city of Milwaukee during the past decade. For this thesis study, field experiments were conducted in Lake Michigan from the summer of the year 2018 to the fall of the year 2019, with nearly a full year of data characterizing the near-bed turbulence primarily at a deep site of Lake Michigan. The site is located at (42°58.809'N 87°39.800'W) to the east of Milwaukee, Wisconsin with a 55-m depth (see Figure 2.7a). The bed material is a mix of sand (from fine to coarse) and silt. The lakebed at the sampling site was mostly covered by quagga mussels, with relatively small size (i.e., averaged mussel size is about 0.9 cm with only 1~2 largest ones of 2.8 ~2.9 cm per Ponar grab

(area is about 22.5X22.5cm²)) compared to those found in coastal regions. Figure 2.6 shows the underwater image of the mussel-covered lakebed at the measurement site (Troy et al., 2016).

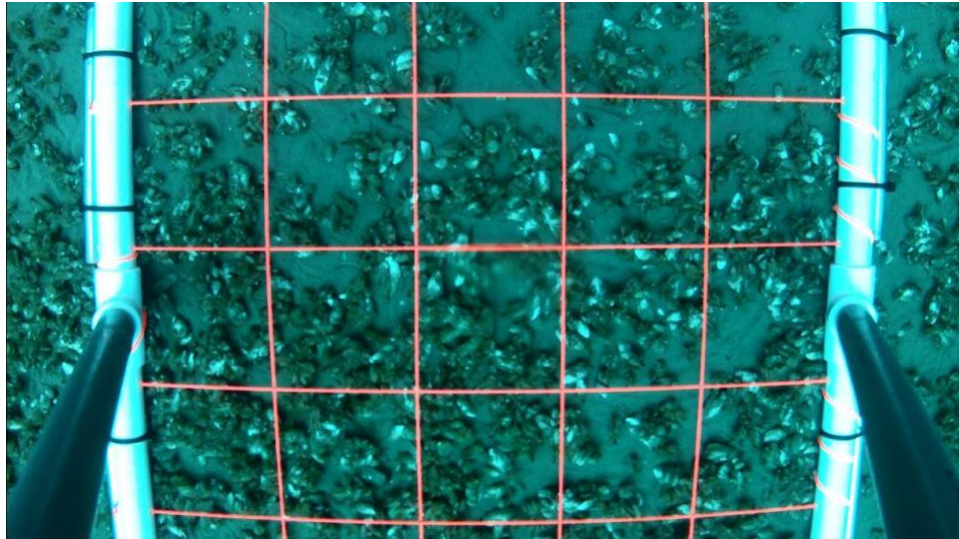


Figure 2.6 Profundal mussel density in 55m site of Lake Michigan, Photo from Bootsma Team, UWM

In addition to the 55-m site, a few deployments were made at two shallower sites with 10-m and 25-m depths, respectively. The 10-m site has been extensively sampled with an autonomous observational platform for meteorological conditions, water temperature profiles and other biochemical parameters over the past decades. Since it is about 1 mile off the coast near the Atwater Park in Milwaukee, WI, it was named as AW10. Accordingly, the other two sites are denoted as AW25 and AW55, respectively. The AW10 site has a rocky substrate that provides support to mussel establishment. Locations of all three sites are presented in Figure 2.7 and Table 2.2. The AW25 site was selected with the objective to examine mixing near the summer thermocline (20~25 m when stratified). In this thesis, only data from AW55 were analyzed since the main objective was to examine the effects of bio-mixing in the profundal water of Lake Michigan.

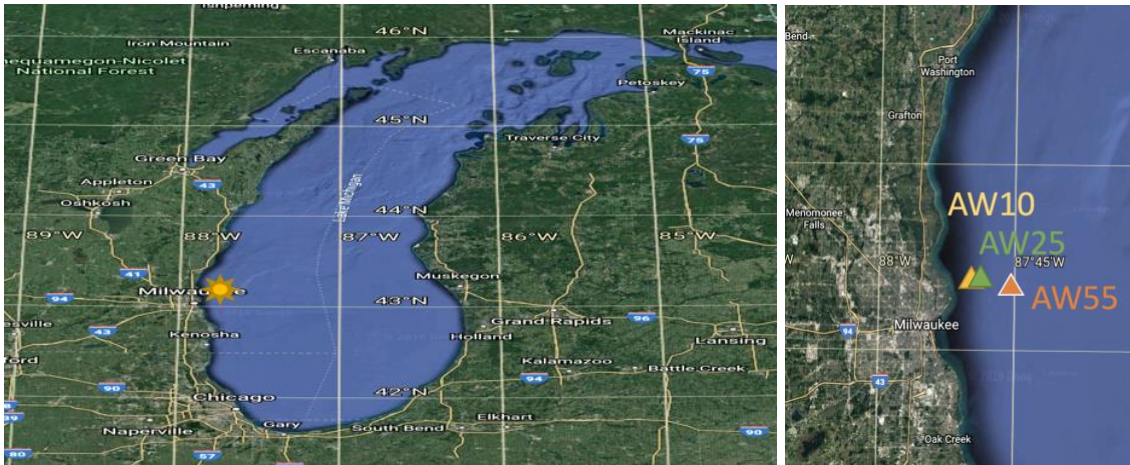


Figure 2.7 UW-PIV deployment locations.
The three sites were named as AW55, AW25, and AW10 for the location of the sites near the Atwater Park, Milwaukee, WI. Map: Google Earth

Table 2.2 Deployment sites information

Name	Coordinate	Depth
AW55	(43°04.35' N, 87°51.87' W)	55m
AW25	(43°06.62' N, 87°50.68' W)	25m
AW10	(43°05.71' N, 87°51.87' W)	10m

The density and size distribution of mussels at AW55 were estimated from replicate bottom Ponar Grab (sample area was 22.5X22.5cm²). The total mussel density was approximately 8300 mussels/m² (greater than 0.2cm) and 5200 mussels/m² (greater than 0.5 cm) (Mosley and Bootsma, 2015).

The UW-PIV system was deployed from *R/V Neeskay, UWM*, by lowering it down to the lake bottom from a winch (Figure 2.8 a). The system was then left on the bottom for 5~10 days with a string cable connecting to a surface marker buoy to indicate its "landing" location for retrieval (Figure 2.8 b). During the deployment, a waterproof action camera GoPro was mounted on the platform and recorded a video for several hours after the deployment to check the surrounding environment of the deployment site. It has been observed that the 55-m site was

covered with high-density patches of mussels during the last few years, almost every UW-PIV deployment has landed on a substrate covered with quagga mussels.

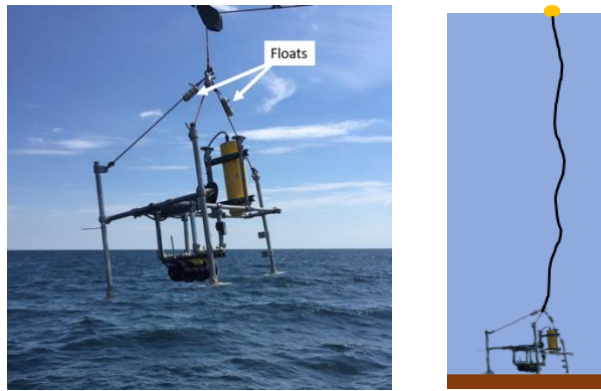


**Figure 2.8 Deploying UW-PIV on Lake Michigan.
The UW-PIV frame was deployed on the deck of *R/V Neeskay*, UWM**

The Linux-based computer in the camera housing was accessed remotely through the underwater Ethernet cable with SSH before and after the deployment for setting parameters and downloading recorded images. The sampling frequency was set to be 1 Hz (e.g., 1 image pair per second) for PIV imaging acquisition. The total sampling time per data set was approximately 10-13 minutes, which allows acquisition of about 400-600 pairs of images, including the system boot time.

Table 2.3 summarizes location, time, duration and PIV acquisition configurations for each deployment from July 2018 to September 2019. The winter season between November 2018 and April 2019 was skipped for safety concerns.

Figure 2.9 shows the histograms of horizontal velocity components measured at 25 cm height above the lake in August 2017 at the AW55 site (Data courtesy from David Cannon). The histogram shows that the typical velocity magnitude near the bottom is from 0cm/s to 5cm/s. This velocity range was used to set approximate PIV inter-exposure time to be $\Delta t = 20$ ms by considering the image resolution and ten imaging pixels as the optimal particle image

displacement for the cross-correlation analysis. As shown in Table 2.3, Δt was set to 20 ms for most cases, except for a few cases where it was 10 ms, particularly at the more dynamic shallower AW10 and AW25 sites.

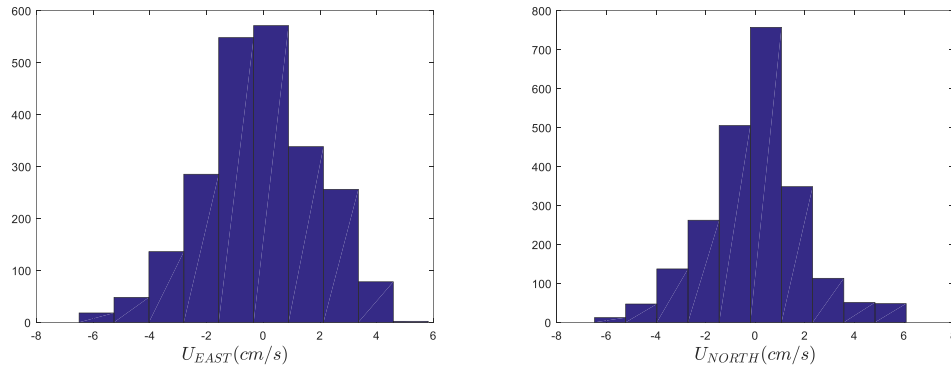


Figure 2.9 Histogram of the velocity measured by an ADV at the height of 25cm above the lake bottom. Data were acquired in August 2017 at the AW55 site. The full width at half maximum of the fitted Gaussian distribution is around 4.6cm/s.

Table 2.3 UW-PIV deployment date

Record date	Sample site	Data sets	PIV Δt (ms)	Laser pulse width(ms)	Data set number
7/17-7/18/2018	AW25	12	5	2	0004-0016
7/24-7/31/2018	AW55	64	10	5	0018-0081
7/31-8/9/2018	AW25	71	10	5	0084-0155
8/9-8/16/2018	AW55	55	10	5	0157-0212
8/16-8/22/2018	AW55	111	10	5	0214-0325
8/23-9/4/2018	AW55	139	20	5	0327-0466
10/9-10/16/2018	AW55	48	20	5	0485-0533
5/2-5/14/2019	AW55	180	20	5	0554-0735
7/1-7/11/2019	AW55	166	20	5	0741-0907
8/27-9/20/2019	AW25	231	20	5	0916-1146
9/23-10/14/2019	AW10	N/A	10	5	N/A

Figure 2.10 shows some sample images acquired at the three deployment sites. The deployment case AW25-01 was on a mussel bed which was covered with algae; nearly half of the images were blocked by the algae grow on the mussel bed. The deployment of AW25-02 was on a flat sandy lakebed without mussels. All of the deployments at AW55 were landed on a mussel-covered substrate, and mussel siphons can be clearly seen in these sample images. Another observation is that the particle density at site AW25 was significantly higher than that at the AW55 site. The low particle density brings technical challenges for PIV analysis, and it was also found that acoustic-based velocity measurements were unsuccessful in the near-bed region at the AW55 site due to extremely low signal to noise ratio. The resolution of the acquired images is 2048*1536, the laser sheet width in the image is about 10 cm, then the effectively FOV is around 20 cm in height and 10 cm in width.

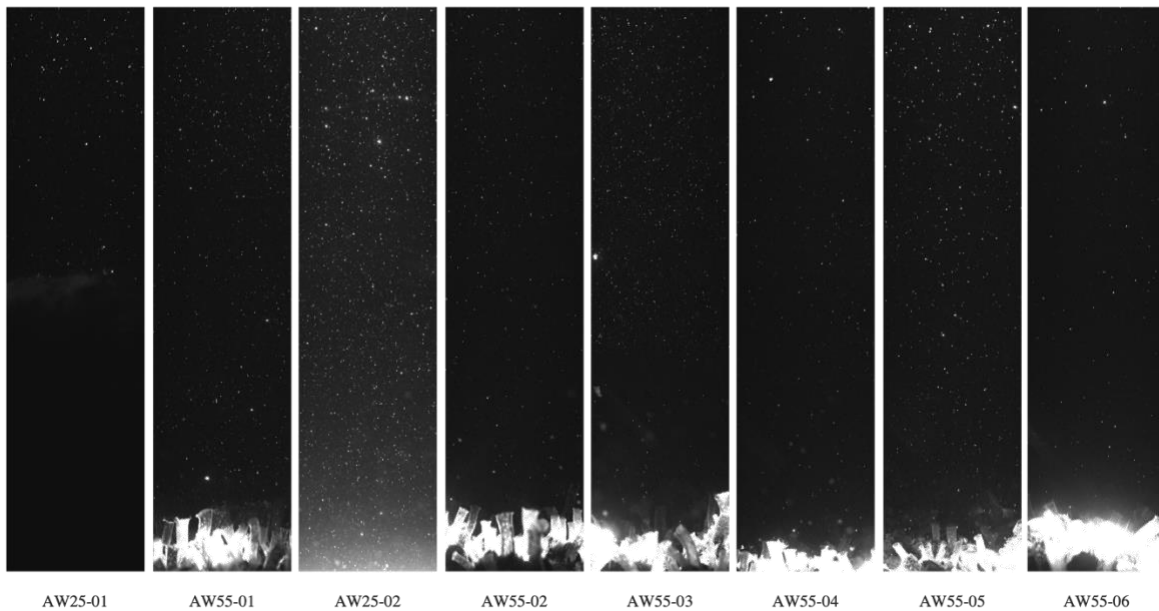


Figure 2.10 Sample images of deployments.

2.4 Companion measurements, Micro-profile coupled with PIV

The membrane method for measuring the chemical profiles near the lake bottom was introduced by our companion Rae-Ann MacLellan-Hurd from Harvey Bootsma Lab, UWM. This sampling technique relies on molecular diffusion through the membrane until the water inside the membrane is in equilibrium with the ambient water.

The sampler that was attached with our UWPIV frame and was deployed with the UWPIV deployments; Figure 2.11 shows the photos of the sampler and the UWPIV frame, two samplers were attached in case one of the samplers failed. The UWPIV was deployed not less than six days, which is long enough for the sampler to reach chemical equilibrium with ambient water, based on laboratory equilibration experiments carried out in Harvey Bootsma Lab, UWM. Upon retrieval, the membranes were sampled using syringes for each, and analyzed in the lab for the Soluble Reactive Phosphorus (SRP) profile.



Figure 2.11 The membrane tube attached in the UWMPIV frame

2.5 PIV interrogation and post-processing

To minimize the impact of ambient light, particularly for those images acquired at daytime, PIV images were pre-processed to remove the “background” before interrogation analysis. A local median filter was applied based on a 60×60 pixel window to the raw image, and the result is considered as the “background” image, which was then subtracted from the original image.

The 2-D velocity field was calculated through a central difference based (2nd order accurate in space), anti-aliasing PIV interrogation algorithm (Liao and Cowen, 2005). PIV interrogation analysis includes a single-pass analysis with a subwindow size of 40×40 pixels (3.84×3.84 mm physically). PIV mesh was constructed with a 50% subwindow overlap, therefore the spatial resolution of the measured 2-D velocity field was 20×20 pixels, or 1.92×1.92 mm.

PIV measurement errors in this study were primarily due to low particle seedings (because of mussels' filtration) and occasional strong out-of-plane motions. To minimize the impact of measurement errors, raw PIV data were post-processed to remove "outliers" of velocity measurements based on the so-called "median test" approach, which is the most widely used method to identify "spurious" vectors in post-interrogation validation of PIV data (Westerweel, 1994). Specifically, an improved adaptive "median test" (Westerweel and Scarano, 2005) was adopted here, and the procedures is summarized as the following. First, consider a measured velocity at a given PIV mesh grid, v_0 , which can be either component of the 2D velocity vector. Its neighboring data are selected from the local 5×5 mesh grids (excluding v_0), and they form a data series $v_i \equiv \{v_1, v_2, \dots, v_{24}\}$. The median value of the data series is then calculated and denoted as v_m . The residual of the local data, defined as $r_i = |v_i - v_m|$, and their median r_m can be evaluated. Therefore, a local-adaptive and normalized residual of the measurement v_0 is defined as: $r'_0 \equiv \frac{|v_0 - v_m|}{r_m}$. The measured velocity is deemed as valid if r'_0 is less than a threshold value, which is set to 2.0 in this study as suggested in (Westerweel and Scarano, 2005). Otherwise, it is considered as a spurious vector. Subsequently, spurious vectors were removed and replaced by the local median v_m .

Results of PIV pre-processing, interrogation and post-processing procedures are demonstrated through an example illustrated in Figure 2.12. The velocity quiver plot shows two velocity components that are subtracted by their mean values averaged over the entire FOV. The coordinate was defined as shown in this figure, where $z = 0$ was selected to be just above the mussel bed. Active mussel siphons were clearly seen in the PIV images. Ideally, a small spatial resolution should be chosen to provide more accurate small-scale turbulent structure analysis (e.g., turbulent dissipation rate can be estimated base on the gradients of instantaneous vector

distribution). However, due to the strong depletion effect of high-density mussels in deep, low energetic waters, the particle density is relatively low for PIV interrogation if smaller sub-windows were used. It was estimated that the Kolmogorov length scale in this study was in the range of $\eta = 0.7\sim 1.1$ mm. According to the relationship between total fraction of dissipation rate and resolved wavenumber, the underestimated dissipation rate is smaller than 5% if the grid resolution is less than 5η (3.5 ~ 5.5 mm) (Cowen et al., 1997). This suggests that PIV resolution in this study (1.92 mm) is sufficiently high for using direction spatial differentiation as a good approximation for local velocity gradient, thus the “Direct Method” can be applied to estimation the dissipation rate of TKE.

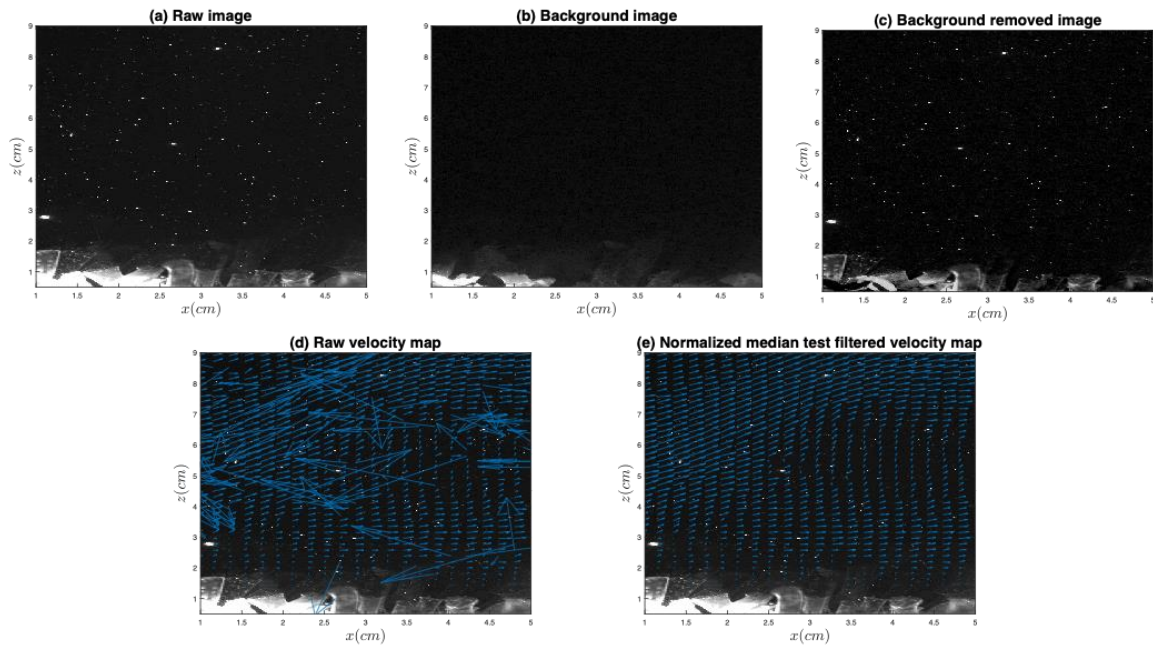


Figure 2.12 An example of PIV pre-process, interrogation result and post-process (adaptive median test) result.

2.6 Analysis of particle concentration data

Particle images provide another interesting and important information to characterize the bio-mixing processes by quagga mussels. Specifically, the instantaneous distribution of particle density can be estimated if individual particles can be identified and registered. It was assumed in this study that numbers of particles identified in a defined window are proportional to particle volume concentration, i.e., all particles are same in size. Thus, the turbulent flux of particles $-\overline{u'_i c'}$ can be estimated, where u'_i and c' are velocity and particle concentration fluctuations. Subsequently, the “eddy” diffusivity of particles can be estimated following the Fickian transport theorem, i.e., turbulent flux is proportional to the mean gradient, and the proportionality is the turbulent (“eddy”) diffusivity.

In this thesis study, particle density distribution was obtained through digital image processing that identified individual particles on images. The detail of the particle counting algorithm is similar to that presented by (Liao et al., 2009). The procedures is summarized as the following:

- 1) A raw PIV image is pre-processed to remove the background, similar to the PIV pre-process.
- 2) The background-removed image is smoothed through a Gaussian image filtering to reduce image “noise”.
- 3) A binary image is generated from the smoothed image by finding the regional maximum.
- 4) Particles and their locations are identified by analyzing pixel connectivity of the binary image.
- 5) The number of particles is counted in interrogation windows, which is then considered as the surrogate of particle density distribution.

Figure 2.13 demonstrates the particle identification procedure through a sample image from the data set AW55-0023. The result from this algorithm seemed to be as good as that can be identified by bare eyes. However, it was also found that some particles with very low image intensity and some particles adjacent to one big bright particle were not able to be identified by this algorithm.

Figure 2.14 shows the particle density evaluated from counting the positioned particle location from the same example case. The counting window was chosen to be the same as that for the PIV interrogation. The particle density, about 4 particles per interrogation window (IW) on average, is lower than that typically required for robust PIV measurements (usually greater than 5-10 paired particles per IW (Bertuccioli et al., 1999b)).

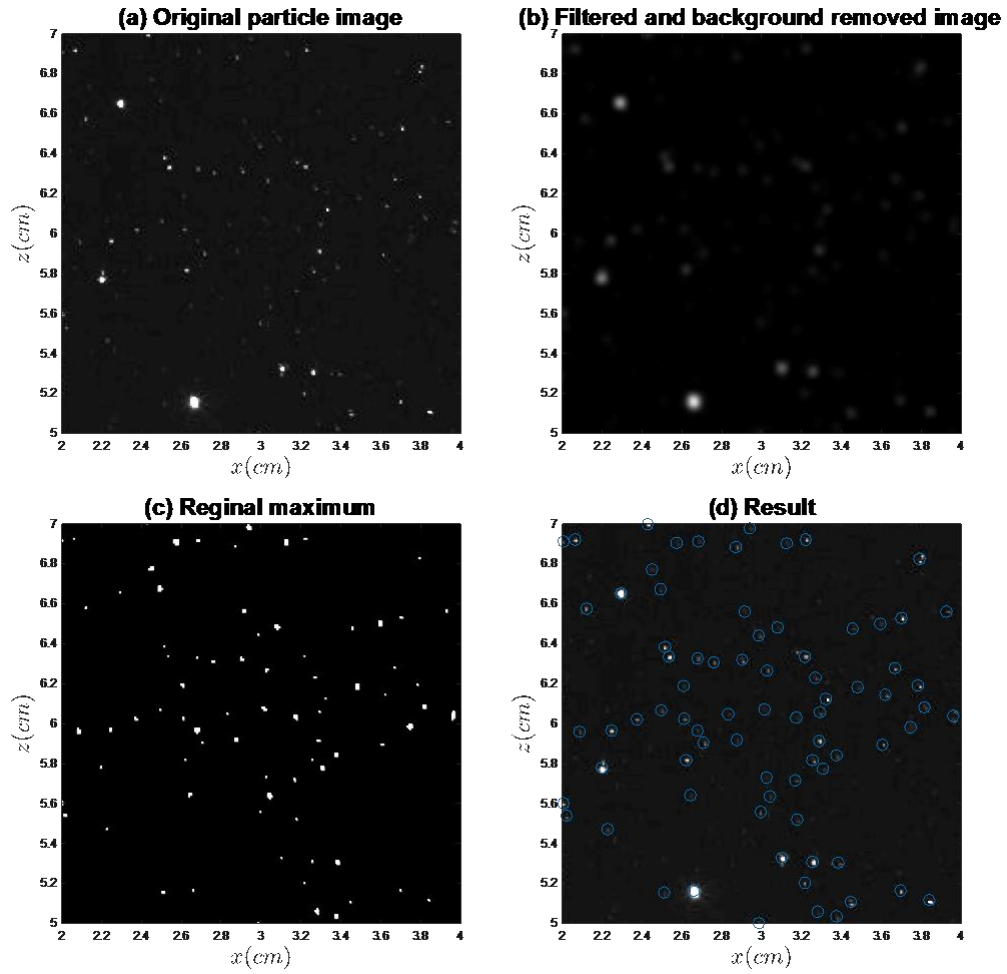


Figure 2.13 An example that illustrates the particle identification algorithm. (a) Raw PIV image, (b) image after background removing and smoothing, (c) binary image generated by regional maximum finding, (d) particles identified are marked with circles.

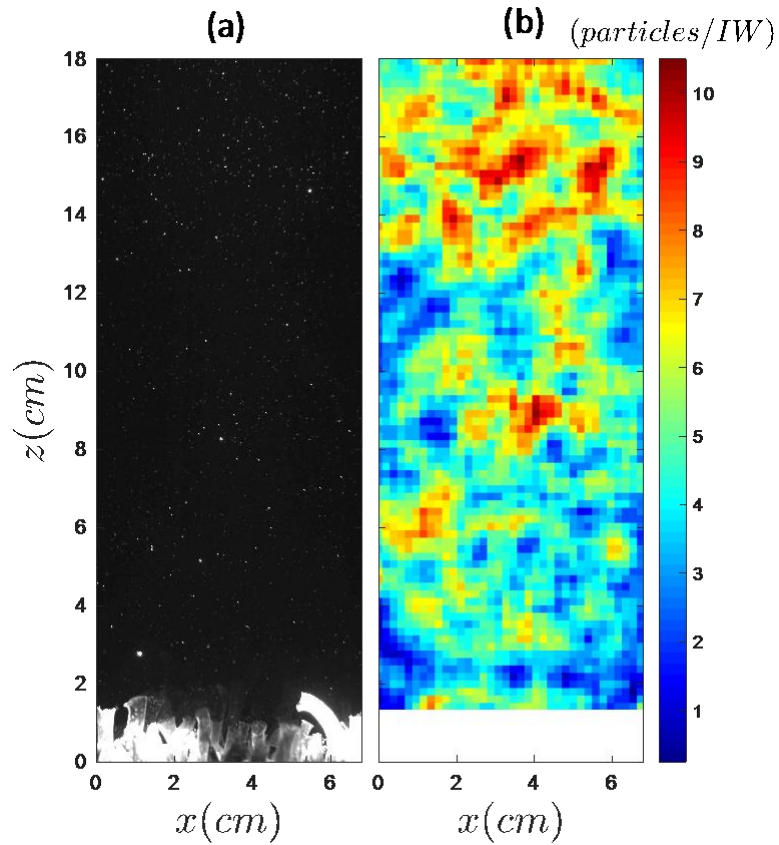


Figure 2.14 The particle counting results
(a) original particle image, (b) instantaneous particle concentration field resolved from the
same IW of PIV analysis (from data set AW55-01-0023).

CHAPTER 3. MEASUREMENT RESULTS AND DATA ANALYSIS

Turbulent diffusion is the transport of mass, heat, and momentum due to turbulence.

When turbulent mixing is intense, the molecular diffusion is negligible compared to the turbulent diffusion. The turbulent diffusivity or eddy viscosity is the parameter for quantifying the speed of turbulent diffusion. In this chapter, data cleaning methods are introduced for removing the wrong datasets and “Outliers” in the velocity maps. And the methods for extracting turbulent parameters from velocity map and particle concentration are conducted and evaluated for the turbulent diffusivity estimations.

3.1 The uncertainties of the mean flow direction and instrument perturbation

In the benthic environment of a deep offshore site of the Lake, the main currents appear to be random without noticeable prevailing directions, particularly when the velocity magnitude is lower than 5 cm/s (see Figure 3.1, the red dots) at the AW55 site. However, current flow speed exceeding 5cm/s (the yellow dots) seems to prevail along the northwest-southeast direction, which is approximately parallel to the shoreline near the site. Since the “landing” of the UW-PIV at the depth of 55m is often with random direction, it is certain that the PIV laser plane will be more likely not parallel to the main flow direction. With only one camera in the UW-PIV system, the third velocity component which is perpendicular to the image plane could not be resolved, thus we applied the “shading board” to artificially guide flows from random directions to be more or less aligned with the laser lane. However, it is unnecessary to have the measurement parallel to the main current in characterizing turbulent mixing processes while the turbulent flow could be assumed as isotropic. The assumption of isotropy is certainly not true for classic wall turbulence due to unidirectional external flow, i.e., near-wall streamwise velocity

fluctuation has a greater intensity than spanwise and vertical fluctuations. However, in the presented study, turbulence from mussels' "bio-mixing" processes can be assumed to be isotropic while the primary source of turbulence was from mussels' filtration activities.

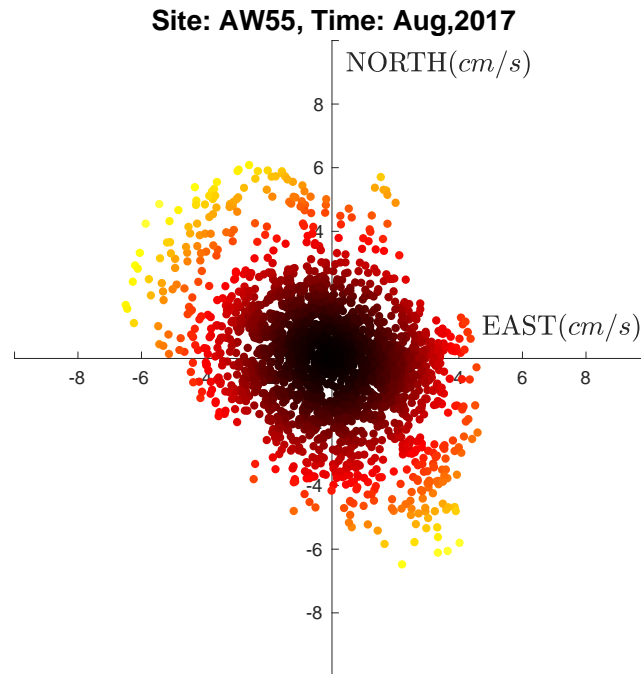


Figure 3.1 Near bottom velocity distribution measured by ADV (Acoustic Doppler Velocimeter) on the site of AW55 in August 2017.

The ADV sample volume was located 25cm above the lake bottom which is close to the PIV measurement ROI (from 0cm to 20cm above the bottom), every data points represents a ten minutes average. (Data courtesy from David Cannon, Purdue University)

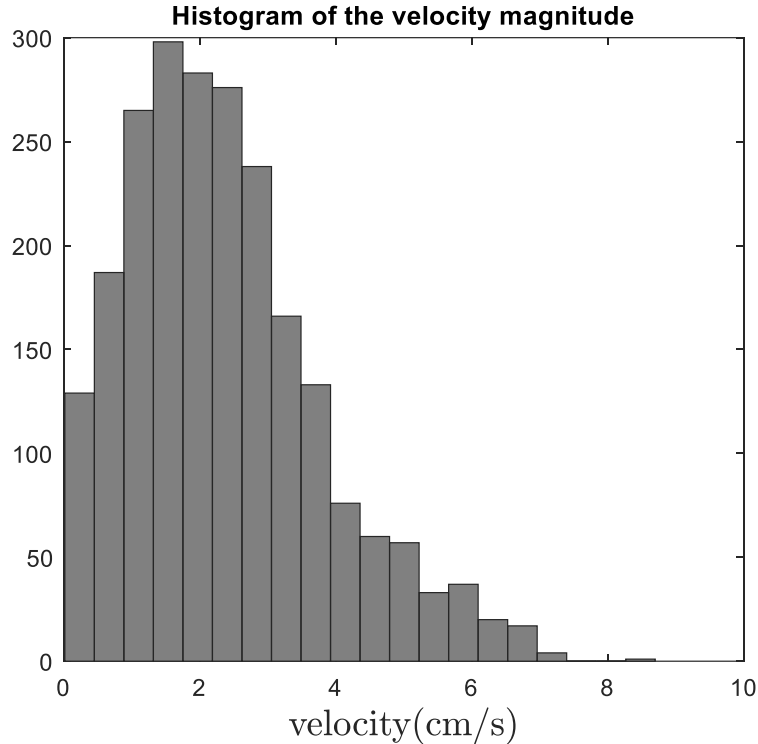


Figure 3.2 Histogram of the velocity magnitude from ADCP measurement, Aug 2017. Data provided by David Cannon, Purdue University.

However, concerns remain with cases where the ambient flow approaches to the laser sheet with large oblique angles. The UW-PIV system itself can block the flow from the front by the shading board or the back by the camera housing (see Figure 2.1), which may introduce significant perturbations (e.g., artificial wake turbulence) that can be advected to the measurement region. Thus, it is necessary to identify these cases and develop a criterion to discard them from subsequent analysis.

Time series of horizontal velocity at height $z = 5$ cm was extracted from PIV results for analysis. Most time series present a combination of slow transient trend, some low-order undulations and random (turbulent) motions (Figure 3.3a). A linear regression of the entire series was applied to represent the transient trend (dashed line). A lowpass filter (with an averaging time window of 50 s) was applied to preliminarily remove random motions, and the smoothed result is shown as a dotted line.

A few cases stood out with apparently organized oscillations with a fairly constant period of about 10 seconds (Figure 3.3a). Spectrum analysis of the horizontal velocity component shows a sharp peak located at the frequency of around 0.1 Hz (Figure 3.4a). It was hypothesized that the 0.1 Hz oscillation could be an indication of the instrument wake due to mean flows approaching the camera housing or shading board from large oblique angles. Other possible contributions were excluded from the analysis, such as the basin-scale lake seiche or internal waves (cycling period in the order of hours or days) and surface waves (due to the significant water depth).

Consider a main current flow against the measurement plane, the front shading board or the camera unit can obstruct the flow and generate a von Karman vortex street which is an unsteady oscillating flow. The frequency of the von Karmen vortex street can be estimated from similarity analysis. The width D of the shading board or the camera unit are around 0.1~0.2 m depended on the different flow directions, and the typical approaching velocity V is in the range of 1 cm/s to 5 cm/s, the kinetic viscosity ν in the temperature(about 4 °C) is $1.5 \times 10^{-6} \text{ m}^2\text{s}^{-1}$. So the Reynolds number, $Re = VD/\nu$, is in the range of 600~3000, by simplifying the obstacle as a cylinder. In this Reynolds number range the Strouhal number St is nearly a constant around 0.2 from the classic similarity analysis (Achenbach and Heinecke, 1981). The definition of the St number is:

$$S_t = nD/V \quad (3.1)$$

Where n is the oscillation frequency, which can be calculated as $n = S_t V/D$. This analysis indicates that $n = 0.005 \sim 0.1\text{Hz}$, which seems to agree with the peak frequency observed in some data series (see Figure 3.3(a), Figure 3.4 (a)), particularly when the current flow is on the higher end ($\sim 5 \text{ cm/s}$).

Following this analysis, a data rejection procedure was established according to the velocity spectrum of the measured time series. Datasets showing a significant “peak” around 0.1 Hz were then considered susceptible to instrument wake perturbation and removed from analysis. About 15% cases were rejected in this study. Figure 3.3(b) and Figure 3.4(b) show the time-series velocity and the spectrum of the case without a significant abnormal peak.

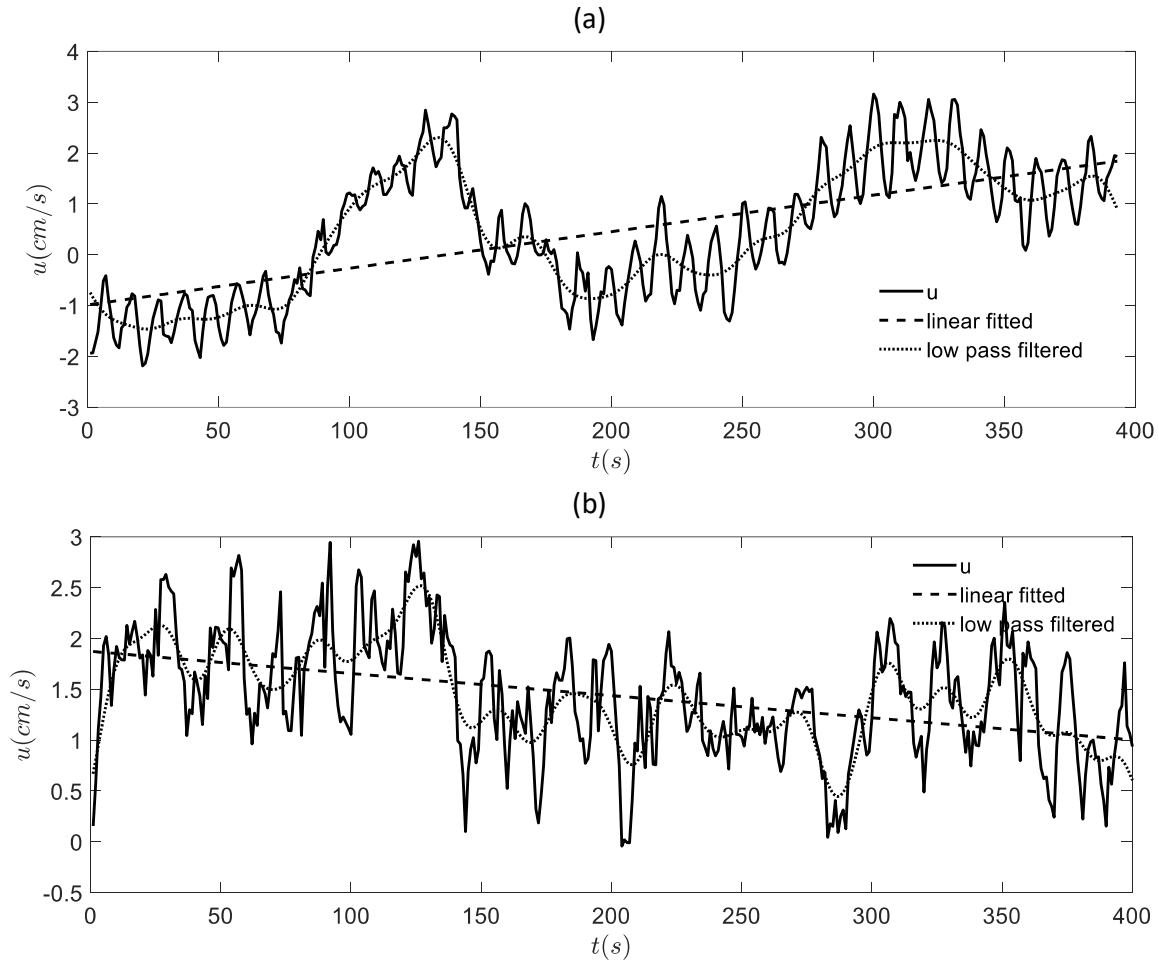


Figure 3.3 Time series of the streamwise velocity at $z = 5$ cm.
(a) A typical Time series of the streamwise velocity at $z = 5$ cm from data set. The dotted line represents the lowpass filtered ($= 50$ s) velocity signal. The solid line is the horizontal velocity, where the dashed line and the dotted line are lowpass filtered and linear regressed velocities. (b) is a case with normal time series streamwise velocity

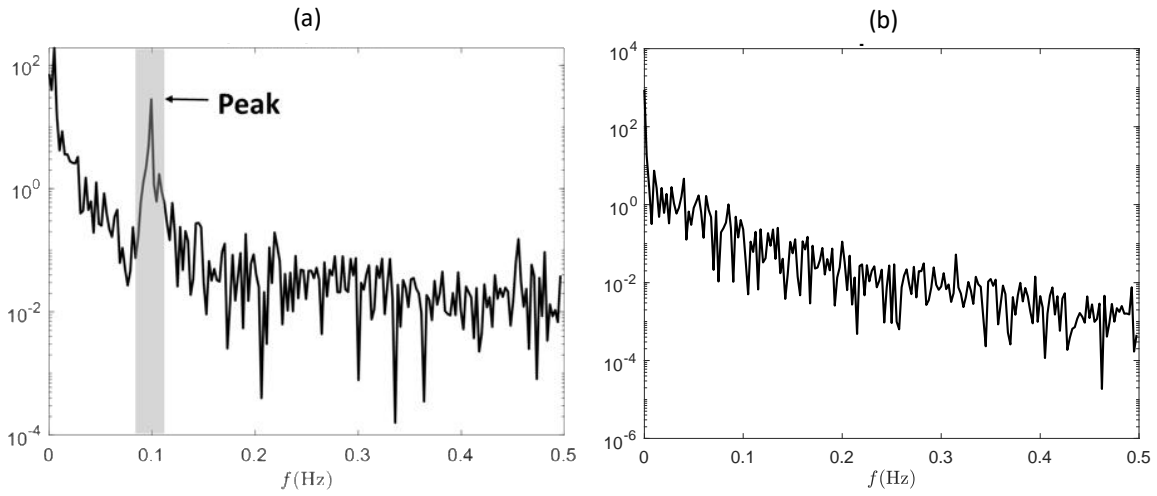


Figure 3.4 Velocity spectrum analysis of the velocities on Figure 3.3

(a) is the velocity spectrum of the abnormal case and (b) is the velocity spectrum of the normal case.

3.2 Turbulent diffusivity estimation

The concentration diffusion in turbulent flow has a similar formation as Fickian diffusion. The turbulent diffusivity could be modeled as the same as the Fick's Law. The flux of diffusion could be modeled as the diffusion term:

$$\overline{w'c'} = -D_z \frac{\partial \bar{c}}{\partial z} \quad (3.2)$$

Where the left term is turbulent particle flux estimated by the covariance of vertical velocity fluctuation w' and particle concentration fluctuation c' , the time series mean concentration is notated as \bar{c} . The turbulent diffusion could represent how strong the turbulent mixing in the height z . By the isotropy and homogenous assumption in the horizontal direction, we could only consider the vertical diffusion in our analysis.

3.2.1 Direct method

The very straightforward method is the direct method, which derived from the definition of turbulent diffusivity (Equation 3.2). Since both the concentration gradient and the turbulent particle flux could be extracted from the PIV velocity map and the particle concentration map, we could estimate the vertical diffusivity directly by

$$D_z = -\frac{\overline{w'c'}}{\partial \bar{c} / \partial z} \quad (3.3)$$

3.2.2 Reynolds averaging method (Covariance method)

The turbulent diffusivity of momentum transferring could be written in the same format as the mass diffusivity. Following the turbulent-viscosity hypothesis, the turbulent viscosity can be estimated by

$$\nu_T = -\frac{\overline{u'w'}}{\partial U/\partial z} \quad (3.4)$$

Where $\overline{u'w'}$ is the Reynolds shear stress. Liao (Liao et al., 2009) claimed that the eddy viscosity and the turbulent diffusivity have the same order magnitude, the turbulent diffusivity D_z is proportional to the turbulent viscosity ν_T , so we could use the eddy viscosity for estimating the turbulent diffusivity as well.

However, by checking the mean velocity profiles, the lake bottom flow profile often has the profiles with too many turning points, which makes most cases unable to apply this method, so we gave up using the method in this thesis.

3.2.3 k-epsilon method

The k-epsilon method is the improvement of the mixing length method, and it is the most widely used model in Computational Fluid Dynamics for turbulent flow conditions (Pope 2000; Launder and Spalding, n.d.1974). By assuming that the turbulent viscosity is isotropic, in other words, the turbulent viscosity is the same in all directions, the eddy viscosity (turbulent viscosity) was approximated as:

$$\nu_T = C_\mu \frac{k^2}{\varepsilon} \quad (3.5)$$

Where C_μ is a constant equal to 0.09, k is the turbulent kinematic energy (TKE), ε is the TKE dissipation rate.

However, the isotropy assumption is not strictly established here, especially in the region near the bottom. It is expected that the $k - \varepsilon$ method has a better estimation for where far from the bottom than where the near bottom.

3.3 TKE and Reynolds stress estimation

For applying the methods introduced in the above sections for the turbulent diffusivity estimation, the Reynolds stress, TKE, and covariance of concentration and vertical velocity fluctuation were required. The method for calculating the parameters will be discussed in this section.

Reynolds decomposition is a mathematical technique that can separate the fluctuation from the time-average value. The definition of Reynolds decomposition of u is

$$u = u' + \bar{u} \quad (3.6)$$

Where u' is the fluctuation and the \bar{u} is the time-averaged velocity component. The Reynolds stress is defined as $R_{ij} \equiv \overline{u'_i u'_j}$, which is the covariance of the velocity fluctuations.

3.3.1 Random wave-induced fluctuation removal

Accurate estimation of Reynolds stresses and TKE in the coastal ocean are difficult due to the inherent complications associated with separating surface wave-induced unsteady motions from the turbulence. The wave-induced component of the fluctuations includes contributions from both surface and internal waves. It is not always practical to separate the two different fluctuations in natural flow since both of them are random. Following the Hussain's decomposition (Hussain and Rees, 1995) instead of Reynolds' decomposition, the velocity component u could be decomposed as

$$u = \bar{u} + \tilde{u} + u' \quad (3.7)$$

Where the additional term \tilde{u} is the wave-induced part.

3.3.2 Low-pass filtering method

There are many ways to define the combined part of the mean velocity and wave-induced fluctuation, the very straightforward way is by applying the low-pass filtering to the time series of the velocity, because the random wave-induced fluctuation might have a lower frequency compared to the turbulence.

Figure 3.5 shows the time series of the horizontal velocity u in one 400s measurement at the height of 5cm above the bottom, the lowpass filtered dotted velocity curve and linear fitted dash line shows that the wave-induced fluctuation do happen in the measurement of the profundal area of Lake Michigan, but compared to the ensemble flow like tide flow which usually can fit with an ensemble sinusoid curve, the fluctuation in the measurements of this thesis is more random.

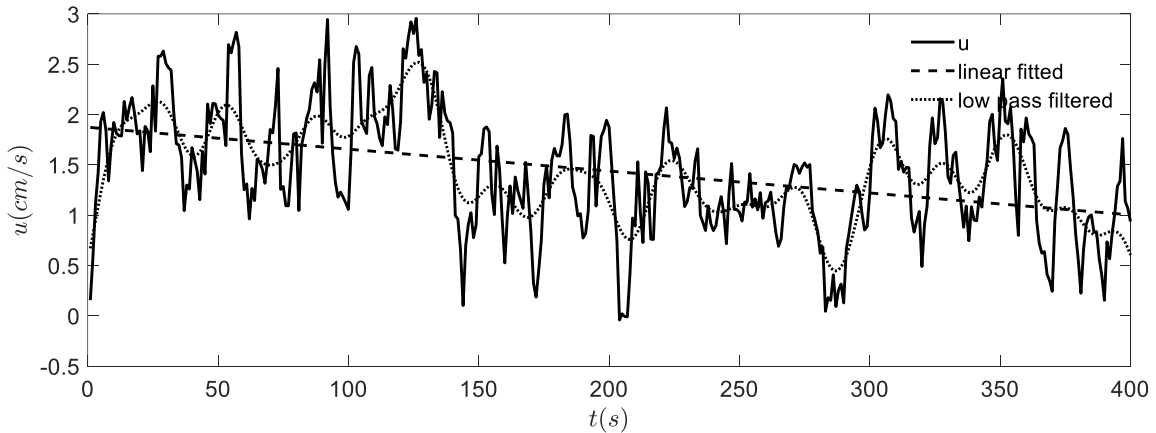


Figure 3.5 Time series of the streamwise velocity at $z = 5$ cm from data set AW55-0023. The dotted line represents the lowpass filtered ($= 50$ s) velocity signal. The solid line is the horizontal velocity, where the dashed line and the dotted line are lowpass filtered and linear regressed velocities. The sample rate is 1Hz.

By applying the Hussain decomposition to the Reynolds stress (Nayak et al., 2015), we have

$$\overline{u_i' u_j'} = \overline{(u_i - \bar{u}_i - \tilde{u}_i)(u_j - \bar{u}_j - \tilde{u}_j)} \quad (3.8)$$

By applying the lowpass-filtered time-series of velocity as the sum of mean velocity and the wave-induced velocity

$$\bar{u}_i + \tilde{u}_i \approx u_{i(\text{lowpassfiltered})} \quad (3.9)$$

The Reynolds stress could be derived as

$$\overline{u_i' u_j'} = \overline{(u_i - u_{i(\text{lowpassfiltered})})(u_j - u_{j(\text{lowpassfiltered})})} \quad (3.10)$$

In later discussion, the method was named as the “lowpass filter method” in this thesis for convenience. however, in actual data processing, we applied the moving average for the filtering, which is recognized as one of the standard approaches in related research papers (Nimmo Smith et al., 2002). Figure 3.6 shows the comparison of the result by using the lowpass filter method and the method without removing the wave-induced fluctuation. It is not surprising that the Reynolds normal stresses are in large difference, the removing wave-induced oscillating process decreased the value significantly. But Figure 3.6(a) shows that the reductions are varied for the near-bottom region and the top region of the set of data; the reason might be that the wave-induced fluctuation contributed different proportions in the different elevations.

Figure 3.6(b) shows that the Reynolds shear stress smaller difference for the two methods, the low-pass filter method reduced the Reynolds shear stress estimation on the top ($z > 10\text{cm}$) which is the same as the Reynolds normal stress, but there is an increase on the bottom which is abnormal to the intuition. However, it is pointless to compare the result by only one specific dataset since the flow condition in our research site, and the correlation analysis will be carried out in the next sections with the whole datasets.

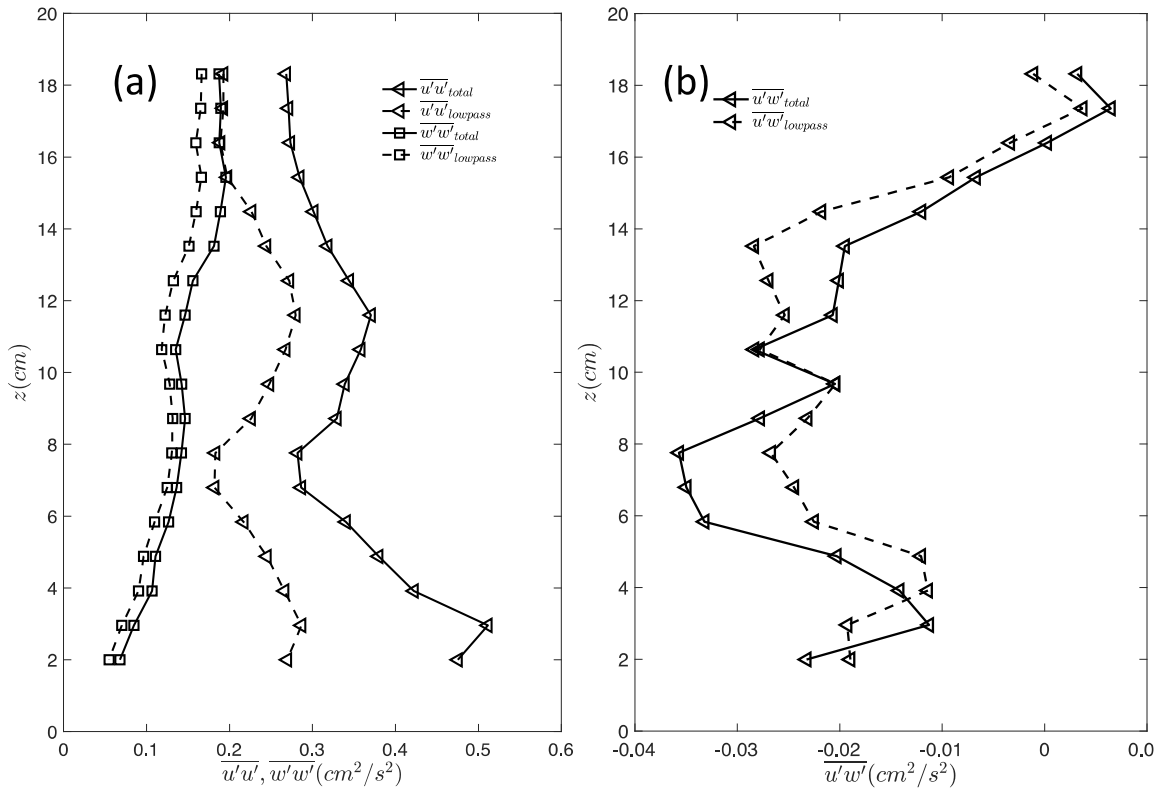


Figure 3.6 Reynolds normal stress calculated from mean velocity and low pass velocity. (a) (b) are the comparison of the Reynolds normal stress $\overline{u'u'}$, $\overline{w'w'}$. The Reynolds stresses profile were spatially averaged in the horizontal direction. From the comparisons, the fluctuation calculated from the low pass filtered velocity is smaller than from the mean velocity, which implied that the low-frequency fluctuation, which probably came from waves, indeed influences the Reynolds stress estimation.

In sum, the lowpass filter method is one of the very straightforward methods applied in the Reynolds stress calculation with wave-induced fluctuations. It is widely applied in some cases with ensemble waves i.e. tidal flows. However, in the profundal area of Lake Michigan bottom, the waves are mostly random, the filter size needs to be carefully selected.

3.3.2.1 Data processing procedures

In applying the lowpass filter method in the data batch processing, we did not follow the exact procedures mentioned above for convenience. Instead of smoothing the 3D matrix (time series of 2D velocity map), the spatial average in the horizontal direction was conducted before the moving average procedure. The 3D matrix was reduced to a 2D matrix which significantly saved the computation and storage space in the data processing. The spatial averaging is equivalent to a lowpass filtering applied in time series if assuming the flow is homogeneous in the horizontal direction.

The procedures of the data processing could be summarized as below and shown in Figure 3.7.

1. Calculate the instantaneous mean velocity profile by averaging the rows of the instantaneous velocity map, save the velocity profile to a 2D matrix, which is the history of the mean velocity profile.
2. Smooth the 2D matrix in the time series direction with the different filtering size(5s,9s,11s)
3. Expand each filtered profile history to a 2D velocity map, which is the approximation of the sum of mean velocity and wave-induced fluctuation.
4. Subtract the filtered velocity map from the instantaneous velocity map,

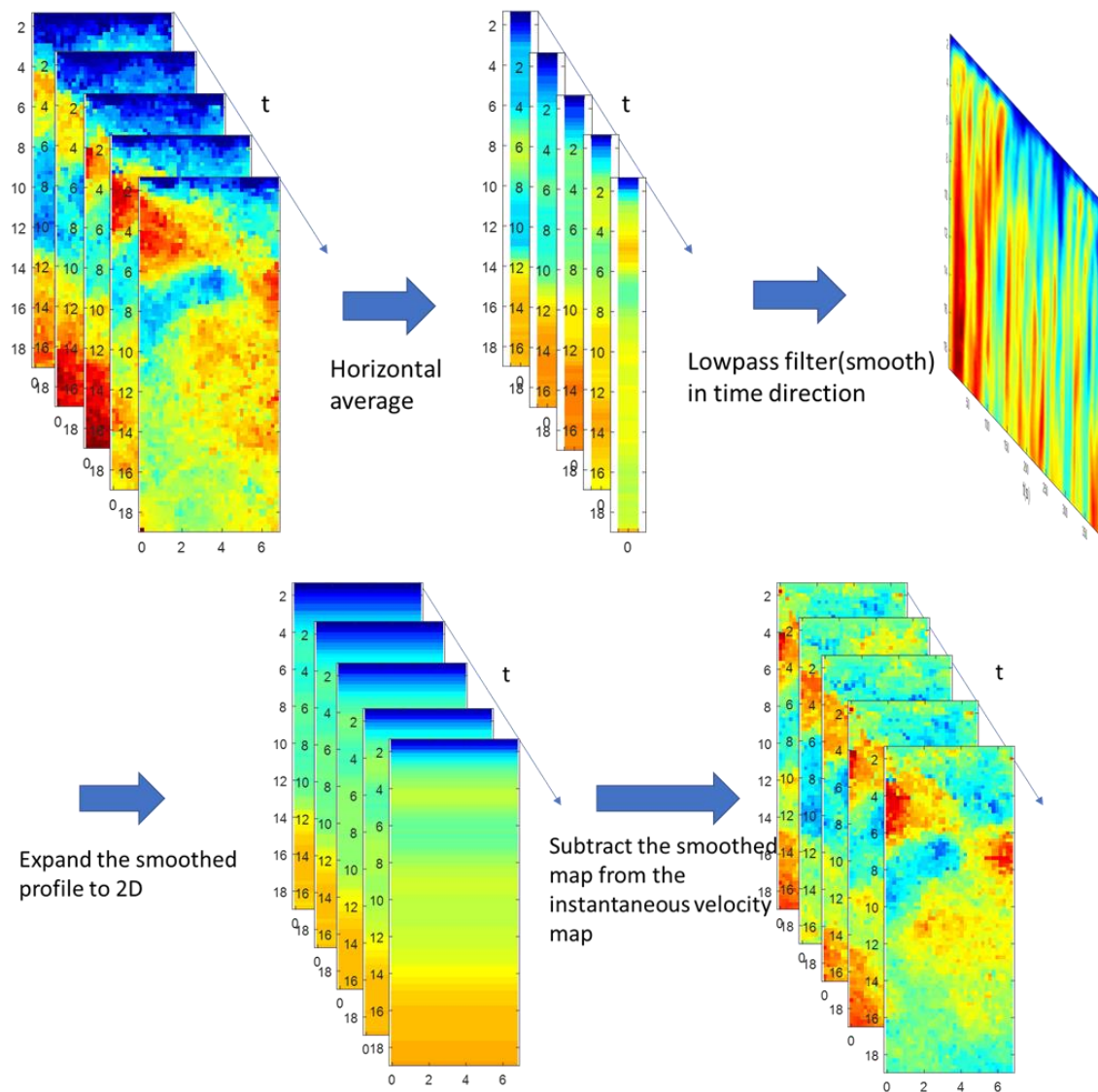


Figure 3.7 Lowpass method data processing steps

3.3.3 Second-order structure function method

Nimmo Smith (Nimmo Smith et al., 2002) introduced the second-order structure function method by taking advantage of the 2-D velocity map provided by PIV. This method was followed by the idea from Trowbridge (Trowbridge, 1998). In Trowbridge's paper, the difference of the velocities measured in two different points with the distance of r_i was defined

as $\Delta u_i = u_i(x_i + r_i) - u_i(x_i)$. The second-order velocity structure function is defined as the covariance of difference in velocities between two points,

$$D_{ij} = \text{cov}[\Delta u_i, \Delta u_j] = \overline{[u_i(x_i + r_i) - u_i(x_i)][u_j(x_i + r_i) - u_j(x_i)]} \quad (3.11)$$

by assuming the horizontal homogeneity, the turbulence parameters in different points in horizontal direction should be in the same, then

$$\overline{u_i(x_i + r_i)u_j(x_i + r_i)} = \overline{u_i(x_i)u_j(x_i)} \quad (3.12)$$

$$\overline{u_i(x_i)u_j(x_i + r_i)} = \overline{u_i(x_i + r_i)u_j(x_i)} \quad (3.13)$$

By substituting (3.12) (3.13) to (3.11), the covariance can be simplified as:

$$\text{cov}[\Delta u_i, \Delta u_j] = 2\overline{u_i(x_i)u_j(x_i)} - 2\overline{u_i(x_i + r_i)u_j(x_i)} \quad (3.14)$$

Decomposing the u_i by Hussain decomposition (Equation(3.8)) and substituting in Equation (3.14), and assuming there's an negligible correlation between the turbulent fluctuations and the wave-induced oscillations, i.e. $\overline{u_i' \tilde{u}_j} \approx 0$. Equation (3.14) could be derived as

$$\begin{aligned} \text{cov}[\Delta u_i, \Delta u_j] = & 2(\overline{u_i'(x_i)u_j'(x_i)} + \overline{\tilde{u}_i(x_i)\tilde{u}_j(x_i)}) - \\ & 2(\overline{u_i'(x_i + r_i)u_j'(x_i)} + \overline{\tilde{u}_i(x_i + r_i)\tilde{u}_j(x_i)}) \end{aligned} \quad (3.15)$$

In this thesis, if the PIV ROI size is much smaller than the wavelength (Nimmo Smith et al., 2002), the wave-induced terms could be canceled out.

$$\text{cov}[\Delta u_i, \Delta u_j] = 2\overline{u_i'(x_i)u_j'(x_i)} - 2\overline{u_i'(x_i + r_i)u_j'(x_i)} \quad (3.16)$$

In the second term of Equation(3.16), $u_i'(x_i + r_i)$ and $u_j'(x_i)$ are statistically uncorrelated when the r_i is larger than the integral length scale. So, the second term will converge to zero when the r_i reached the integral length scale.

If the distance of the two points r_i meet the conditions that: (1) $r_i \ll \gamma$; and (2) $r_i > l$, where γ is the wavelength of the wave, and l is the integral length scale. The Reynolds stress can be estimated by the second-order structure-function,

$$\overline{u'^2} = \frac{1}{2}D_{11}(r), \overline{w'^2} = \frac{1}{2}D_{33}(r), \overline{u'w'} = \frac{1}{2}D_{13}(r) \quad (3.17)$$

Figure 3.8 shows the structure functions D_{11} , D_{33} and D_{13} with respect to the distance of the two measured points on the velocity map. Figure 3.8(a) show good convergence for the height of $z = 3\text{cm}$ and $z = 4\text{cm}$ at $r_1 = 4.5\text{cm}$ and 5cm , the situation that $z=3\text{cm}$ converged early than the $z = 4\text{cm}$ matches the theory that the convergence is depended on the integral length scale, which here we can approximate as the distance from the bottom (Nayak et al., 2015). Thus, for $z = 3\text{cm}$ and $z = 4\text{cm}$, the integral length scale is smaller than the maximum value of r_1 , the convergence will show in the structure function curve, while for $z = 6\text{cm}$ and 8cm , the integral length scales increased to the value larger than the width of the PIV measurement, which means the convergence will not show in the structure-function curve.

In Figure 3.8(b), the structure-function D_{33} is relatively nosier than the D_{11} , but there still exist a flat region on the structure-function curve with the heights of $z = 3\text{cm}$ and $z = 4\text{cm}$, the plateau intervals are considered as the convergence region. Figure 3.8(c) shows the structure-function D_{13} with respect to r_1 , the D_{13} is much nosier than D_{11} and D_{33} , there's not a clear convergence region on the curve. In the data batch processing of all datasets, it is not possible to find the convergence region of the curve manually, so the convergence region was approximated set as the last five points of the structure-function, and the converged value of the structure-function is approximately estimated as the mean value of the last five points.

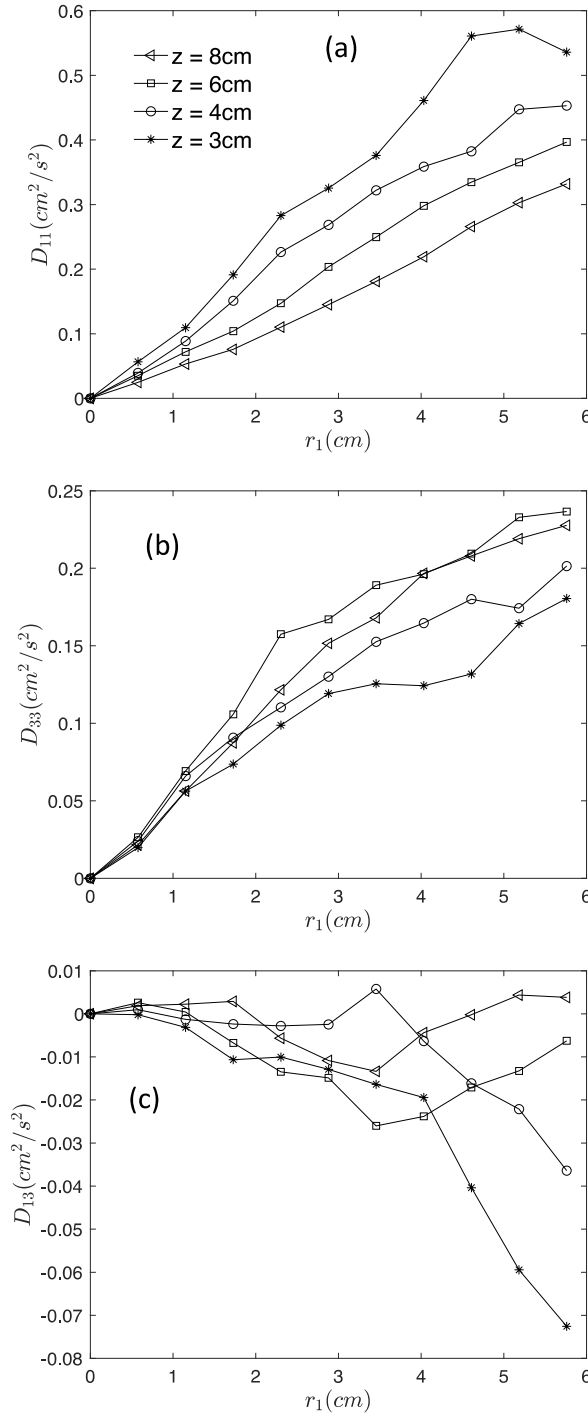


**Figure 3.8 Structure function $D(r_1)$ at $z = 3\text{cm}$, 4cm , 6cm and 8cm .
 (a) $D_{11}(r_1)$, (b) $D_{33}(r_1)$, (c) $D_{13}(r_1)$. The result was subtracted from AW55-0023 dataset.**

As mentioned above, the width of the UWPIV is not sufficiently large for the structure method, we still apply the method in estimating the Reynolds stress. Figure 3.9 shows the

comparison of the structure method and the lowpass method. The lowpass method reduced the value of the stress in both the two normal stresses ($\overline{u'u'}$ and $\overline{w'w'}$) in all elevations, but the structure-function method reduced more values on the top part of the curve. By tracking back to the structure-function, the reason might be that the structure-function didn't reach the convergence region in our measurement, then the structure function method might have the underestimated result at the height $z > 10\text{cm}$ by theoretical analysis. Figure 3.9 (c) shows the result of the Reynolds shear stress, the Reynolds shear stress by the structure-function also estimated a smaller value at the top comparing to the near-bottom region.

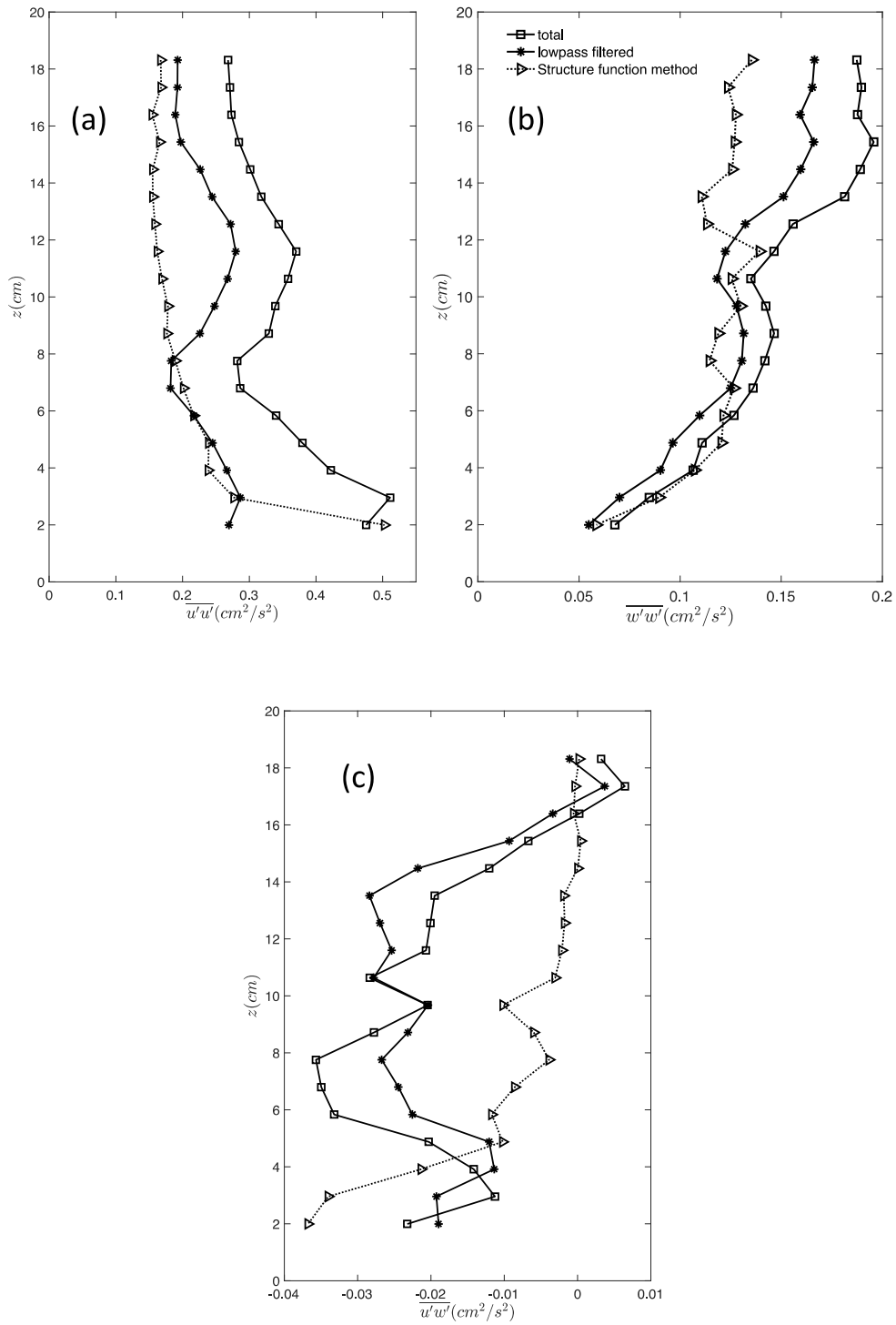


Figure 3.9 (a)(b) Reynolds normal stress and (c) Reynolds shear stress by second-order structure function method and the lowpass filter method.

3.3.4 Correlation analysis

The two methods introduced in 3.3.2 and 3.3.3 both have the advantage and the weakness in calculation of the Reynolds stress in the situation with the random wave. Preliminary comparison and analysis of the two methods were carried out in 3.3.3 for one typical dataset, however, the comparison needs to be carried out statistically for the whole datasets.

3.3.4.1 Turbulent kinetic energy (TKE) calculation

For evaluating and selecting the best method for our application, we applied the lowpass filter method and the Second-order structure function method in the TKE and Reynolds stress estimation. The definition of TKE is

$$TKE = \frac{1}{2} \left(\overline{u' u'} + \overline{v' v'} + \overline{w' w'} \right) \quad (3.18)$$

Which could be calculated from the Reynolds normal stress. In the 2D-PIV measurement, we have the $\overline{u' u'}$ and $\overline{w' w'}$. By assuming the homogenous and isotropy turbulence, we can approximately estimate the missing Reynolds normal stress $\overline{v' v'}$ as

$$\overline{v' v'} = \frac{1}{2} \left(\overline{u' u'} + \overline{w' w'} \right) \quad (3.19)$$

Then the TKE could be calculated by the equation

$$TKE = \frac{3}{4} \left(\overline{u' u'} + \overline{w' w'} \right) \quad (3.20)$$

To compare the two different methods and optimize the filter size, we calculated and plotted all datasets measured. Because the structure-function method may have different performance in the different heights, the top ($z > 10\text{cm}$) and bottom ($z = 2 \sim 5\text{cm}$) were plotted and analyzed separately.

Figure 3.10 is the comparison of the TKE estimation, the filtering size increased from (a) to (d). The overall TKEs estimated by the lowpass filter is smaller compared to the structure-function method. The dashed lines in the figures are the linear fitted results, the slope of the linear fitted lines decreases as the filter size increases, which is because larger filtering size represents the less fluctuation remained in the subtracted portion, then more fluctuations kept in the result. As using the structure-function method as the reference, it is more scattered while the lowpass filter size increased, but the slope is closer to one while with the filter size increasing. We also observed that there is a bifurcation occurred at the low dissipation rate location, this abnormal happened also with the filter size increased. The slopes of the linear regression were listed in Table 3.1. A trade-off for the filter size selection has been made because there are many side effects while increasing the filter size. In this thesis, the filter size of 9 s was selected for the filtering because the filter size is not too scattered but the linear fitted slope close to one.

Table 3.1 List of the slopes of the linear regression in Figure 3.10

Filter size	1s	5s	9s	11s
Z = 2~5cm	1.92	1.66	1.41	1.33
Z > 10cm	1.93	1.66	1.41	1.33

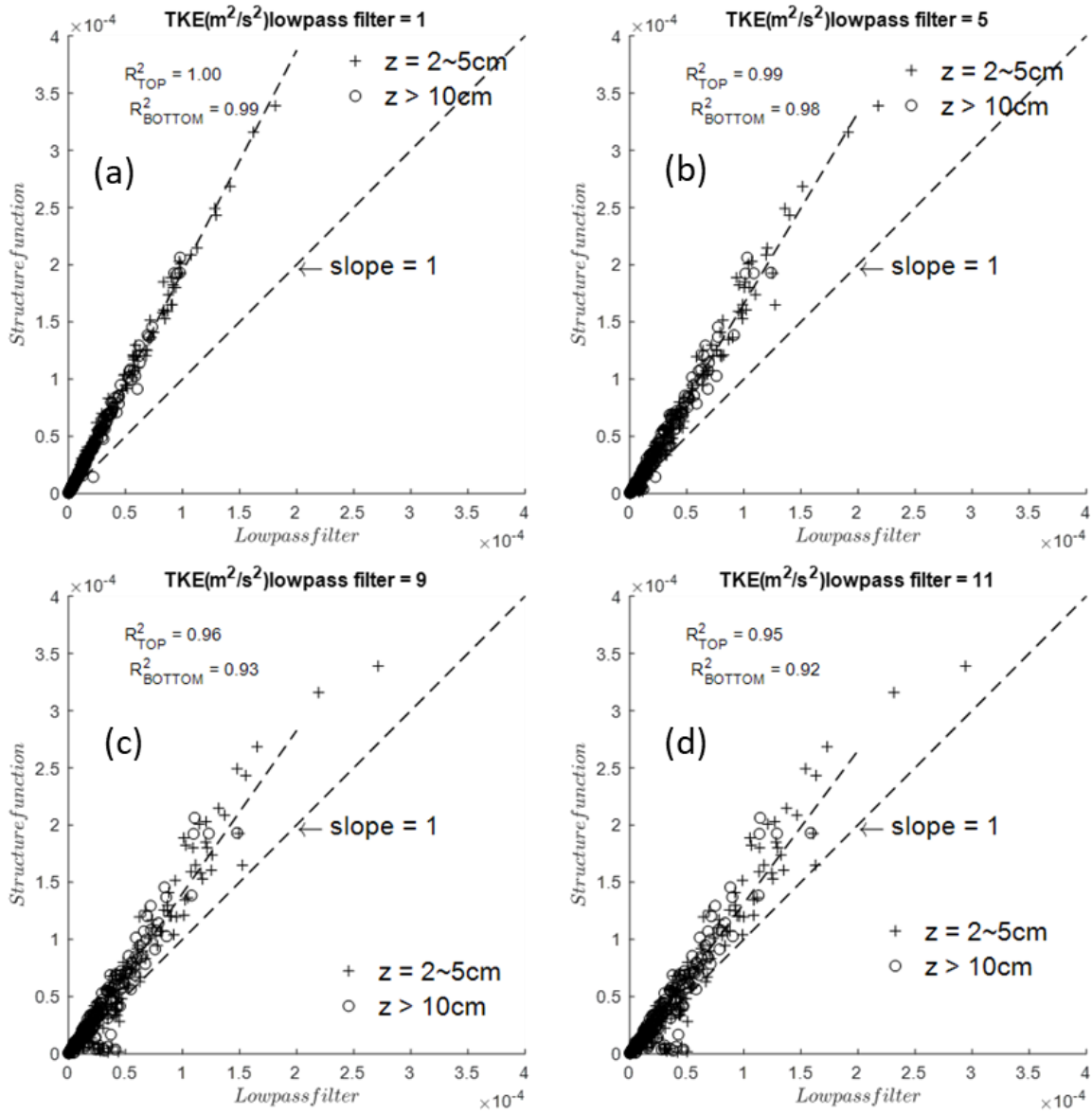


Figure 3.10 TKE comparison of the lowpass filter method and the structure function method, (a) lowpass filter =1, (b) lowpass filter = 5, (c) lowpass filter = 9, (d) lowpass filter = 11.

Figure 3.11 shows the Reynolds shear stress $\overline{u'w'}$ comparison between the structure method and the lowpass filtering method. The trend of the Reynolds shear stress comparison is very similar to the TKE comparison, the slope of the linear regression decreased and the comparison turned to be scattered while the filter size increased.

However, the slope of the linear regression of the lower level elevation and the higher level elevation slightly differs. The slope of the top is larger than the bottom in Figure 3.11(a) but the result in Figure 3.11(d) is reversed, which means the decrease speed of the top-level line is faster than the bottom level line while the lowpass filter size increased.

This result indicated two possible conclusions, one is the wave-induced fluctuations do not the same in different elevations, while the second is that the structure-function method has the different performance in wave removal in different elevations. It is hard to tell which conclusion is correct. Here we followed the same procedures as the TKE calculation and made a trade-off between the different methods, and chose the lowpass filter method with filter size = 9 s as the final method.

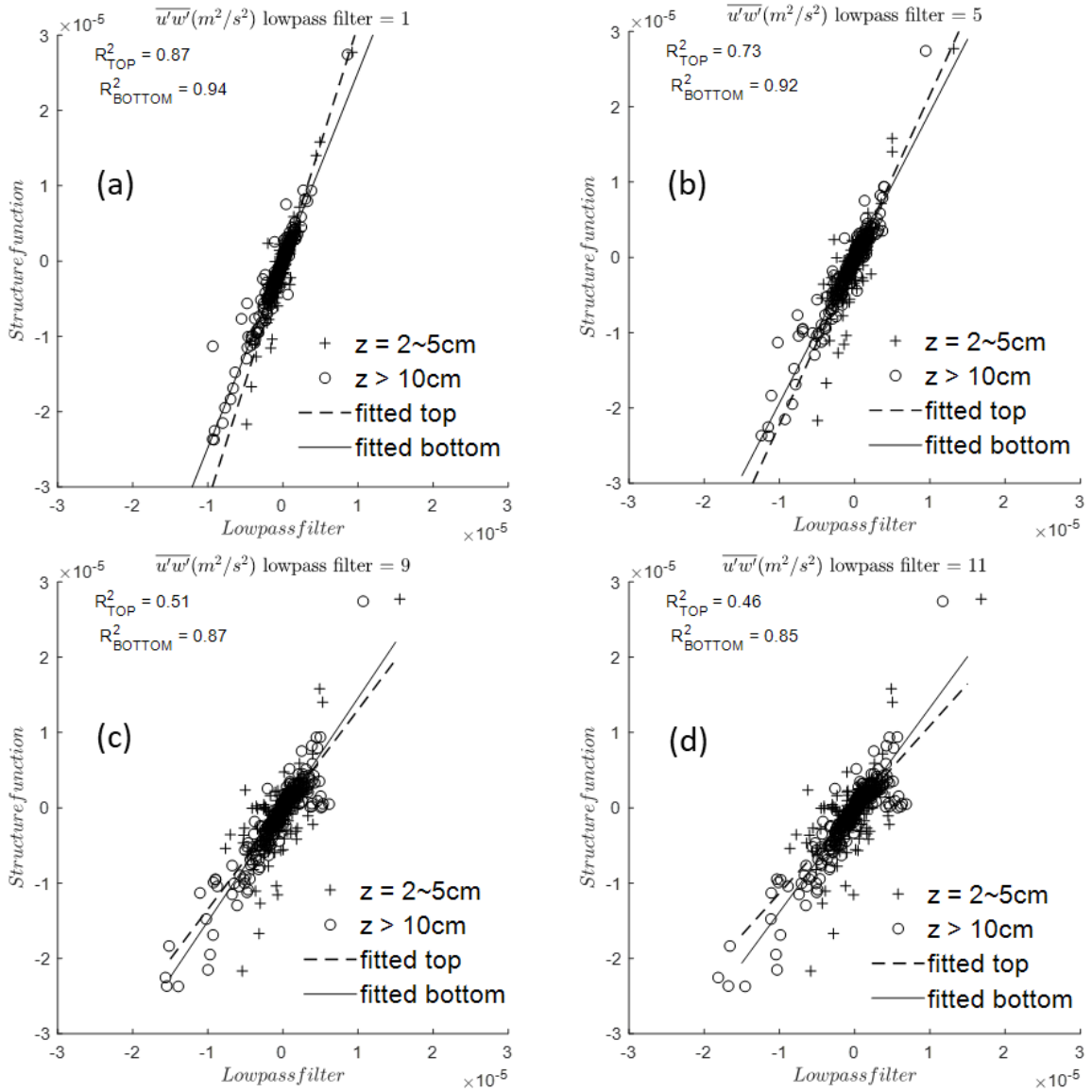


Figure 3.11 Reynolds shear stress comparison of the lowpass filter method and the structure function method.
(a) only spatial filter without lowpass, (b) lowpass filter = 5 s, (c) lowpass filter = 9 s, (d) lowpass filter = 11 s.

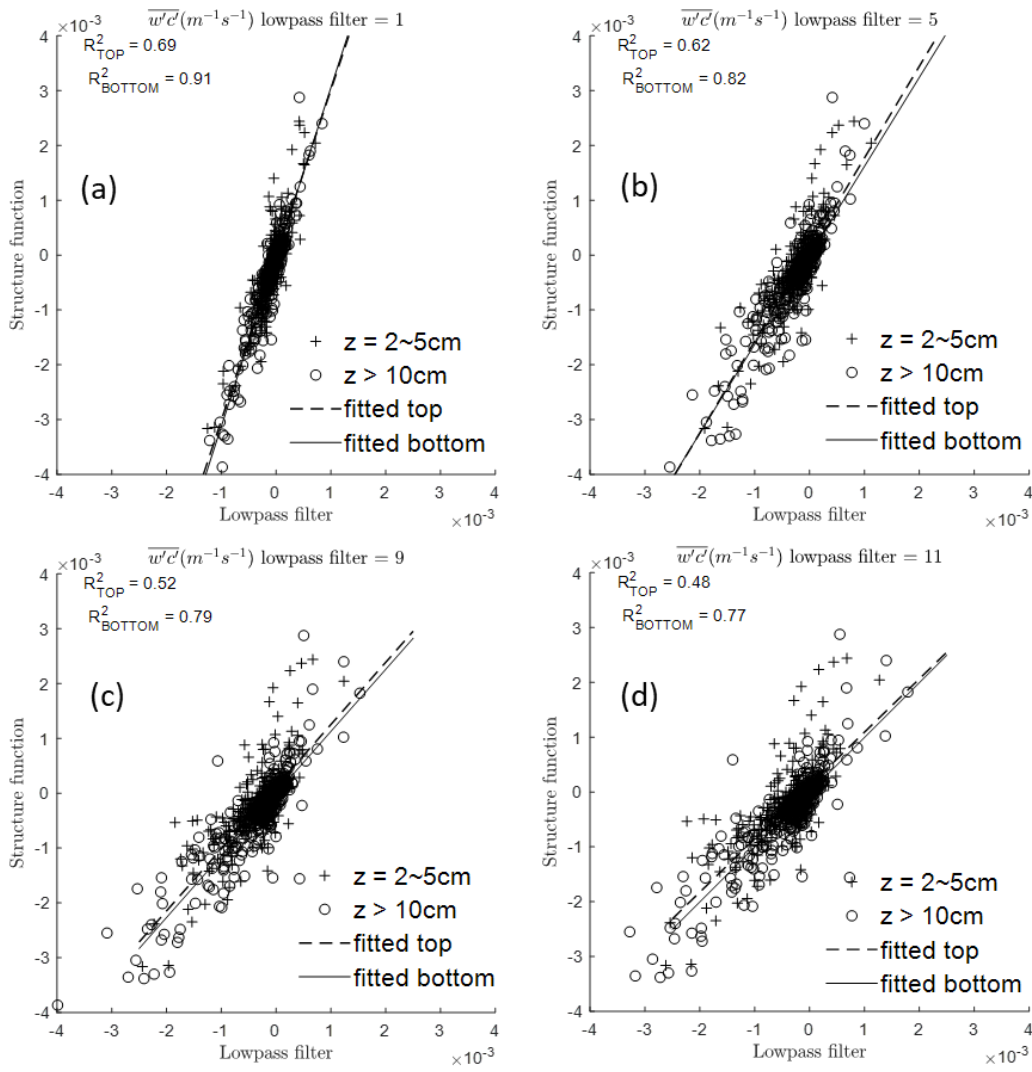


Figure 3.12 Particle concentration flux $w' c'$ estimation comparison of the lowpass filter method and the structure function method.
(a) lowpass filter = 1s, (b) lowpass filter = 5 s, (c) lowpass filter = 9 s, (d) lowpass filter = 11 s.

Figure 3.12 shows the comparison of the particle concentration flux estimated by structure-function method and the lowpass filter method, the result is similar to the Reynolds shear stress, but compared to the Reynolds shear stress result, the data are more scattered when applying the lowpass filter, the reason might be the particle concentration counting result is a bit of noisy compared with the velocity. The same lowpass filter method with filter size = 9 s was selected for the particle concentration flux estimation.

By summarizing all the comparisons, the lowpass filter method with filter size = 9s is selected by the reason of robust and good correlation with the structure-function method. Although there are some shortcomings of the method in some cases, this is already the best solution we have tried to find.

3.4 TKE dissipation rate estimation

For the k-epsilon method introduced above, the TKE dissipation rate needs to be estimated from the velocity maps for the diffusivity calculation. And determining the vertical profile of the dissipation rate is of interest as it relates to the mixing process in the surface layer. The TKE dissipation rate, which denoted as ε , is the rate of the TKE dissipated to heat in turbulent flow. However, in the literature, there's no general agreement as to be the best method to estimate the TKE dissipation rate from the velocity maps measured by PIV; The TKE dissipation rate is defined as (Pope, 2000)

$$\varepsilon = 2\nu \langle s_{ij} s_{ij} \rangle = \nu \left\langle \frac{\partial u_i}{\partial x_j} \frac{\partial u_i}{\partial x_j} + \frac{\partial u_j}{\partial x_i} \frac{\partial u_i}{\partial x_j} \right\rangle \quad (3.21)$$

Where the s_{ij} is the rate-of-strain tensor, u_i is the fluctuation of velocity in i^{th} direction. In this section, we will describe how we apply several common approaches to estimate the turbulent energy dissipation rate from PIV measurement. In the next four sections, four different methods will be introduced for estimating the dissipation rate from PIV 2D velocity maps.

3.4.1 Direct method

The TKE dissipation rate could be estimated “directly” from the instantaneous 2D in-plane velocity gradients which extracted from the PIV data. Five terms of the equation could be calculated by the spatial velocity derivative directly: $\left(\frac{\partial u}{\partial x}\right)^2$, $\left(\frac{\partial w}{\partial z}\right)^2$, $\left(\frac{\partial w}{\partial x}\right)^2$, $\left(\frac{\partial u}{\partial z}\right)^2$, $\left(\frac{\partial w}{\partial x} \frac{\partial u}{\partial z}\right)$.

$\left(\frac{\partial v}{\partial y}\right)^2$ could be estimated by the continuity equation:

$$\left(\frac{\partial v}{\partial y}\right)^2 = \left(-\frac{\partial u}{\partial x} - \frac{\partial w}{\partial z}\right)^2 \quad (3.22)$$

By assuming the mean of missing out-of-plane cross gradients is equal to their in-plane gradients by Hinze (J. O Hinze, 1987)

$$\varepsilon_{D1} = 4\nu \left[\overline{\left(\frac{\partial u}{\partial x}\right)^2} + \overline{\left(\frac{\partial w}{\partial z}\right)^2} + \overline{\frac{\partial u}{\partial x} \frac{\partial w}{\partial z}} + \frac{3}{4} \overline{\left(\frac{\partial u}{\partial z} + \frac{\partial w}{\partial x}\right)^2} \right] \quad (3.23)$$

Or (Doron et al., 2001).

$$\varepsilon_{D2} = 3\nu \left[\overline{\left(\frac{\partial u'}{\partial x}\right)^2} + \overline{\left(\frac{\partial w'}{\partial z}\right)^2} + \overline{\left(\frac{\partial u'}{\partial z}\right)^2} + \overline{\left(\frac{\partial w'}{\partial x}\right)^2} + 2 \overline{\frac{\partial u'}{\partial z} \frac{\partial w'}{\partial x}} + \frac{2}{3} \overline{\frac{\partial u'}{\partial x} \frac{\partial w'}{\partial z}} \right] \quad (3.24)$$

Where the water viscosity $\nu = 1.5 \times 10^{-6} m^2/s$ in around 5°C near the deep lake bottom. In this thesis, dissipation rate estimated by Equation (3.23) and (3.24) were denoted as ε_{D1} and ε_{D2} . Figure 3.13 shows the dissipation rate calculated by Hinze’s method (ε_{D1}) (Figure 3.13(a)) and Doron’s method (ε_{D2}) (Figure 3.13 (b)). The result shows that these two methods have similar results, their differences are very subtle. The values on the edges have relatively large errors, which are caused by the errors in calculating the velocity gradient at the boundaries. The values near the bottom also have relatively large anomalies, by checking back to the original images, these anomalies are located near the mussel siphons where the velocity measurement has

a significant error which can contaminate the gradient. These error values were removed out from the final analysis.

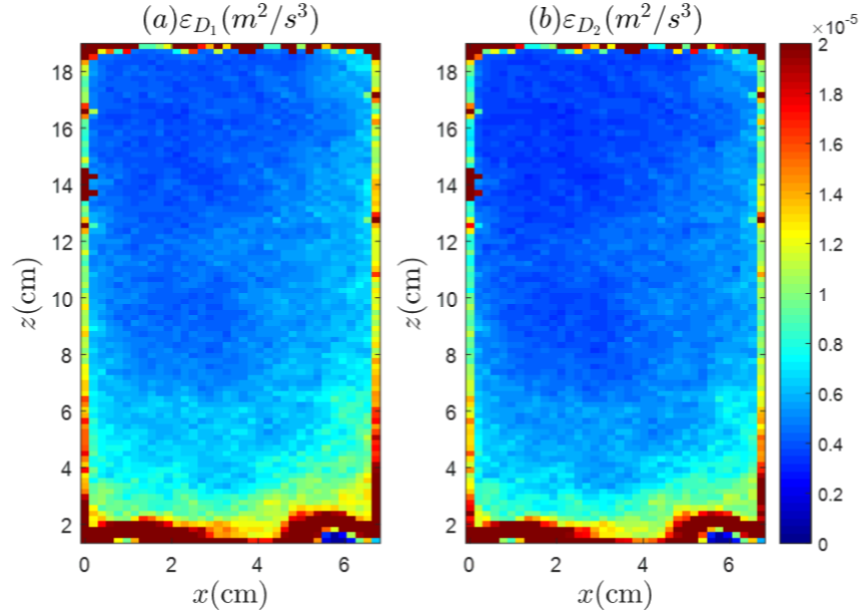


Figure 3.13 (a) TKE dissipation rate calculated by Hinze’s direct method. (b) TKE dissipation rate calculated by Doron’s direct method. The dataset is AW55-0023.

3.4.2 Linear-Fit in Inertial Subrange of a 1-D Velocity Spectra

Assume that turbulence is homogeneous along the streamwise direction, and an equilibrium inertial subrange exists in turbulent velocity spectra, the dissipation rate can be determined by the one-dimensional longitudinal and transverse velocity spectrum E_{11} and E_{33} , which are equivalent to the Fourier transform in the wavenumber space, $\kappa_1 \equiv \frac{2\pi}{x}$, of the autocorrelation function of the streamwise and spanwise velocity fluctuations u' and v' . The dissipation rate can be subtracted by fitting the measured velocity spectrum with the universal -5/3 power law in the inertial subrange (Pope, 2000; Wang and Liao, 2016b),

$$E_{11}(\kappa_1) = \frac{18}{55} \left(\frac{8\varepsilon_{LF}}{9\alpha} \right)^{2/3} \kappa_1^{-5/3} \quad (3.25)$$

$$E_{11}(\kappa_1) \approx \frac{3}{4} E_{33}(\kappa_1) \quad (3.26)$$

Where $\alpha = 1.5$ is a universal constant. Dissipation rate estimated as the best linear fitting parameter to $\log E_{11} \sim \log \kappa_1$ is then denoted as ε_{LF} .

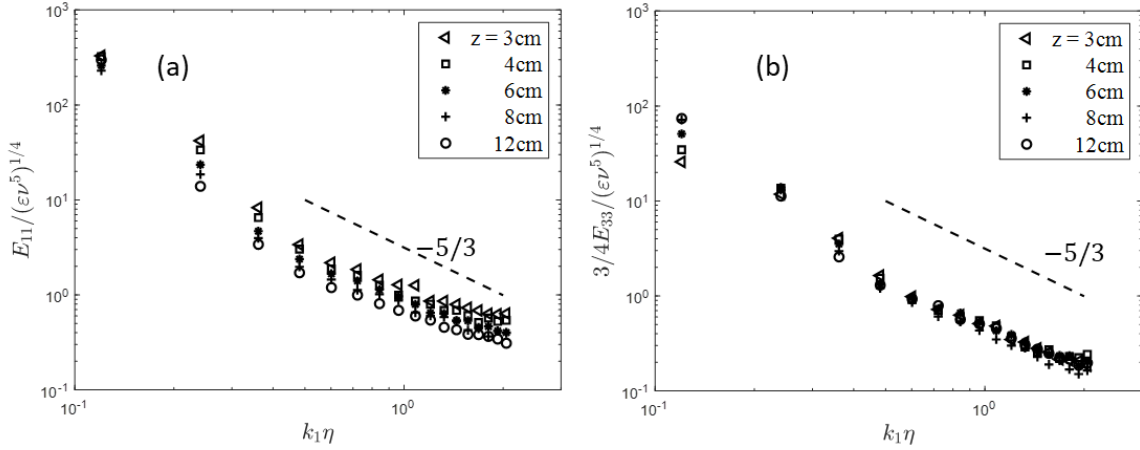


Figure 3.14 Spatial spectral analysis of the velocity.
(a) is the streamwise horizontal velocity spectrum E_{11} , (b) is the streamwise vertical velocity spectrum E_{33} .

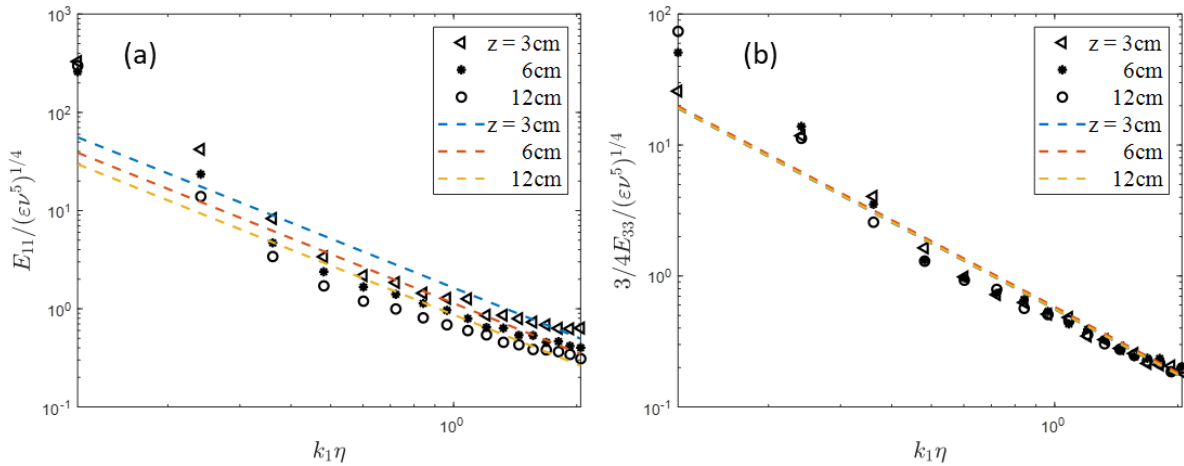


Figure 3.15 log linear fitting of the velocity spectrum.
The dashed lines are the fitted lines.

Figure 3.14 shows the log-log plot of the 1-D horizontal wavenumber spectrum for both horizontal and vertical velocity with Kolmogorov scaling, where the Kolmogorov length scale $\eta = (\nu^3/\varepsilon)^{1/4}$ was estimated from the direct method introduced above. The figure shows fairly good fit with the $-5/3$ slope. Figure 3.15 shows the linear fitting of the log-log wavenumber spectrum, the dashed lines are the linear fitting results. Figure 3.15(a) shows the trend that the

spectrum increased as the z decreased, while the three lines in Figure 3.15(b) are sort of overlapped and don't show there is a significant trend of increasing while the z decreased.

The difference between the vertical and horizontal spectrum results in different distances above the bottom indicates that the near-bottom turbulence flows are anisotropic. By plotting the ratio of the dissipation rate calculated by horizontal and vertical velocity spectrum, Figure 3.16 shows that the ε_{LF11} is larger than ε_{LF33} , while the ratio converged to one while the z increased to the top. This result shows the methods with isotropy assumption might have a significant error in the near-bottom region.

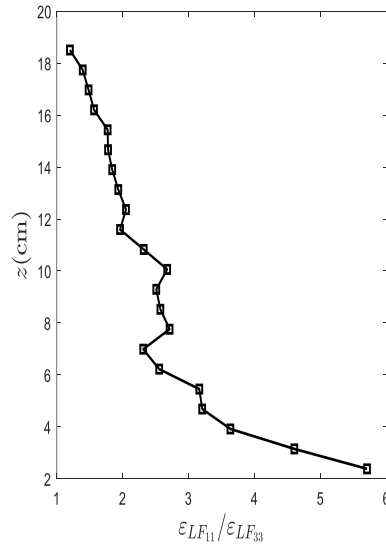


Figure 3.16 Ratio of the linear fitting methods by horizontal and vertical velocity spectrum.

3.4.3 Structure-function fitting method

By following the Kolmogorov's second similarity hypothesis, the second-order structure function follows the equation

$$D_{11}(r) = C_2(\varepsilon_{SF}r)^{2/3} \quad (3.27)$$

$C_2 = 2.12$ (Sreenivasan, 1995) While D_{11} is the second order structure function in Equation (3.11), the dissipation rate ϵ_{SF} (dissipation estimated by structure function) could be estimated by fit Equation (3.27) in the integral length range.

Figure 3.17 shows the structure-function with the linear fitting result; three different levels are plotted in the figure. The trend of the structure functions is fairly well matched with the 2/3 slope lines. The structure-function also shows the trend that the dissipation rate is higher in the bottom than the top as the spectrum method.

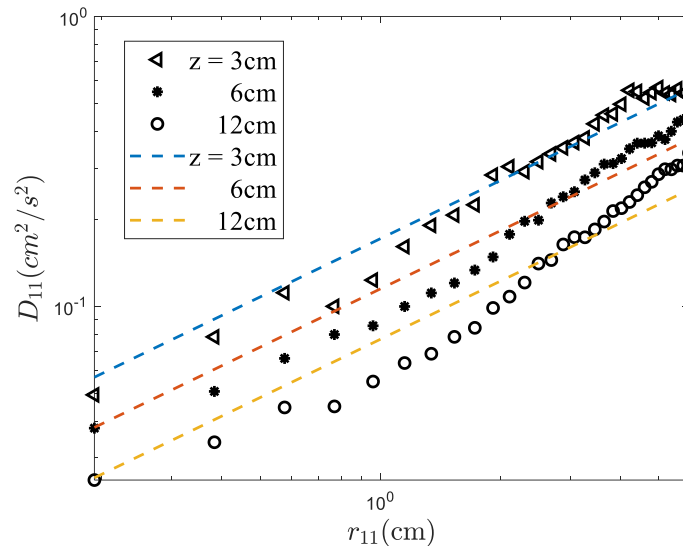


Figure 3.17 Secondary structure-function and the linear fit of the $\log(D_{11})$ and $\log(r_{11})$.

3.4.4 Large Eddy PIV method

The Large Eddy PIV method was first proposed by Sheng et al. (Sheng et al., 2000), following the concept of the Large Eddy Simulation (LES) algorithm in turbulence modeling. Since the PIV applies image correlation on a sub-image window frame with a finite size, it is conceptually equivalent to velocity filtering in LES: the instantaneous velocity u_i ($i = 1, 2$ for 2D PIV measurements) can be decomposed into a PIV-resolved velocity \overline{U}_i , and an unresolved sub-grid scale (SGS) motion \check{u}_i :

$$u_i = \bar{U}_i + \check{u}_i \quad (3.28)$$

Applying the decomposition into the Navier-Stokes equation, the dissipation term can be represented as $2\tau_{ij}\bar{S}_{ij}$, where $\tau_{ij} = \overline{u_i u_j} - \bar{U}_i \bar{U}_j$, is the SGS stress tensor, and the SGS strain rate tensor is:

$$\bar{S}_{ij} = \frac{1}{2} \left(\frac{\partial \bar{U}_j}{\partial x_i} + \frac{\partial \bar{U}_i}{\partial x_j} \right) \quad (3.29)$$

Then the dissipation rate denoted as ε_{LEP} (LEP for Large Eddy PIV method), can be estimated as:

$$\varepsilon_{LEP} \equiv \langle \varepsilon_{SGS} \rangle = -2 \langle \tau_{ij} \bar{S}_{ij} \rangle \quad (3.30)$$

where the operator “ $\langle \rangle$ ” represents ensemble averaging. For the SGS stress tensor estimation, Sheng proposed two models for the experimental applications.

The SGS stress tensor τ_{ij} could be extrapolated from measured 2D surface flow field using the eddy viscosity mode from Smagoristky (Smagoristky,1963)

$$\tau_{ij} = -C_s^2 \Delta^2 |\bar{S}| \bar{S}_{ij} \quad (3.31)$$

where Δ is the interrogation window size and the C_s is a model constant with a value of 0.17 in many LES applications, and

$$|\bar{S}| = \sqrt{2\bar{S}_{ij}\bar{S}_{ij}} \quad (3.32)$$

The model is expected to give a better result in high Reynolds number turbulent flow because it is too dissipative in the laminar region. However, it was also noted that the numerical value of C_s for estimating ε_{LEP} may differ from 0.17 as it depends on the degree of PIV interrogation window overlap, on the way in which spatial gradients are approximated by finite difference, and on which components of the strain tensor are used to estimate \bar{S} (Bertens et al.,

2015). Sheng also mentioned that there's a dynamic method which replaces the C_s to a number obtained depending on the flow structure, but it is not suitable for the PIV measurement.

In our 2D PIV measurement, 5 out of 9 components of SGS strain rate tensor \bar{S}_{ij} can be calculated directly, the other 4 missings could be estimated by continuity and isotropy assumption.

$$\frac{\partial \bar{U}_2}{\partial x_2} = -\frac{\partial \bar{U}_1}{\partial x_1} - \frac{\partial \bar{U}_3}{\partial x_3} \quad (3.33)$$

$$\frac{\partial \bar{U}_1}{\partial x_2} = \frac{\partial \bar{U}_2}{\partial x_1} = \frac{\partial \bar{U}_3}{\partial x_2} = \frac{\partial \bar{U}_2}{\partial x_3} = \frac{1}{2} \sqrt{\left(\frac{\partial \bar{U}_1}{\partial x_3}\right)^2 + \left(\frac{\partial \bar{U}_3}{\partial x_1}\right)^2} \quad (3.34)$$

Then the TKE dissipation rate ε_{LEP} could be calculated by putting the equations above together. Figure 3.18 shows the TEK dissipation rate map calculated by the LEP method, there is a certain similarity between that distribution and the distribution calculated by the direct method, but the average value of the LEP method is about three times of the direct method for this dataset. The outside two layers are with a glaring error value which is from the numerical gradient calculation in the boundary values. The boundary values were cut out in the final analysis as the same as the direct method.

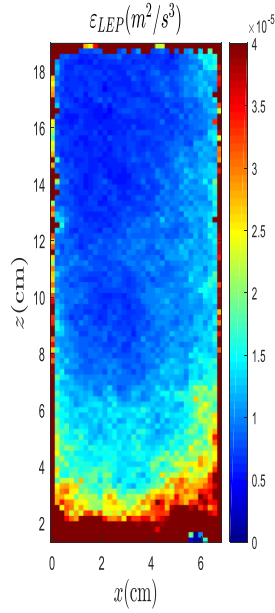


**Figure 3.18 Distribution of TKE dissipation rate ϵ_{LEP} .
Estimated from the dataset AW55-0023.**

3.4.5 Comparison and conclusion

Figure 3.19 shows the comparison between the direct method 1 and the direct method 2, The results of the two methods are correlated very well, and the slope of the fit is close to 1, in the other words, the two methods are consistent. The dashed line and the solid line are with nearly the same slope, indicating that either the top or the bottom estimations are identical for both the methods. The R-squared value of the two linear regressions are both very close to 1. Thus, in the later comparisons, only the first direct method ϵ_{D_1} was selected, because the first direct method is more popular in the literature.

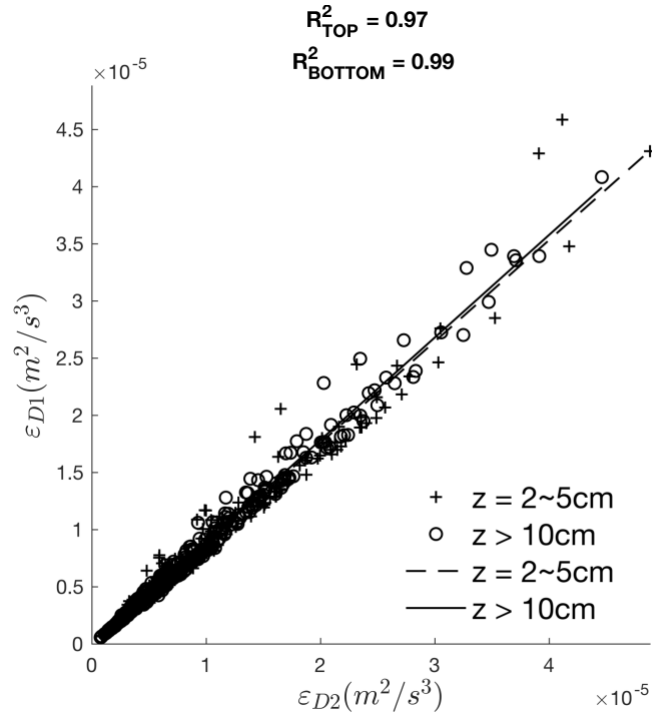


Figure 3.19 Dissipation rate estimation difference between the two direct methods

Figure 3.20 is the comparison between the direct method and the large eddy method, The R-squared value of the linear regression shows that the correlation between the two methods is very good, because they both use the spatial velocity gradient for calculation. But the slope of the linear regression is not close to one, the large eddy method is about one order higher than the direct method. The different results for the two methods is because the two methods don't share the same assumption, the assumption of the direct method is that the resolution of the PIV is high enough for resolving the eddies in the dissipation range while it is assumed that the resolution for velocity gradient calculation is larger than the size of the eddies for the Large-eddy method.

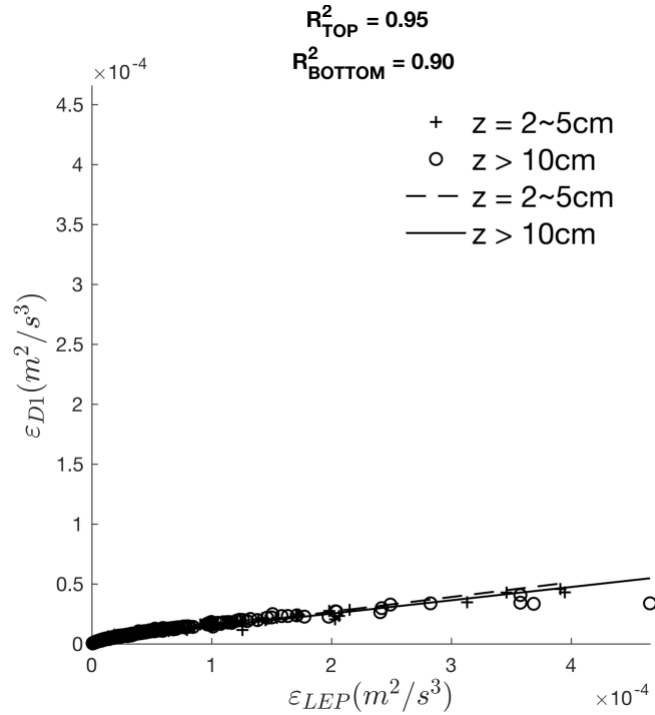


Figure 3.20 Dissipation rate estimation comparison between the direct method and LEP method

Figure 3.21 shows the comparison of the LF_{11} method and the direct method. The correlation between the two methods is also very good, the R^2 is 0.94 for the top points while the R^2 is 0.89 for the bottom points. But the linear fitting method shows a significantly higher value than the direct method. The spectra linear fitting methods require the wave number in the Inertial Subrange(IR), however, the range of wavenumber is around $1/\eta$ (see Figure 3.15), which is on the edge of the IR where the linear fitting might have more errors.

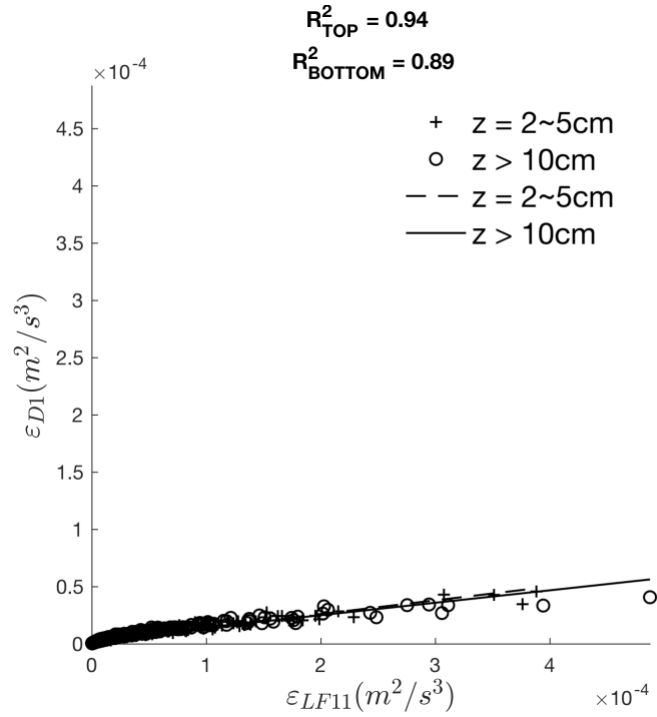


Figure 3.21 Comparison of the direct method and the LF_{11} method

Figure 3.22 shows the comparison between the direct method and the LF33 method; the figure shows that the slope of the linear regression for the bottom and top elevations are different. As the conclusion in (3.4.2), the dissipation rate estimated by the LF33 might be less dissipated near the bottom compared to the LF11 method due to the anisotropy.

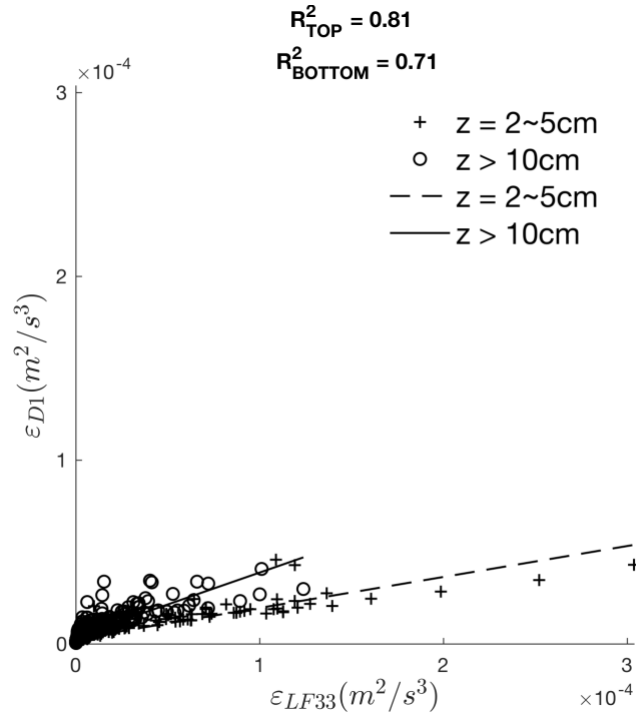


Figure 3.22 Comparison of the direct method and the LF_{33} method

Figure 3.23 shows the direct method is correlated with the structure-function method fairly well, the R^2 values are relatively small, but the two methods shared the same order aptitude. The linear regression of the bottom elevations has a smaller R^2 value compare to the top elevation. The structure-function method requires that the distance is not in the range larger than the integral length scale. It is theoretically possible to cut the part larger than the integral length scale, but it is not doable to select the right range for the fitting manually.

Figure 3.24 shows the comparison between the LEP method and the LF11 method; the figure shows that there is a significant correlation between the two methods. The similarity between the two methods proved that the two methods are statistically identical in the applications; however, this does not necessarily mean that the two methods are suitable in our application.

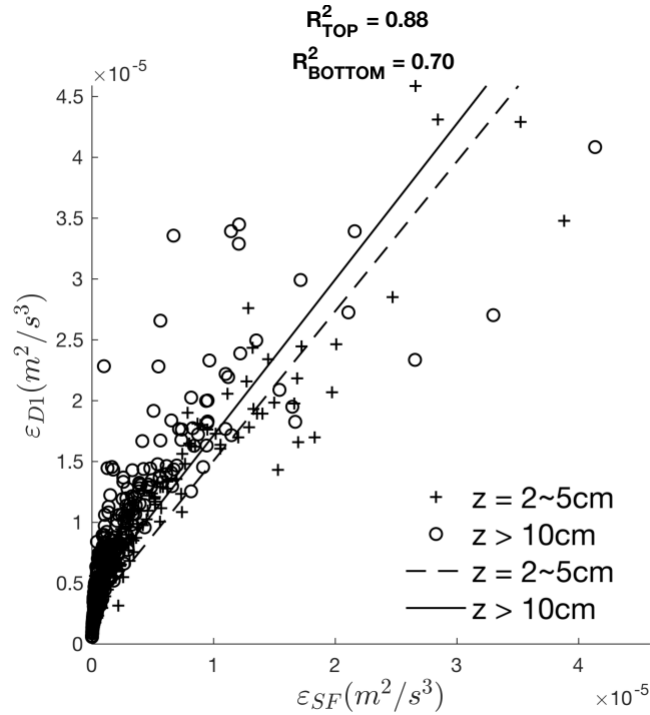


Figure 3.23 Comparison of the direct method and the SF method

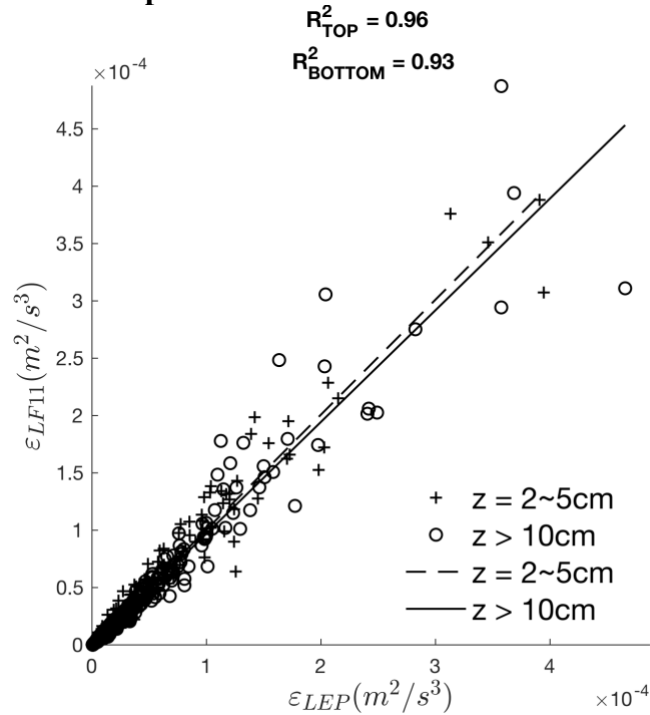


Figure 3.24 Comparison of the LEP method and the LF11 method

In sum, the Direct method, Spectrum method, Structure-function method and Large Eddy PIV method were compared in this section. The anisotropy between the vertical direction and the

horizontal direction is observed in the comparisons, the anisotropy increased as the elevation decreased, and the anisotropy brings more noise when applying the LF33 method. From the velocity spectrum curve which is directly related to the resolution of the PIV, we found that the velocity spectrum is in the range near the end of the IR, where might not following the $-5/3$ slope very well, thus the methods with the assumption of in the IR might not suit for the flow condition in this thesis.

Therefore, the direct method is selected in the thesis since the direct method is relatively robust and with fewer assumptions. And the LEP method was deprecated because it is too dissipate when estimating the flow with low Re number.

3.5 Results and correlation analysis of turbulent diffusivity

The direct method and the k-epsilon method were selected for the turbulent diffusivity/viscosity estimation. The eddy viscosity estimated by the k-epsilon method is denoted as ν_T while the diffusivity by the direct method is D_z .

3.5.1 Time series result and data selection

By applying all the methods selection to all datasets, the vertical profile of the turbulent parameters could be calculated from the velocity maps and the particle concentration extracted from the recorded images. By using the 2D median filter in the time series of the profiles, both the spatial and the temporal are smoothed and with outliers removed. The filtered time series result is shown in Figure 3.25. From the time series mean velocity, we found that the deployment during October is very low energetic, but for the July and August, there were several high-velocity events. The particle concentration time series shows there's a decreasing trend of the

particle concentration from July to October. The depletion of the particle concentration was observed from the concentration profiles, the depletion layer is around 10 cm from the bottom. In Figure 3.25 (f), the particle flux is decreased from July to October, which indicated that the grazing rate of the quagga mussel was decreased due to the lack of food source.

For the convenience of evaluating the time series data, we selected 27 periods from the time series results by following the criteria that the turbulent parameters are relatively identical in every period. For every period, the results were averaged for later analysis. The selected periods were attached in APPENDIX.

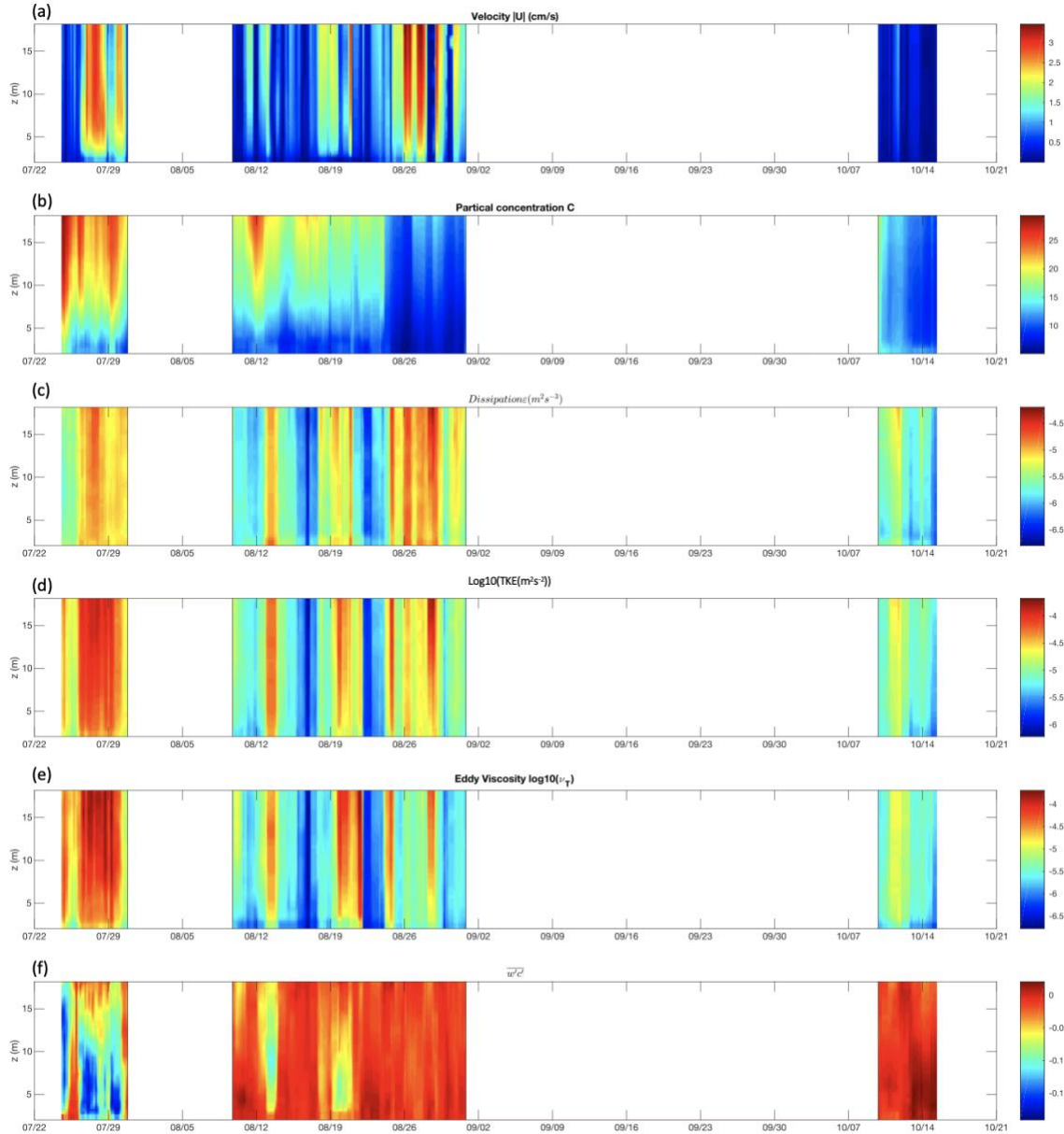


Figure 3.25 Time series of results
(a) Mean horizontal velocity $|U|$, (b) Particle concentration C , (c) Dissipation rate ε , (d) TKE, (e) Eddy viscosity ν_T , (f) Particle flux $w' c'$.

3.5.2 Analysis of the selected data

For the convenience of comparison, we selected the near bottom($z=2\sim 5\text{cm}$) and the top region($z>10\text{cm}$) for the analysis, the results were averaged in the bottom region and the top region. Figure 3.26 is the comparison of the eddy viscosity and turbulent diffusivity, the figure

shows fairly good coupling for the eddy viscosity and turbulent diffusivity, the result corresponded to the Liao's result (Liao et al., 2009) which applied the covariance method in the eddy viscosity method for a case with smooth mean velocity profile.

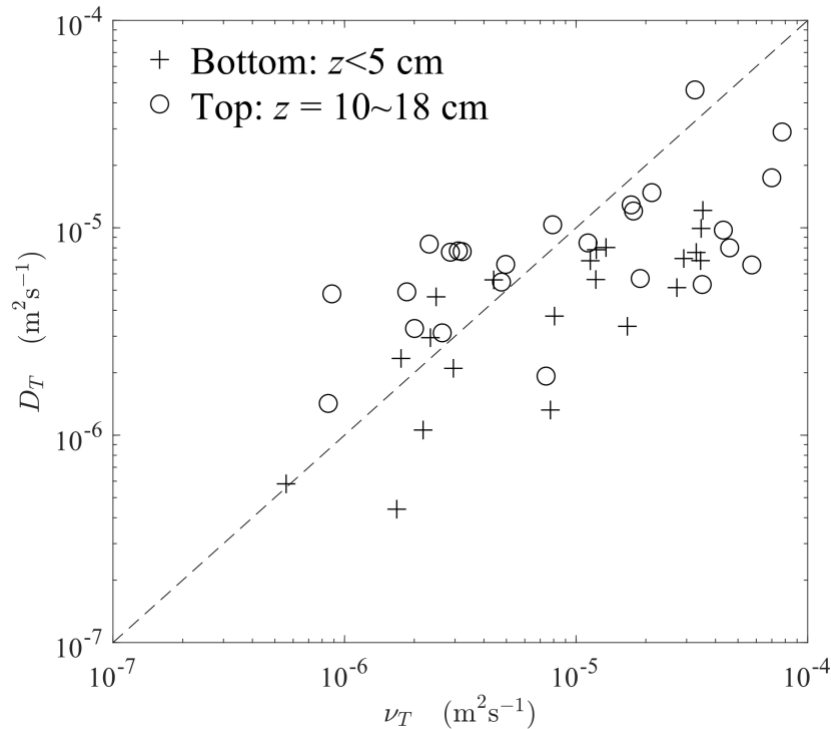


Figure 3.26 Comparison of the turbulent viscosity and turbulent diffusivity

For evaluating the source of the turbulent diffusivity, we plotted the comparison between the mean velocity and diffusivity. Figure 3.27 shows that the mean velocity is not correlated to the diffusivity very well, the uncorrelation between the mean velocity and the diffusivity implied that the major source of the diffusivity is not from the roughness of the lakebed, because the diffusivity should increase as the velocity increased if the bed roughness is the main source of turbulent diffusivity. This result implied that the other source of the turbulent diffusivity, mussel exhalant jet, might contribute to the major part of the turbulent mixing.

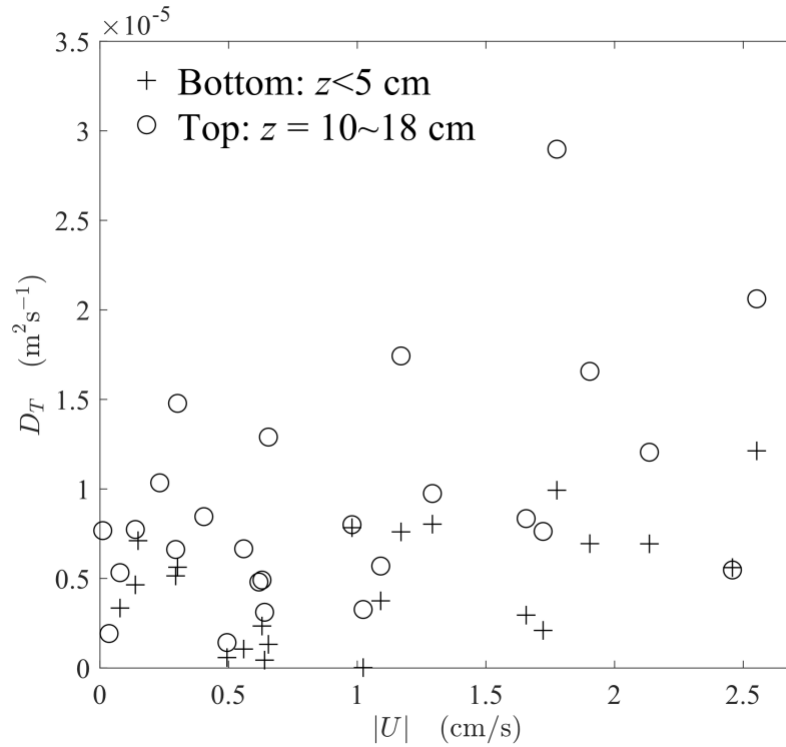


Figure 3.27 Comparison of the mean velocity and the turbulent diffusivity

Figure 3.28 shows the correlation between the particle concentration and the eddy viscosity. The reason we compared the particle concentration with the eddy viscosity instead of the diffusivity is that the diffusivity calculation is calculated from the particle concentration fluctuation. The correlation between particle concentration and the eddy viscosity is relatively good, and there is a trend that the eddy viscosity increased as the particle concentration increased. This result implied that the profundal mussels exhalant jet might be the main source of the near-bed turbulent diffusivity.

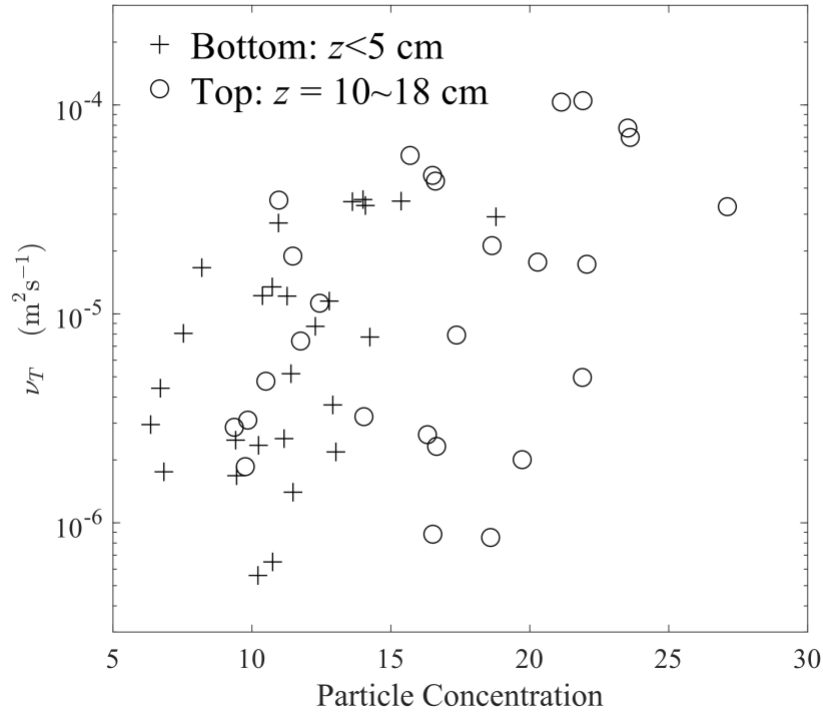


Figure 3.28 Comparison of the particle concentration and the eddy viscosity

3.5.3 Filtration rate of mussels

In this study, it is assumed that near-bed vertical transport of particles through turbulent is primarily a result of mussel filtration. If the collective pumping rate of mussels is denoted as Q ($\text{m}^3 \text{s}^{-1}$ per square meter, or m s^{-1}), and mussels can filter out most if not all particles delivered to the bed,

$$QC_0 = -\overline{w'c'} \quad (3.35)$$

where C_0 is the particle concentration immediately above the mussel bed, and the turbulent flux $-\overline{w'c'}$ is assumed to be nearly uniform in a short distance above the mussel bed. With the data measured and averaged in each of the 27 sections, mussels' pumping rate can be estimated, where C_0 and $-\overline{w'c'}$ are taken as the averages of measured profiles of particle

concentration and turbulent flux over $z = 2\sim 5$ cm. The time sequence of the estimated Q is shown in Figure 3.29, along with the measured near-bed turbulent diffusivity D_T (i.e., average of $z = 2\sim 5$ cm)

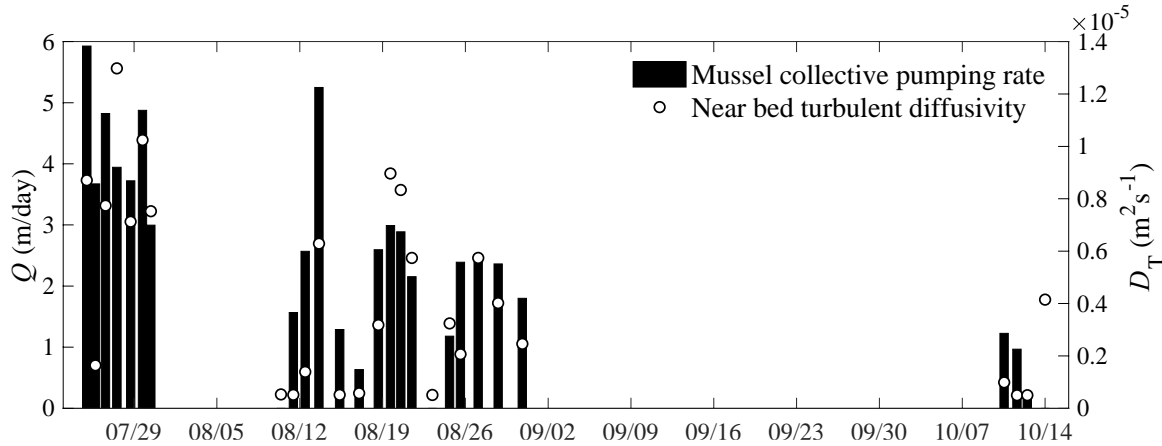


Figure 3.29 Time series of estimate mussel collective pumping rate (converted to m/day) and near-bed diffusivity

It appeared that mussels' pumping rate, thus the filtration activity was relatively high in July and earlier August of 2018. It then gradually decreased. This showed a trend similar to that of the particle concentration and the near-bed diffusivity. A good linear correlation was found between the diffusivity and pumping rate, for both $z = 2\sim 5$ cm and $z = 10\sim 18$ cm, as shown in Figure 3.30. Linear regression was applied that suggested

$$D_T = \gamma Q \quad 3.36$$

where $\gamma = 1.74 \times 10^{-6} \left(\frac{m^2 s^{-1}}{m \text{ day}^{-1}} \right)$ and $4.42 \times 10^{-6} \left(\frac{m^2 s^{-1}}{m \text{ day}^{-1}} \right)$ for $z = 2\sim 5$ cm and $z = 10\sim 18$ cm, respectively. Similarly, a good correlation was also found between the turbulent viscosity ν_T and the pumping rate Q (see Figure 3.31). These relations suggested that mussels' filtration activity is the primary source of turbulence production in the otherwise very quiescent benthic boundary layer.

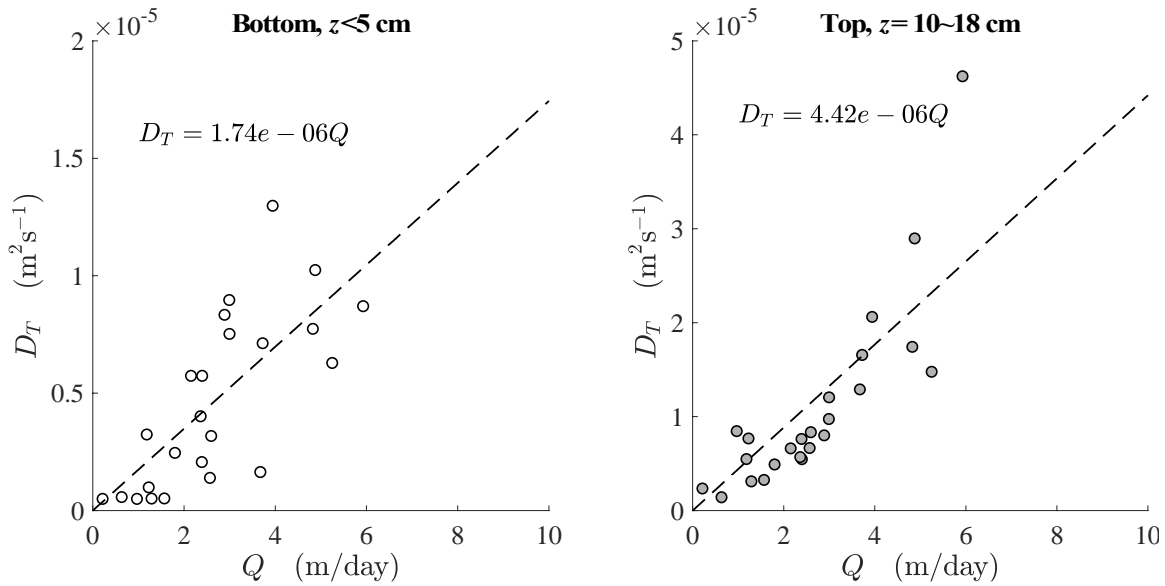


Figure 3.30 Correlation between turbulent diffusivity and mussels' collective pumping rate. Dashed lines and equations in the figure represent linear regression of $D_T = \gamma Q$.

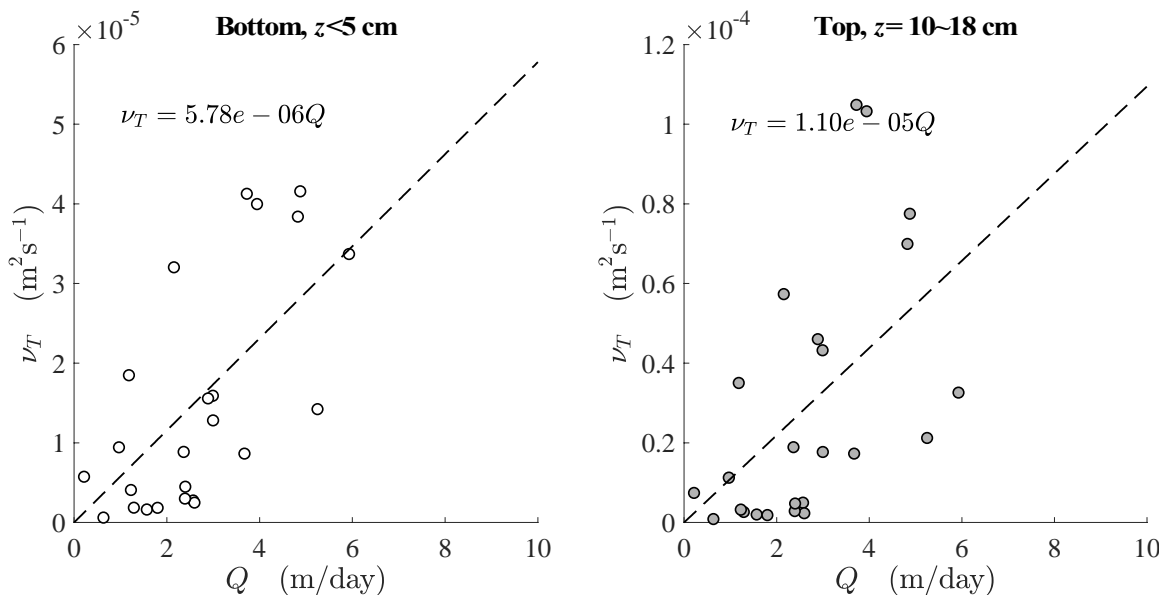


Figure 3.31 Correlation between turbulent viscosity and mussels' collective pumping rate. Dashed lines and equations in the figure represent linear regression of $\nu_T = \gamma Q$.

CHAPTER 4. TESTING HYPOTHESES WITH MODELING ANALYSIS

To test the hypothesis that bio-mixing due to quagga mussels' filtration activities may help them to maximize the grazing rate, a simplified One-D model is developed. Turbulence structures and “eddy” (turbulent) diffusivities measured and analyzed in Chapter 3 will be applied to parameterize the model, which can be solved numerically. The numerical model and empirical mixing coefficients will also be applied to evaluate the excretion of soluble reactive phosphorus (SRP), according to the measured near-bed SRP profiles at the 55m site in Lake Michigan.

4.1 One D advection-diffusion model for phytoplankton transport

Vertical transport of phytoplankton at the profundal site of Lake Michigan can be simplified through a steady-state one-dimensional advection-diffusion process. Since the primary objective of this study is to assess the effects of bio-mixing on transport, algae production, mortality and grazing are not included in the modeled water column. Source and/or sink terms will only be considered at boundaries. In addition, horizontal transport terms are ignored considering the main gradient occurs along the vertical direction only. With these assumptions, the governing equation can be written as

$$\frac{\partial}{\partial z} \left(-D \frac{\partial C}{\partial z} - w_s C \right) = 0 \quad (4.1)$$

where C is the concentration of phytoplankton; z is the vertical coordinate, and $z = 0$ on the lake bottom; D is the vertical diffusion coefficient (e.g., the turbulent diffusivity); and w_s is the magnitude of settling speed of phytoplankton particles (i.e., $w_s > 0$). The simple One-D model is a statement that local advective transport of phytoplankton due to passive settling is balanced by the diffusion process due to turbulent mixing.

4.2 Analytical framework with constant diffusivity

If the diffusivity D is assumed to be constant, the transport equation can be simplified as the following, which is a linear differential equation that could be solved analytically.

$$D \frac{\partial^2 C}{\partial z^2} + w_s \frac{\partial C}{\partial z} = 0 \quad (4.2)$$

The solution of the equation above can only be made with appropriate assumptions for boundary conditions, particularly at the lake bottom where quagga mussels' filter-feeding activities may affect transport of phytoplankton over the entire water column.

4.2.1 Boundary conditions considering mussels' grazing

For the bottom boundary, the diffusive flux plus settling $-D \frac{\partial C}{\partial z} - w_s C$ is assumed to be in balance with mussels' grazing rate. By assuming the filtering rate to 100%, the mussel grazing rate (G) can be calculated as

$$G = dqC_B = QC_B \quad (4.3)$$

where d is the density of the mussels in (1/m²), q is the pump rate of an individual mussel which can be typically represented in (Liter/day), C_B is the phytoplankton concentration on the lake bottom, i.e., $C_B = C(z = 0)$. The formula suggests that the mussels only acquire the particles in a thin layer near the mussel inhalant siphon, the mussel grazing rate is only related to the bottom concentration and its pumping rate. It is more convenient to define the collective filtration rate $Q \equiv dq$, which has a dimension of volume of water filtered per unit time and per unit area of the lake bottom. Therefore, the unit of Q is equivalent to that of a speed in terms of (m/day). In the following analysis, the ratio between the collective filtration rate (Q) and the settling speed (w_s) will frequently be used as an important parameter.

Another important factor is related to phytoplankton particles that are not grazed by mussels and “settled out” of the water column. Although those particles settled on the bottom might be resuspended due to hydrodynamic forces, they are not considered in this study since we focus on profundal mussels particularly in a quiet and stratified environment where mixing from ambient current is very weak. Therefore particles “settled out” will stay on the lake bottom. Here the area of “lake bottom” should exclude areas of opening incurrent siphons of mussels (see Figure 4.1). A “porosity” (β) can be defined as the total area of open siphon cross-sections over a unit lake bottom area, i.e.,

$$\beta \equiv \frac{dA_s}{A_{unit}} \quad (4.4)$$

With an estimated incurrent siphon diameter of about 2~4 mm, and a typical mussel density of $d = 2,000 \sim 10,000 \text{ m}^{-2}$, The porosity β could vary between about 1% to 13%. The relative area of the lake bottom that accepts settling of phytoplankton particles is then defined as

$$\alpha = 1 - \beta \quad (4.5)$$

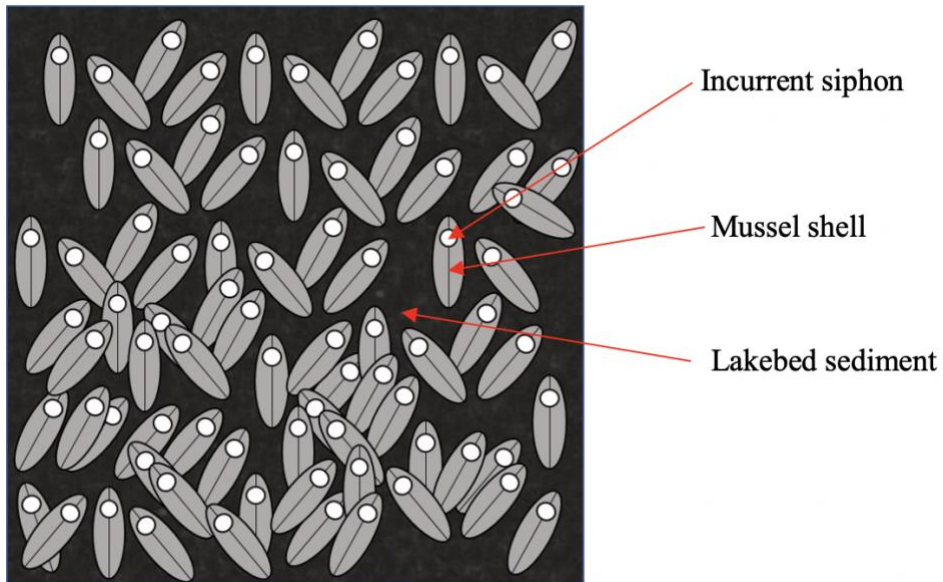


Figure 4.1 Illustration of mussel “porosity” β , which represents the fraction of total areas of mussels’ incurrent siphons per unit area of the lake bottom. Parameter $\alpha \equiv 1 - \beta$ thus represents the fraction of areas including the lakebed sediment and mussel shells (minus incurrent siphons).

With all considerations and assumptions, the bottom boundary condition can be formulated as

$$D \frac{\partial C}{\partial z} + \beta w_s C = QC \quad \text{at } z = 0 \quad (4.6)$$

The top boundary can be considered at a height that is sufficiently far away from the lake bottom such that mussels’ filtration has negligible impact, and concentration gradient vanished.

This condition can be written as

$$\frac{dD}{dz} = 0 \quad \text{at } z = \infty \quad (4.7)$$

4.2.2 Analytical solution with constant diffusivity and finite water depth

To solve the transport equation, there must be at least one Dirichlet boundary condition. Without loss of the generality, the bottom concentration C_B can be considered as the reference value. Therefore, the analytical solution is

$$C(z) = \left[\frac{Q + \alpha w_s}{w_s} + \left(1 - \frac{Q + \alpha w_s}{w_s} \right) e^{-\frac{w_s z}{D}} \right] C_B \quad (4.8)$$

This solution suggests that at the infinite distance (height), $C_\infty \equiv C(\infty) = \frac{(Q + \alpha w_s) C_B}{w_s}$, which means the grazing rate at the bottom equals to the delivery of particle from infinity distance through settling multiplied by the siphon porosity, i.e.,

$$w_s C_\infty = QC_B + \alpha w_s C_B \quad (4.9)$$

If the delivery from the infinite distance is fixed, mussels' grazing rate is a constant value disregarding the pumping rate Q and the diffusivity D . A greater pumping rate will just result in a reduced bottom concentration C_B .

However, it should be noted that this solution is certainly not practical. Water depth (H) is a finite value, and it is more reasonable to assume a known concentration at the water surface, i.e., $C_H \equiv C(z = H)$. It is more practical that the solution is scaled with C_H , and the bottom concentration C_B is not known *a priori*. From the solution (4.8) we know that

$$C_H = C(H) = \left[\frac{Q + \alpha w_s}{w_s} + \left(1 - \frac{Q + \alpha w_s}{w_s} \right) e^{-\frac{w_s H}{D}} \right] C_B \quad (4.10)$$

Therefore, the solution can be given more appropriately as

$$\frac{C(z)}{C_H} = \frac{\frac{Q + \alpha w_s}{w_s} + \left(1 - \frac{Q + \alpha w_s}{w_s} \right) e^{-\frac{w_s z}{D}}}{\frac{Q + \alpha w_s}{w_s} + \left(1 - \frac{Q + \alpha w_s}{w_s} \right) e^{-\frac{w_s H}{D}}} \quad (4.11)$$

Thus, the ratio of the bottom boundary concentration and the surface concentration is

$$\frac{C_B}{C_H} = \frac{1}{\frac{Q + \alpha w_s}{w_s} + \left(1 - \frac{Q + \alpha w_s}{w_s} \right) e^{-\frac{w_s H}{D}}} \quad (4.12)$$

To demonstrate the analytical solution, parameters are specified according to the typical hydrodynamic conditions at the 55-m site, particularly under the summer stratified conditions. Since mussels' siphon jets and filtration activities are not significant sources of momentum and energy into the ambient environment, its interaction with the ambient hydrodynamic mixing and its impact on particle grazing and sedimentation were presented with an assumption of the 1-meter water column. Phytoplankton's passive settling rate was selected to be $w_s = 0.6$ (m day⁻¹) based on (Luo et al., 2012; Shen et al., 2018). Ambient turbulent diffusivity seldom exceeds 10⁻⁵ (m² s⁻¹), thus it is specified to be varying between $D = 1.0 \times 10^{-6}$ and 1.0×10^{-5} (m² s⁻¹). Mussels' collective pumping rate was assumed to vary such that $Q/w_s = 0.01 \sim 50$. Under these

conditions, the normalized phytoplankton concentration profiles $C(z)/C_H$, i.e., equation (4.11) is shown in Figure 4.2

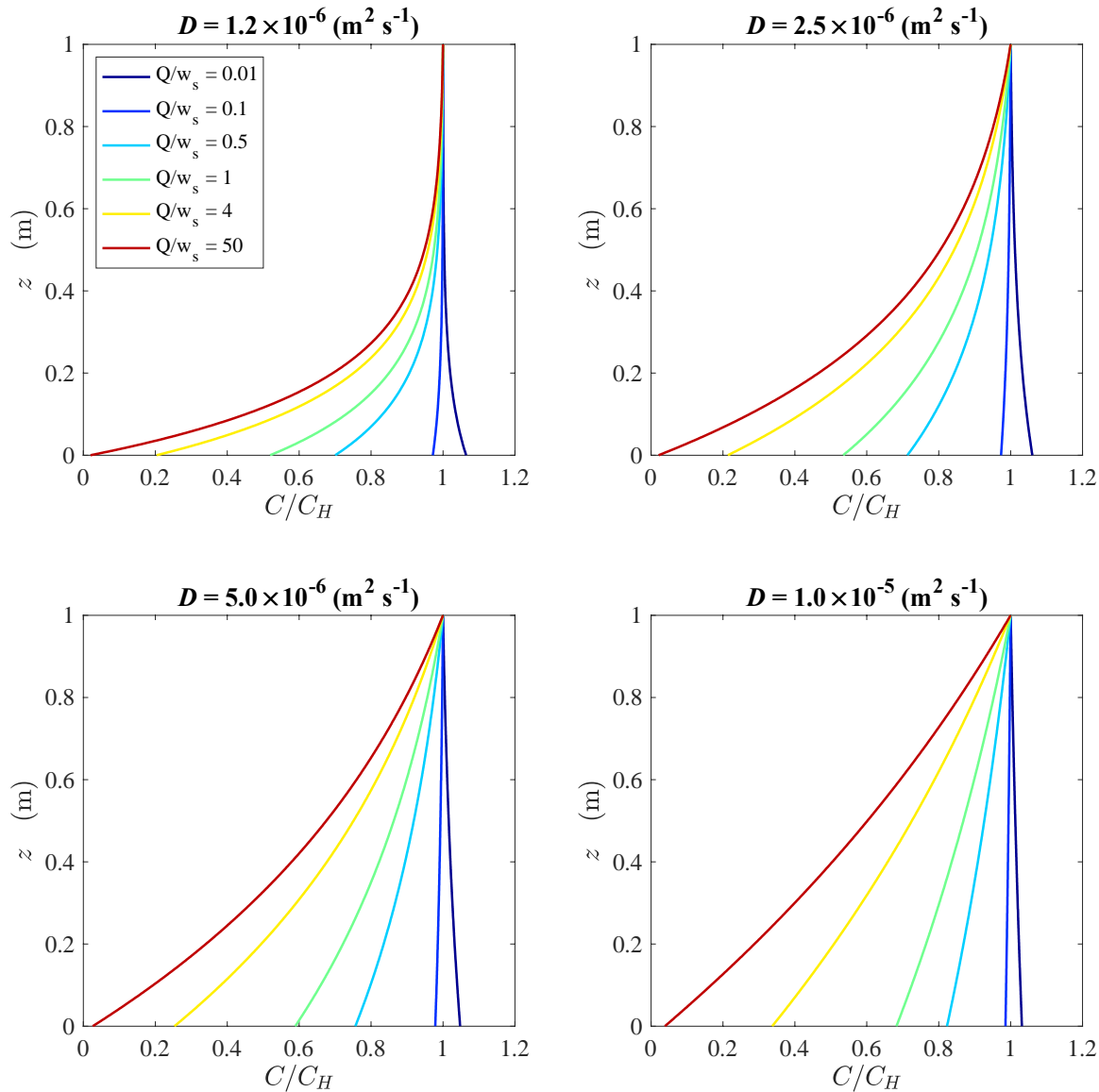


Figure 4.2 Analytical solution of phytoplankton concentration profiles in a 1-meter water column under varying ambient mixing coefficient D and mussels' collective pumping rate Q .

Analytical solutions showed that concentration above mussels decreases as their pumping rate increases, creating a “particle-depleted” boundary layer. The ambient turbulent diffusivity affects the overall shapes of concentration profiles significantly. It was also noted that when $D < 1.2 \times 10^{-6} \text{ (m}^2\text{s}^{-1}\text{)}$, impacts of mussels' filtration are limited within the 1-meter water column

with Q/w_s up to 50, since the concentration gradient at $z = 1.0$ m keeps zero, which suggests a zero-diffusive transport from the top, thus all particles feeding into this system is only supplied by passive settling, i.e., $w_s C_H$. With a higher D , it is apparent that a positive gradient starts to form at $z = 1.0$ m, which means that mussels' filtration starts to affect the entire 1-meter depth so mussels' grazing will be fueled with additional diffusive transport from the top.

To further illustrate this concept, mussels' grazing efficiency can be defined as $G/w_s C_H$, i.e., the ratio of grazing to the passive settling supplied at the top of the water column. Following equation (4.12),

$$\frac{G}{w_s C_H} = \frac{Q C_B}{w_s C_H} = \frac{1}{\left(1 - \frac{\alpha w_s}{Q}\right) - \left[1 - (1 - \alpha) \frac{w_s}{Q}\right] e^{-\frac{w_s H}{D}}} \quad (4.13)$$

This relation between the grazing efficiency and pumping rate Q/w_s at varying background diffusivity are shown in Figure 4.3. In this figure, the dashed line was defined as the “theoretical limit”, which assumes an unlimited water column height. Therefore, the grazing efficiency is independent of turbulent diffusion, and all grazed and settled out particles were completely supplied by passive settling at the infinite distance, i.e., $w_s C_\infty$. According to equation (4.9), the grazing efficiency under the “theoretical limit” is

$$\frac{G}{w_s C_\infty} = \frac{Q C_B}{w_s C_\infty} = \frac{Q}{Q + \alpha w_s} \quad (4.14)$$

With diffusivity less than 1.2×10^{-6} ($m^2 s^{-1}$), the calculated grazing efficiency (red solid line in Figure 4.3) matches that of the “theoretical limit”, which means mussels' grazing effects are limited within a 1-meter height. With the diffusivity increase, the efficiency exceeds that of the “limits”. This suggests that grazing effects extend beyond 1 meter, which increases the effective “settling” of phytoplankton particles by creating a positive gradient of concentration that enhances diffusive transport.

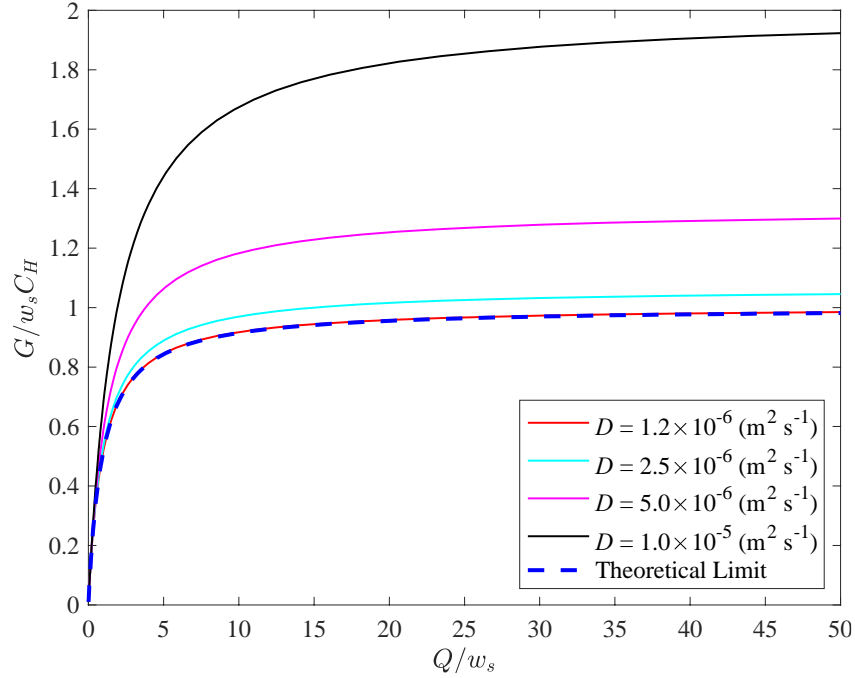


Figure 4.3 Mussels’ grazing efficiency as a function of pumping rate and background turbulent diffusivity. Here the efficiency was defined as the ration of grazing rate QC_B to the passive settling $w_s C_H$.

Moreover, grazing efficiency initially increases rapidly as the pumping rate starts to increase from zero. The rate of increase then reduces and the grazing efficiency seems to approach a “plateau”. Considering the case of infinite water depth and constant concentration C_∞ , the grazing efficiency will asymptote to 100% as Q approaching infinity (see equation 4.14). It is reasonable to consider that mussels are not willing to pursue a 100% efficiency as the energy spent on increasing the pumping rate has little increase of grazing efficiency in return. It is, however, possible to achieve fairly high efficiency with a modest pumping effort. If we define an “optimal” pumping rate Q_{opt} as that produces a 95% efficiency, then we have $\frac{Q_{opt}}{Q_{opt} + \alpha w_s} = 0.95$, according to equation (4.14). This suggests that $\frac{Q_{opt}}{w_s} = 19\alpha$. For example, if $\alpha = 1 - \beta = 0.93$, and $w_s = 0.6$ (m/day) we have $Q_{opt} = 17.67 w_s = 10.6$ (m/day). For a mussel density $d = 10,000$ (m⁻²), this is equivalent to an optimal pumping rate of about 1.06 liter per day per

individual mussel, on average. The optimal pumping rate is close to 3 liter per day from the empirical measurements of the large profundal mussels (>22mm) in Lake Michigan by (Vanderploeg et al., 2010).

4.3 Enhanced Mussel Grazing due to Bio-Mixing: A Numerical Modeling Test

The analytical solution presented above assumes a constant diffusivity profile, which does not account for near-bed mixing due to mussels' filtration activities. As shown in Chapter 3, field measurements suggested a good correlation between mussels' filtration pumping rate and near-bed turbulent diffusivity. To test the effects of the enhanced diffusivity, particularly on mussels' grazing rate, a numerical model is needed to account for varying and nonuniform distribution of the diffusivity.

A Finite Volume approach is selected for numerical modeling. The water column is discretized into N "cells" with a uniform size Δz . Considering a cell with index i ($i = 0, 1, \dots, N - 1$), with the cell above and below indexed as $i + 1$ and $i - 1$, respectively (Figure 4.4), the discretized equation that approximate the advection-diffusion equation (4.1) is

$$-\frac{D_{i-\frac{1}{2}}}{\Delta z} C_{i-1} - \left(\frac{D_{i+\frac{1}{2}}}{\Delta z} + \frac{D_{i-\frac{1}{2}}}{\Delta z} + w_s \right) C_i + \left(\frac{D_{i+\frac{1}{2}}}{\Delta z} + w_s \right) C_{i+1} = 0 \quad (4.15)$$

where an upwind scheme is applied for the advection due to settling, and the central difference scheme is applied for diffusive transport. The phytoplankton concentration is defined on the center of each cell and the diffusivities are defined on cell faces. Settling speed w_s is assumed as a constant value throughout. As illustrated in Figure 4.4b, the bottom boundary condition is discretized as

$$w_s C_1 + D_1 \frac{(C_1 - C_0)}{\Delta z} = Q C_0 + \alpha w_s C_0 \quad (4.16)$$

i.e., the diffusive transport and settling into the bottom cell are balanced with mussels' filtration and phytoplankton particles that "settled out" on the lake bottom. The top cell of the water column is assumed to maintain a constant concentration. For convenience, it is set as

$$C_{N-1} = 1.0$$

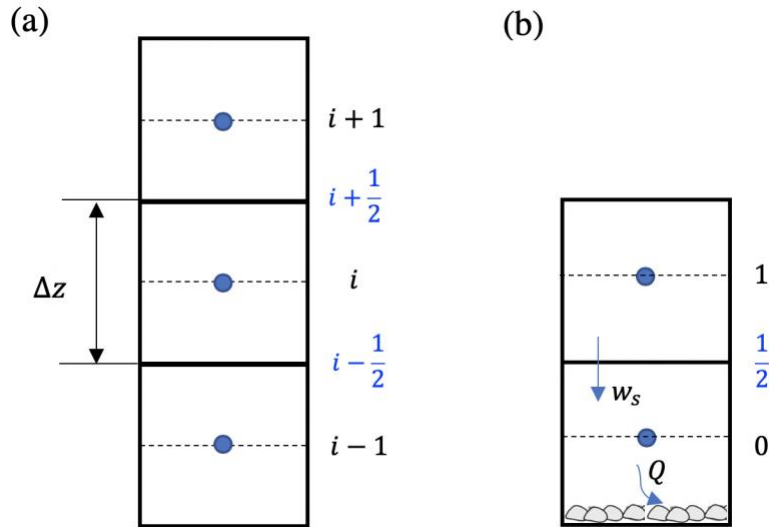


Figure 4.4 Illustration of the one-d FVM grid structure.
(a) interior finite volume cell stencil (b) bottom boundary condition

Modeling runs were conducted to evaluate the mixing and mussels' grazing in a profundal environment in Lake Michigan. To be consistent with the analytical framework, the height of the water column was set to be $H = 1.0$ m, considering the limited impact on momentum or energy from filter-feeding activities. Since it is difficult to precisely describe the vertical distribution of diffusivity, a conceptual structure is specified with three controlling parameters: (1) a background diffusivity D_B which is largely uniform almost over the entire water column; (2) a minimum diffusivity $D_{min} = 1.0 \times 10^{-6}$ m²s⁻¹ (i.e., a nominal value of the molecular viscosity of water); and (3) an enhanced diffusivity due to mussels' bio-mixing, D_{siphon} , which is linearly proportional to mussels' collective pumping rate:

$$D_{siphon} = \gamma Q$$

where the coefficient $\gamma = 1.272 \times 10^{-6} \frac{m^2 s^{-1}}{m \text{ day}^{-1}}$, as derived from field data (see Chapter

3). In addition, if $D_{siphon} < D_B$, it is forced to be equal D_B , i.e., the enhanced diffusion due to bio-mixing is “buried” in the background mixing. With our best knowledge, the vertical distribution of diffusivities was designed into a “four-layer” structure:

1. The linear bottom layer from $z = 0$ to 2 cm : diffusivity increases linearly from D_{min} to D_{siphon} ; This profile considers the fact that turbulent diffusivity usually is suppressed as it approaches to the solid wall.
2. The constant mixing layer from $z = 2$ to 20 cm : diffusivity is uniformly set as D_{siphon} ;
3. From $z = 20 \text{ cm}$ to $z = 30 \text{ cm}$, diffusivity is linearly reduced from D_{siphon} to D_B ;
4. From $z = 30 \text{ cm}$ up to the water column top $z = H$, the diffusivity is uniformly set as the background D_B .

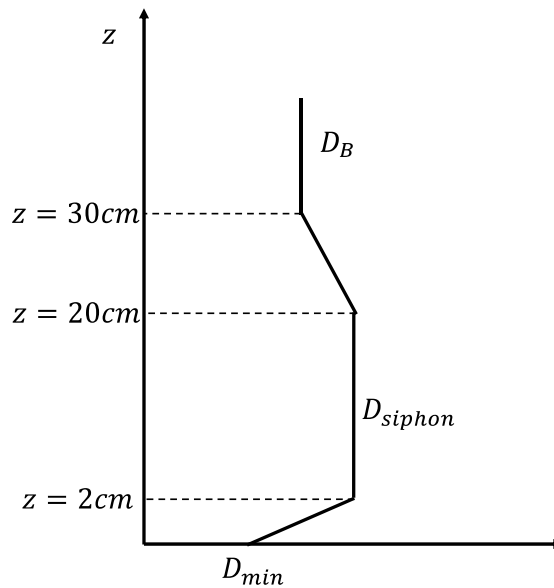
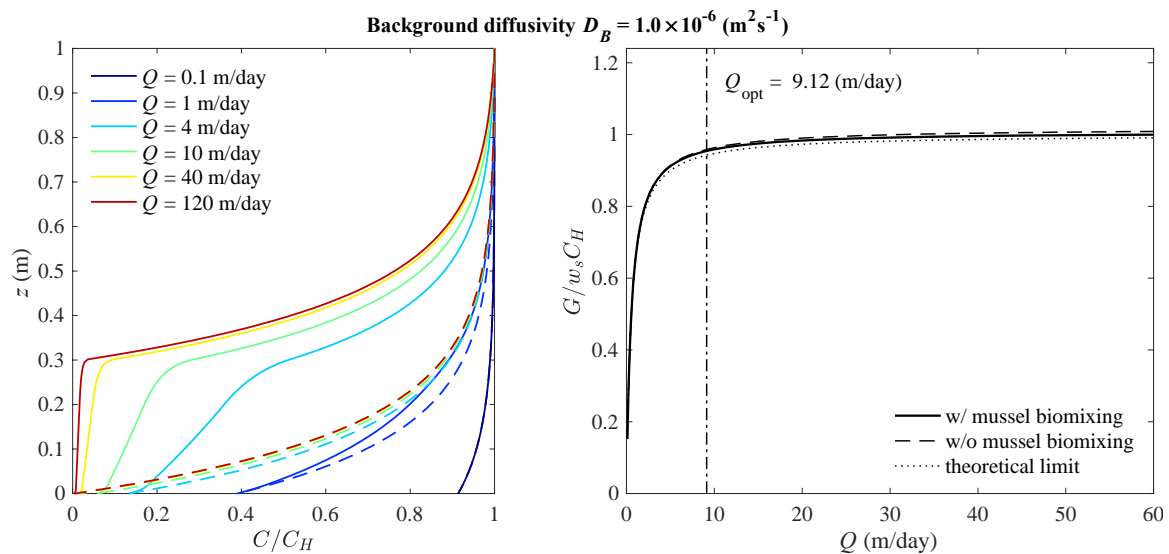
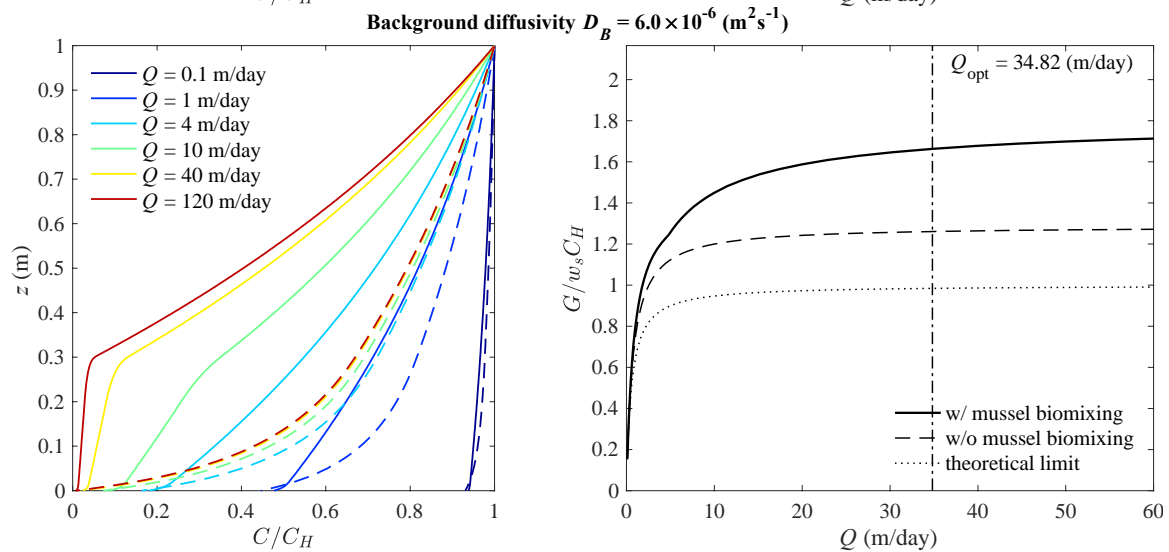
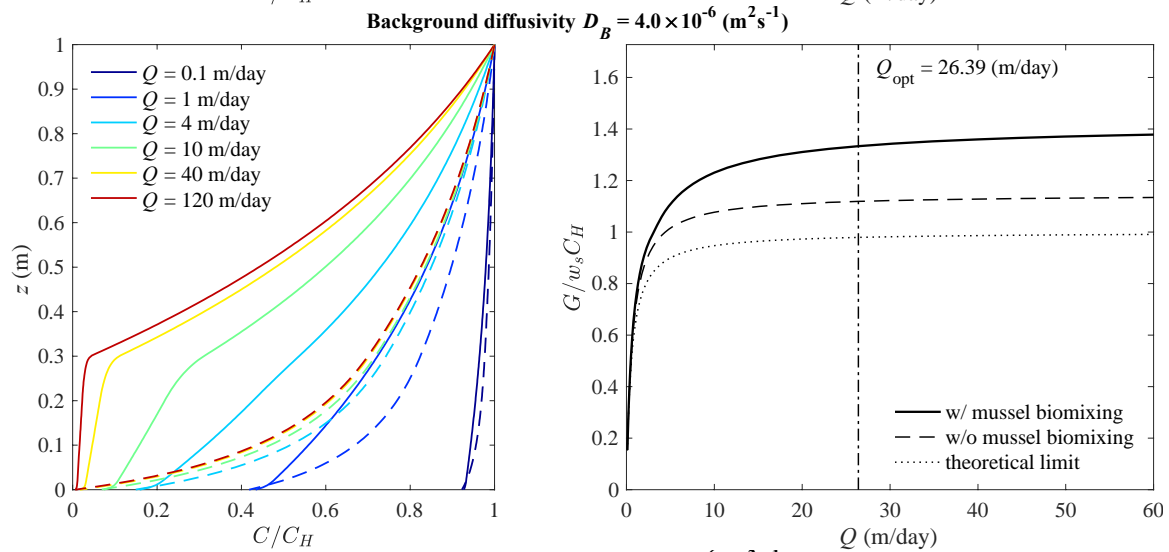
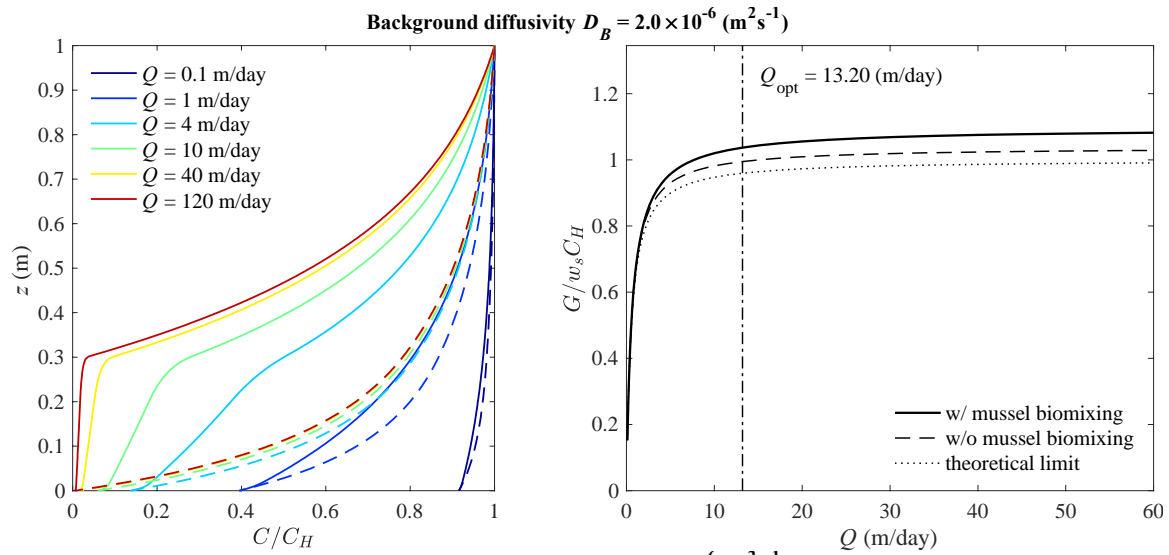


Figure 4.5 Illustration of the “four layers” structure

For comparison, simulation runs were also conducted by ignoring the enhanced diffusivity due to mussels' bio-mixing. Thus, a profile is specified such that diffusivity increases linear from D_{min} to D_B in $z = 0 \sim 30$ cm. It then remains constant D_B for $z > 30$ cm. The two scenarios were denoted as “w/ mussel bio-mixing” and “w/o mussel bio-mixing”, respectively.

Figure 4.6 shows modeling results for normalized phytoplankton concentration profiles $\left(\frac{C}{C_H}\right)$ and the normalized grazing rate $\left(\frac{G}{w_s C_H}\right)$ with varying background diffusivity ($D_B = 10^{-6} \sim 10^{-5} \text{ m}^2 \text{ s}^{-1}$) and collective mussel pumping rate ($Q = 0.1 \sim 120 \text{ m day}^{-1}$), for cases with and without the “bio-mixing” enhanced diffusivity. Within the range of these variabilities, it appears that the additional diffusivity D_{siphon} due to bio-mixing causes a dramatic change to the concentration profile. As D_{siphon} increases with the pumping rate, a 30 cm layer above the bed with uniformly low concentration start to develop, forming a sharp gradient at $z = 30$ cm. This result is not surprising as the model was designed to assign D_{siphon} in the bottom 30 cm. In addition, a greater gradient is formed at $z = 1.0$ m, compared to the case w/o bio-mixing.





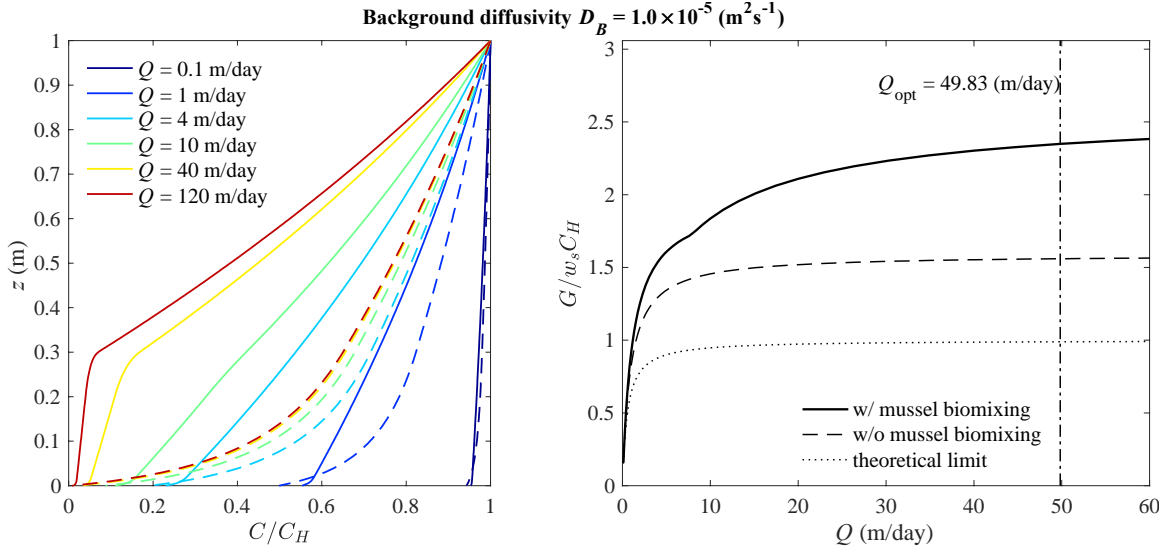


Figure 4.6 Results of numerical simulation for the phytoplankton concentration profile (left) and grazing rate (right) with varying collective pumping rate (Q) and background diffusivity (D_B), with and without bio-mixing effects (i.e., D_{siphon}). Solid and colored lines represent concentration profiles with bio-mixing under different pumping rates. Dashed and colored lines are those without bio-mixing. The difference in Q is represent by different colors.

The normalized grazing rate $\frac{G}{w_s C_H}$ can be considered as a grazing efficiency. Similar to the result of the analytical solution, the grazing efficiency increases with the pumping rate, and the increase “plateaus” as pumping rate becomes excessively large. When the background diffusivity is limited, e.g., $D_B = 1.0 \times 10^{-6}$ ($m^2 s^{-1}$), mussels’ filtration effect seems to be limited within the 1-m water column as the concentration gradient at $z = 1.0$ m is negligible. As a result, grazing efficiency curves, with or without biomixing D_{siphon} , are almost identical to that predicted by the “theoretical limit”, i.e., equation (4.14). As D_B increases, filtration starts to extend beyond 1-m by creating a gradient at $z = 1.0$ m that promotes diffusive transport. Therefore grazing efficiency starts to exceed that predicted by the “theoretical limits” as mussels’ pumping rate grows. Moreover, grazing efficiencies for cases that include bio-mixing effects are greater than those without bio-mixing effects, and the exceedance increases with the background diffusivity D_B .

To evaluate the effects of filtration rate, the optimal pumping rate Q_{opt} is defined, so the corresponding grazing efficiency reaches 95% of the asymptotic maximum according to simulation results. This analysis follows the same argument in the analytical modeling framework, i.e., it is not economical for mussels to pursue a 100% grazing efficiency considering their energy cost. The optimal pumping rate at different background diffusivity, the corresponding grazing efficiency with and without bio-mixing diffusivity are presented in Table 4.1.

Table 4.1 Optimal mussel pumping rate under different background diffusivity and the corresponding grazing efficiency.

The individual pumping rate $Q_{ind} = Q/d$, is calculated with the assumption of mussel density $d = 10,000 \text{ (m}^{-2}\text{)}$.

Background diffusivity $D_B \text{ (m}^2 \text{ s}^{-1}\text{)}$	Optimal collective pumping rate $Q_{opt} \text{ (m day}^{-1}\text{)}$	Optimal individual pumping rate $Q_{ind} \text{ (L day}^{-1}\text{)}$	Grazing efficiency at Q_{opt} of the theoretical limit	Grazing efficiency at Q_{opt} with bio-mixing effect	Grazing efficiency at Q_{opt} without bio-mixing effect
1.0×10^{-6}	9.12	0.912	0.942	0.954	0.958
2.0×10^{-6}	13.2	1.32	0.960	1.037	0.995
4.0×10^{-6}	26.4	2.64	0.979	1.334	1.112
6.0×10^{-6}	34.8	3.48	0.984	1.663	1.261
8.0×10^{-6}	44.6	4.46	0.987	2.011	1.411
1.0×10^{-5}	49.8	4.98	0.989	2.349	1.560

Modeling results suggest that bio-mixing due to mussels' filter-feeding can improve the grazing efficiency significantly, particularly with a certain background mixing effect. For example, when $D_B = 1.0 \times 10^{-5} \text{ (m}^2 \text{ s}^{-1}\text{)}$, mussels' grazing efficiency with the enhanced diffusivity at an optimal pumping rate of 49.8 (m day⁻¹) is about 50% higher than that without bio-mixing.

It should be noted that modeling analysis here arbitrarily selected a water column of $H = 1.0$ m, and assigned a constant concentration as the boundary condition at the top of the water column. This is certainly unnatural. A grazing efficiency greater than that predicted by the “theoretical limit” implies an additional source of phytoplankton is fed into the water column from above, due to a non-zero gradient at the top. Realistically, a grazing efficiency exceeding the settling limit can be more appropriately interpreted as an extended impact (e.g., beyond the specified height H) through additional diffusive transport which results in a greater “effective settling” than the “passive settling” (Mosley and Bootsma, 2015; Shen et al., 2018).

4.4 Soluble reactive phosphorus flux estimation

The numerical modeling framework presented in 4.3 was also applied to estimate the excretion rate of soluble reactive phosphorus (SRP) from mussels. Specifically, we consider a simple one-d diffusion process for SRP in a short water column immediately above the mussel bed without additional source or sink:

$$D \frac{dC_{DP}}{dz} = F_{DP} \quad (4.17)$$

where $C_{DP}(z)$ is the concentration of SRP, $D(z)$ is the turbulent diffusivity of SRP which is considered as the same diffusivity for phytoplankton, and F_{DP} is the flux of SRP from mussels' excretion. The equation can be simply solved by integration for $z = 0$ to any given height, i.e.,

$$C_{DP}(z) = C_{DP0} - F_{DP} \int_0^z \frac{1}{D(z')} dz' \quad (4.18)$$

where $C_{DP0} = C_{DP}(z = 0)$. To estimate the flux of SRP, the solution is applied to “match” measured SRP profiles with the least-square fit.

Eight SRP profiles measured from the microprofilers were selected for this analysis (see Figure 4.7). Among them, only four datasets have both PIV and SRP available, i.e., data acquired on 31-July-2018, 16-August-2018 and 23-September-2018 (two profiles). For these datasets with PIV results, the profile of diffusivity is defined following the same approach in section 4.3. Specifically, diffusivity increases linearly from a background (D_B) to D_{siphon} from $z = 0$ to 2 cm, then it remained as a constant D_{siphon} for $z = 2$ to 30 cm. The near-bed diffusivity due to bio-mixing D_{siphon} is set as the depth-average diffusivity from PIV analysis. A non-linear regression procedure was followed to estimate the two unknown parameters C_{DP0} and F_{DP} by matching the model solution (4.18) with the measured profile with the least square sense. For the other four datasets without PIV data, the least square regression was still conducted with three unknowns: C_{DP0} , F_{DP} and D_{siphon} . The same structure of diffusivity profiles was assumed except that there D_{siphon} is estimated as part of the regression instead of from that measured.

Measured SRP profiles and results of regression analysis are shown in Figure 4.7 and Figure 4.8. Estimated SPR flux and other modeling parameters for this analysis are presented in table Table 4.2.

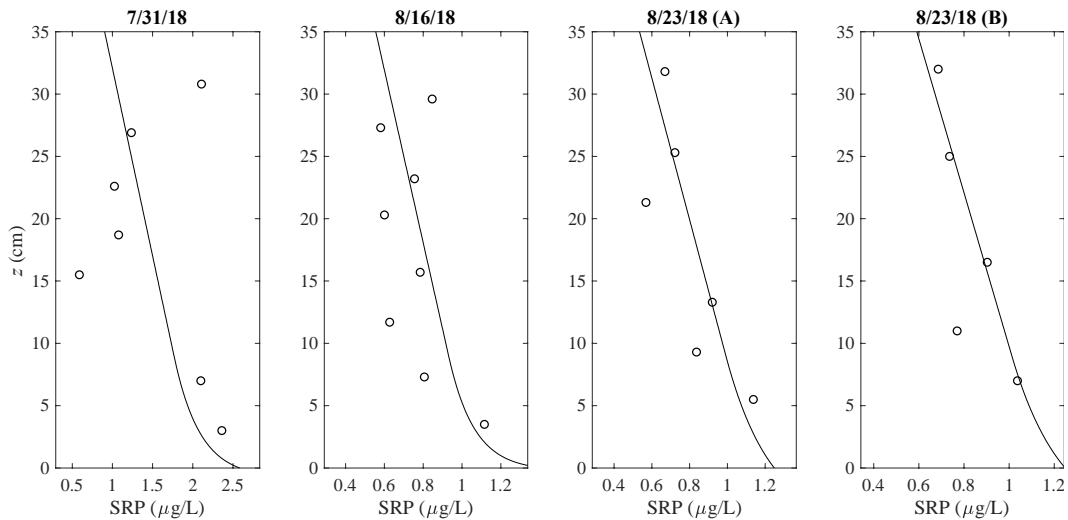


Figure 4.7 Profiles of SRP from microprofiler measurement (circles) and from model solution (solid line), with the SRP flux F_{DP} and bottom concentration C_{DP0} estimated with nonlinear fitting. Distribution of diffusivity $D(z)$ is modeled with average diffusivity measured by PIV during the same time period of SPR microprofiling measurements.

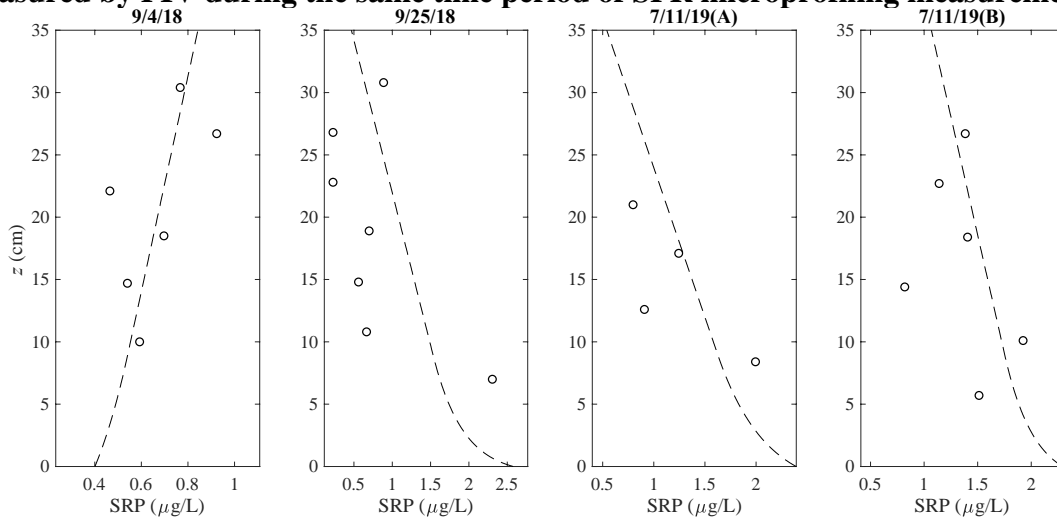


Figure 4.8 Profiles of SRP from microprofiler measurement (circles) and from model solution (solid line), with the SRP flux F_{DP} , bottom concentration C_{DP0} and the diffusivity $D(z)$ all estimated with nonlinear fitting, since PIV data were not available during the microprofiling measurements.

Table 4.2 SRP flux estimation from PIV and microprofiler measurements. Estimated SRP fluxes on 8/23/19 and 7/11/19 were averaged between two replicate deployed microprofilers.

	7/31/18	8/16/18	8/23/18	9/4/18	9/25/18	7/11/19
$D_{siphon} \times 10^5 (m^2/s)$	1.28	4.53	0.29	0.19	1.46	0.63
$F_{DP} \times 10^3 (\mu g s^{-1} m^{-2})$	42.5	65.4	4.9	-2.2	59.7	20.7
$F_{DP} (\mu mol d^{-1} m^{-2})$	118.6	182.3	13.7	-6.1	166.6	57.7
$Q (m/day)$	2.9	5.4	1.3	N/A	N/A	N/A

Estimated SRP flux, which can be assumed as the excretion from mussels, showed a significant variation between 13.7 and 182.3 μmol per day per square meter, except for the case on 9/4/18 with a negative flux, i.e. net transport from water to the substrate. An mean SRP excretion rate of 63 μmol SRP $\text{m}^{-2} \text{d}^{-1}$ with mussel samples collected at the same 55 m site was reported (Mosley and Bootsma, 2015), which is comparable with the average flux estimated from the eight measurements in this study. For the three measurement cases where PIV data were present, the estimated SRP flux has a good correlation with the estimated mussel collective

pumping rate (see Figure 4.9), which can be considered as a partial validation on the SRP flux estimation.

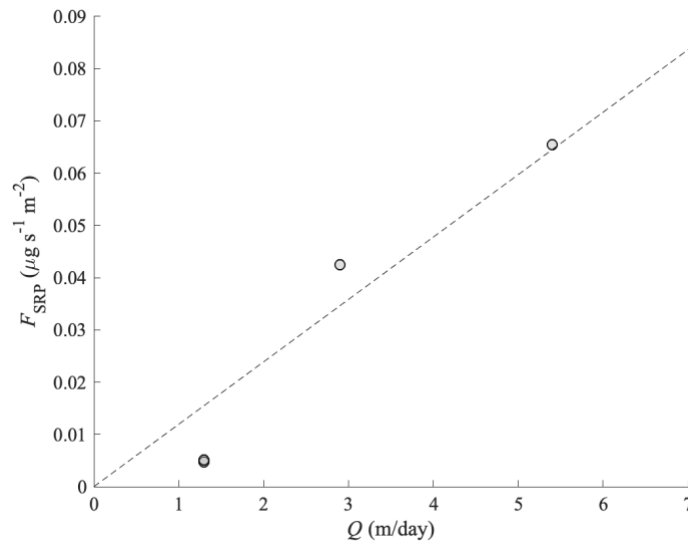


Figure 4.9 Estimated SRP flux vs collected mussel pumping rate according to PIV and microprofiler measurements on 7/31/18, 8/16/18 and 8/23/18.

CHAPTER 5. CONCLUSIONS

In this thesis study, an improved in-situ UW-PIV system had been developed for the bottom turbulence measurements immediately above the quagga mussels bed in a profundal site of Lake Michigan. Through a large number of deployments from summer 2018 to fall 2019, the PIV system has been proved to be reliable and robust for long term deployment (up to three weeks) in a deepwater environment. Moreover, with the powerful Linux-based micro-computer inside, the UW-PIV has high scalability for additional signal collection systems or sensors, which make it potentially a lake bottom monitoring platform for future research.

The velocity map and particle density were extracted from the particle images by the cross-correlation method and particle counting algorithm. PIV measurements were post-processed with a self-adaptive “median test” method to remove spurious vectors due to the low particle density. A velocity spectrum analysis was applied to help to identify cases where mean current flow may generate wake turbulence from the instrument.

The turbulent mixing above the mussel bed was evaluated by estimating the turbulent viscosity and diffusivity. Since the Reynolds number of the boundary layer hydrodynamics was low and turbulence was likely produced by mussels’ filtration activities, a more universal approach, i.e., the TKE-dissipation method ($k - \epsilon$), was selected to evaluate the turbulent viscosity, which does not rely on the Law-of-Wall assumption. Turbulent diffusivity was directly calculated from the measure turbulent flux of particles and the mean particle concentration gradient, following a Fickian diffusive transport concept.

For the analysis of Reynolds stresses, TKE, and turbulent fluxes in the boundary layer of the profundal site, it was found challenging to separate turbulence from low-order transient

various with unknown sources. Structure-function method and low-pass filtering approach were applied to evaluate turbulent fluctuations and their correlations. The two methods were cross-validated in terms of the measured Reynolds stresses and TKE. A good correlation was found while the low-pass filtering produced results with fewer data scatter. The analysis suggested a practical approach to estimate turbulence parameters in such a low energetic environment with 2D PIV measurement, i.e., irrotational random motions can be removed through low-pass filtering, while the smoothing window of the filter can be determined by validation with the structure-function method.

Four methods were tested for the estimation of the TKE dissipation rate, i.e., the “direct” method, velocity spectrum, structure-function and Large Eddy PIV method. Results from different methods correlated well despite varying correlation ratios. The direct method was eventually selected for subsequent analysis since fewer assumptions and no parameter adjusting are required compared to other methods.

Measured turbulent diffusivity from turbulence analysis had a good correlation with the turbulent diffusivity derived from turbulent flux. Such a correlation demonstrated that the analysis presented in this thesis are robust since the two parameters were estimated from two independent approaches. It also proved that the Reynolds analogy between turbulent viscosity and diffusivity may also be valid for the low energetic profundal benthic boundary layer.

Measured turbulent diffusivity/viscosity varied between 10^{-6} to 10^{-5} ($m^2 s^{-1}$), which seemed to correlate with the ambient particle concentration. However, they are not correlated with the ambient mean current flow velocity. Collective pumping rates of mussels were also estimated from measured near-bed turbulent flux of particles. Data showed that near-bed turbulent diffusivity increases linearly with mussels’ pumping rate. These observations supported our

hypothesis that bio-mixing due to mussels' siphon currents is the major source of turbulence the profundal boundary layer, and the enhanced mixing may improve mussels' grazing efficiency.

To further test the hypothesis, a One-D advection-diffusion model with analytical and numerical solutions was applied to examine the relation between mussels' pumping rate and their grazing efficiency. A simple analytical solution suggested that mussels' filter-feeding combined with turbulent mixing can improve grazing efficiency significantly, compared to the scenario of food delivery through passive settling. By assuming 95% of the potential maximum as the optimized grazing efficiency, the optimized pumping rate is about 1 liter per day for a single profundal mussel from the analytical solution.

Numerical modeling was applied to account for the effects of bio-mixing on mussels' grazing. The observed linear relation between turbulent diffusivity and mussels' pumping rate was applied to parameterized the model. Modeling results suggested that the grazing efficiency increases with biomixing. The grazing efficiency also depends on the background diffusivity, and mussels can access phytoplankton at higher positions of the water volume with a greater background diffusivity, therefore increase the grazing efficiency. Simulation results proved the hypothesis that profundal mussel can maximize their grazing efficiency by the enhanced near-bed turbulence through siphon currents. Model simulation also suggested that an optimal collective pumping rate may exist, which varied between about 1 to 5 liters per day per individual, depending on the ambient mixing condition.

The numerical solution also showed a sharp depletion layer of the phytoplankton concentration near the bottom which is caused by siphon-induced mixing. The result might conflict with the understanding that the quagga mussel can benefit from a longer siphon to access the higher level with higher food concentration. Field observation and numerical analysis in this

study showed that the siphon length is much shorter than the thickness of the particle-depleted layer.

The SRP flux was estimated by comparing modeling analysis with measured SRP profiles through the least-square fitting. The SRP flux was assumed as the result of phosphorus excretion from mussels. The analysis showed a significant variation of SRP flux during the deployment period, between 13.7 and 182.3 μmol per day per square meter. An average SRP excretion rate of 63 $\mu\text{mol SRP m}^{-2} \text{ d}^{-1}$ with mussel samples collected at the same 55 m site was reported (Mosley, 2014), which seems to be comparable with the average flux estimated from eight measurements in this study.

BIBLIOGRAPHY

- Achenbach, E., Heinecke, E., 1981. On vortex shedding from smooth and rough cylinders in the range of Reynolds numbers 6×10^3 to 5×10^6 . *J. Fluid Mech.* 109, 239–251.
<https://doi.org/10.1017/S002211208100102X>
- Ackerman, J.D., Loewen, M.R., Hamblin, P.F., 2001. Benthic-Pelagic Coupling over a Zebra Mussel Reef in Western Lake Erie. *Limnol. Oceanogr.* 46, 892–904.
- Adrian, R.J., 2005. Twenty years of particle image velocimetry. *Exp. Fluids* 39, 159–169.
<https://doi.org/10.1007/s00348-005-0991-7>
- Baldwin, B.S., Mayer, M.S., Dayton, J., Pau, N., Mendilla, J., Sullivan, M., Moore, A., Ma, A., Mills, E.L., 2002. Comparative growth and feeding in zebra and quagga mussels (*Dreissena polymorpha* and *Dreissena bugensis*): implications for North American lakes. *Can. J. Fish. Aquat. Sci.* 59, 680–694. <https://doi.org/10.1139/f02-043>
- Bertens, G., van der Voort, D., Bocanegra-Evans, H., van de Water, W., 2015. Large-eddy estimate of the turbulent dissipation rate using PIV. *Exp. Fluids* 56.
<https://doi.org/10.1007/s00348-015-1945-3>
- Bertuccioli, L., Roth, G.I., Katz, J., Osborn, T.R., 1999a. A Submersible Particle Image Velocimetry System for Turbulence Measurements in the Bottom Boundary Layer. *J. Atmospheric Ocean. Technol.* 16, 1635–1646. [https://doi.org/10.1175/1520-0426\(1999\)016<1635:ASPIVS>2.0.CO;2](https://doi.org/10.1175/1520-0426(1999)016<1635:ASPIVS>2.0.CO;2)
- Bertuccioli, L., Roth, G.I., Katz, J., Osborn, T.R., 1999b. A Submersible Particle Image Velocimetry System for Turbulence Measurements in the Bottom Boundary Layer. *J. Atmospheric Ocean. Technol.* 16, 1635–1646. [https://doi.org/10.1175/1520-0426\(1999\)016<1635:ASPIVS>2.0.CO;2](https://doi.org/10.1175/1520-0426(1999)016<1635:ASPIVS>2.0.CO;2)
- Bootsma, H.A., Rowe, M.D., Brooks, C.N., Vanderploeg, H.A., 2015. Commentary: The need for model development related to *Cladophora* and nutrient management in Lake Michigan. *J. Gt. Lakes Res.* 41, 7–15. <https://doi.org/10.1016/j.jglr.2015.03.023>
- Bravo, H.R., Bootsma, H., Khazaei, B., 2019. Fate of phosphorus from a point source in the Lake Michigan nearshore zone. *J. Gt. Lakes Res.*
<https://doi.org/10.1016/j.jglr.2019.09.007>
- Ciutat, A., Widdows, J., Pope, N.D., 2007. Effect of *Cerastoderma edule* density on near-bed hydrodynamics and stability of cohesive muddy sediments. *J. Exp. Mar. Biol. Ecol.* 346, 114–126. <https://doi.org/10.1016/j.jembe.2007.03.005>
- Cowen, E.A., Monismith, S.G., Cowen, E.A., Monismith, S.G., 1997. A hybrid digital particle tracking velocimetry technique. *Exp. Fluids* 22, 199–211.
<https://doi.org/10.1007/s003480050038>
- Cuhel, R.L., Aguilar, C., 2013. Ecosystem transformations of the Laurentian Great Lake Michigan by nonindigenous biological invaders. *Annu. Rev. Mar. Sci.* 5, 289–320.
<https://doi.org/10.1146/annurev-marine-120710-100952>
- Doron, P., Bertuccioli, L., Katz, J., Osborn, T.R., 2001. Turbulence Characteristics and Dissipation Estimates in the Coastal Ocean Bottom Boundary Layer from PIV Data. *J. Phys. Oceanogr.* 31, 2108–2134. [https://doi.org/10.1175/1520-0485\(2001\)031<2108:TCADEI>2.0.CO;2](https://doi.org/10.1175/1520-0485(2001)031<2108:TCADEI>2.0.CO;2)

- Fahnenstiel, G., Nalepa, T., Pothoven, S., Carrick, H., Scavia, D., 2010a. Lake Michigan lower food web: Long-term observations and Dreissena impact. *J. Gt. Lakes Res.*, The Lower Food Web of Lake Michigan: Long-term Trends and the Dreissenid Impact 36, 1–4. <https://doi.org/10.1016/j.jglr.2010.05.009>
- Fahnenstiel, G., Pothoven, S., Vanderploeg, H., Klarer, D., Nalepa, T., Scavia, D., 2010b. Recent changes in primary production and phytoplankton in the offshore region of southeastern Lake Michigan. *J. Gt. Lakes Res.*, The Lower Food Web of Lake Michigan: Long-term Trends and the Dreissenid Impact 36, 20–29. <https://doi.org/10.1016/j.jglr.2010.03.009>
- Fanslow, D.L., Nalepa, T.F., Lang, G.A., 1995. Filtration Rates of the Zebra Mussel (*Dreissena polymorpha*) on Natural Seston from Saginaw Bay, Lake Huron. *J. Gt. Lakes Res.* 21, 489–500. [https://doi.org/10.1016/S0380-1330\(95\)71061-9](https://doi.org/10.1016/S0380-1330(95)71061-9)
- Folkard, A.M., Gascoigne, J.C., 2009. Hydrodynamics of discontinuous mussel beds: Laboratory flume simulations. *J. Sea Res.* 62, 250–257. <https://doi.org/10.1016/j.seares.2009.06.001>
- Glassner-Shwayder, K., Myers, B., n.d. Small Mussels with Big Effects: Invasive Quagga Mussels Eat Away at Great Lakes Food Web [WWW Document]. Small Mussels Big Eff. Invasive Quagga Mussels Eat Away Gt. Lakes Food Web. URL <https://research.noaa.gov/article/ArtMID/587/ArticleID/1149/Small-Mussels-with-Big-Effects-Invasive-Quagga-Mussels-Eat-Away-at-Great-Lakes-Food-Web> (accessed 11.15.19).
- Hecky, R.E., Smith, R.E., Barton, D.R., Guildford, S.J., Taylor, W.D., Charlton, M.N., Howell, T., 2004. The nearshore phosphorus shunt: a consequence of ecosystem engineering by dreissenids in the Laurentian Great Lakes. *Can. J. Fish. Aquat. Sci.* 61, 1285–1293. <https://doi.org/10.1139/f04-065>
- Hussain, G., Rees, G.J., 1995. Thermal Decomposition of HMX and Mixtures. *Propellants Explos. Pyrotech.* 20, 74–78. <https://doi.org/10.1002/prop.19950200206>
- J. O Hinze, 1987. *Turbulence*, 2d ed.. ed. New York : McGraw-Hill.
- Jones, H.F.E., Pilditch, C.A., Bryan, K.R., Hamilton, D.P., 2011. Effects of infaunal bivalve density and flow speed on clearance rates and near-bed hydrodynamics. *J. Exp. Mar. Biol. Ecol.* 401, 20–28. <https://doi.org/10.1016/j.jembe.2011.03.006>
- Karatayev, A.Y., Burlakova, L.E., Padilla, D.K., 2015. Zebra versus quagga mussels: a review of their spread, population dynamics, and ecosystem impacts. *Hydrobiologia* 746, 97–112. <https://doi.org/10.1007/s10750-014-1901-x>
- Karatayev, A.Y., Karatayev, V.A., Burlakova, L.E., Rowe, M.D., Mehler, K., Clapsadl, M.D., 2018. Food depletion regulates the demography of invasive dreissenid mussels in a stratified lake: *Dreissena demography in stratified lakes*. *Limnol. Oceanogr.* 63, 2065–2079. <https://doi.org/10.1002/lno.10924>
- Katija, K., Dabiri, J.O., 2009. A viscosity-enhanced mechanism for biogenic ocean mixing. *Nature* 460, 624.
- Katija, K., Dabiri, J.O., 2008. In situ field measurements of aquatic animal-fluid interactions using a Self-Contained Underwater Velocimetry Apparatus (SCUVA): In situ field measurements using SCUVA. *Limnol. Oceanogr. Methods* 6, 162–171. <https://doi.org/10.4319/lom.2008.6.162>
- Katija, K., Sherman, A., Graves, D., Klimov, D., Kecy, C., Robison, B., 2015. DeepPIV: Particle image velocimetry measurements using deep-sea, remotely operated vehicles. Presented at the APS Meeting Abstracts, p. L33.010.

- Kerfoot, W.C., Budd, J.W., Green, S.A., Cotner, J.B., Biddanda, B.A., Schwab, D.J., Vanderploeg, H.A., 2008. Doughnut in the desert: Late-winter production pulse in southern Lake Michigan. *Limnol. Oceanogr.* 53, 589–604. <https://doi.org/10.4319/lo.2008.53.2.0589>
- Kremien, M., Shavit, U., Mass, T., Genin, A., 2013. Benefit of pulsation in soft corals. *Proc. Natl. Acad. Sci.* 110, 8978–8983. <https://doi.org/10.1073/pnas.1301826110>
- Lassen, J., Kortegård, M., Riisgård, H., Friedrichs, M., Graf, G., Larsen, P., 2006. Down-mixing of phytoplankton above filter-feeding mussels—interplay between water flow and biomixing. *Mar. Ecol. Prog. Ser.* 314, 77–88. <https://doi.org/10.3354/meps314077>
- Lauder, B.E., Spalding, D.B., n.d. THE NUMERICAL COMPUTATION OF TURBULENT FLOWS 21.
- Liao, Q., Bootsma, H.A., Xiao, J., Klump, J.V., Hume, A., Long, M.H., Berg, P., 2009. Development of an in situ underwater particle image velocimetry (UWPIV) system: Underwater PIV. *Limnol. Oceanogr. Methods* 7, 169–184. <https://doi.org/10.4319/lom.2009.7.169>
- Liao, Q., Cowen, E.A., 2005. An efficient anti-aliasing spectral continuous window shifting technique for PIV. *Exp. Fluids* 38, 197–208. <https://doi.org/10.1007/s00348-004-0899-7>
- Liao, Q., Wang, B., Wang, P.-F., 2015. In situ measurement of sediment resuspension caused by propeller wash with an underwater particle image velocimetry and an acoustic doppler velocimeter. *Flow Meas. Instrum.* 41, 1–9. <https://doi.org/10.1016/j.flowmeasinst.2014.10.008>
- Luo, L., Wang, J., Schwab, D.J., Vanderploeg, H., Leshkevich, G., Bai, X., Hu, H., Wang, D., 2012. Simulating the 1998 spring bloom in Lake Michigan using a coupled physical-biological model. *J. Geophys. Res. Oceans* 117. <https://doi.org/10.1029/2012JC008216>
- Mida, J.L., Scavia, D., Fahnenstiel, G.L., Pothoven, S.A., Vanderploeg, H.A., Dolan, D.M., 2010. Long-Term and Recent Changes in Southern Lake Michigan Water Quality with Implications for Present Trophic Status. *J. Gt. Lakes Res.* 36, 42–49. <https://doi.org/10.1016/j.jglr.2010.03.010>
- Mosley, C., n.d. Phosphorus Recycling By Profunda Quagga Mussels in Lake Michigan 104.
- Mosley, C., Bootsma, H., 2015. Phosphorus recycling by profunda quagga mussels (*Dreissena rostriformis bugensis*) in Lake Michigan. *J. Gt. Lakes Res.* 41, 38–48. <https://doi.org/10.1016/j.jglr.2015.07.007>
- Nalepa, T.F., Fanslow, D.L., Lang, G.A., 2009. Transformation of the offshore benthic community in Lake Michigan: recent shift from the native amphipod *Diporeia* spp. to the invasive mussel *Dreissena rostriformis bugensis*. *Freshw. Biol.* 54, 466–479. <https://doi.org/10.1111/j.1365-2427.2008.02123.x>
- Nalepa, T.F., Fanslow, D.L., Pothoven, S.A., 2010. Recent changes in density, biomass, recruitment, size structure, and nutritional state of *Dreissena* populations in southern Lake Michigan. *J. Gt. Lakes Res.* 36, 5–19. <https://doi.org/10.1016/j.jglr.2010.03.013>
- Nayak, A.R., Li, C., Kiani, B.T., Katz, J., 2015. On the wave and current interaction with a rippled seabed in the coastal ocean bottom boundary layer. *J. Geophys. Res. Oceans* 120, 4595–4624. <https://doi.org/10.1002/2014JC010606>
- Nimmo Smith, W., Atsavapranee, P., Katz, J., Osborn, T., 2002. PIV measurements in the bottom boundary layer of the coastal ocean. *Exp. Fluids* 33, 962–971. <https://doi.org/10.1007/s00348-002-0490-z>

- Nishizaki, M., Ackerman, J.D., 2017. Mussels blow rings: Jet behavior affects local mixing: Mussels blow rings. *Limnol. Oceanogr.* 62, 125–136. <https://doi.org/10.1002/lno.10380>
- Pope, S.B., 2000. *Turbulent Flows*. Cambridge University Press, Cambridge. <https://doi.org/10.1017/CBO9780511840531>
- Qualls, T.M., Dolan, D.M., Reed, T., Zorn, M.E., Kennedy, J., 2007. Analysis of the Impacts of the Zebra Mussel, *Dreissena polymorpha*, on Nutrients, Water Clarity, and the Chlorophyll-Phosphorus Relationship in Lower Green Bay. *J. Gt. Lakes Res.* 33, 617–626. [https://doi.org/10.3394/0380-1330\(2007\)33\[617:AOTIOT\]2.0.CO;2](https://doi.org/10.3394/0380-1330(2007)33[617:AOTIOT]2.0.CO;2)
- Quinn, N.P., Ackerman, J.D., 2015. The effect of bottom roughness on scalar transport in aquatic ecosystems: Implications for reproduction and recruitment in the benthos. *J. Theor. Biol.* 369, 59–66. <https://doi.org/10.1016/j.jtbi.2015.01.007>
- Raffel, M., Willert, C.E., Scarano, F., Kähler, C.J., Wereley, S., Kompenhans, J., 2017. *Particle image velocimetry*. Springer Berlin Heidelberg, New York, NY.
- Raffel, M., Willert, C.E., Wereley, S., Kompenhans, J., 1998. *Particle Image Velocimetry: A Practical Guide*. Experimental Fluid Mechanics. <https://doi.org/10.1007/978-3-662-03637-2>
- Riisgård, H.U., Larsen, P.S., 2017. Filter-Feeding Zoobenthos and Hydrodynamics, in: Rossi, S., Bramanti, L., Gori, A., Orejas, C. (Eds.), *Marine Animal Forests*. Springer International Publishing, Cham, pp. 787–811. https://doi.org/10.1007/978-3-319-21012-4_19
- Rowe, M.D., Anderson, E.J., Vanderploeg, H.A., Pothoven, S.A., Elgin, A.K., Wang, J., Yousef, F., 2017. Influence of invasive quagga mussels, phosphorus loads, and climate on spatial and temporal patterns of productivity in Lake Michigan: A biophysical modeling study. *Limnol. Oceanogr.* 62, 2629–2649. <https://doi.org/10.1002/lno.10595>
- Rowe, M.D., Anderson, E.J., Wang, J., Vanderploeg, H.A., 2015. Modeling the effect of invasive quagga mussels on the spring phytoplankton bloom in Lake Michigan. *J. Gt. Lakes Res.*, Complex interactions in Lake Michigan’s rapidly changing ecosystem 41, 49–65. <https://doi.org/10.1016/j.jglr.2014.12.018>
- Shen, C., Liao, Q., Bootsma, H.A., Troy, C.D., Cannon, D., 2018. Regulation of plankton and nutrient dynamics by profundal quagga mussels in Lake Michigan: a one-dimensional model. *Hydrobiologia* 815, 47–63. <https://doi.org/10.1007/s10750-018-3547-6>
- Sheng, J., Meng, H., Fox, R.O., 2000. A large eddy PIV method for turbulence dissipation rate estimation. *Chem. Eng. Sci.* 55, 4423–4434. [https://doi.org/10.1016/S0009-2509\(00\)00039-7](https://doi.org/10.1016/S0009-2509(00)00039-7)
- Smith, W.A.M.N., 2007. 3D Flow Visualization in the Bottom Boundary Layer of the Coastal Ocean, in: *OCEANS 2007*. Presented at the Oceans 2007, IEEE, Vancouver, BC, pp. 1–7. <https://doi.org/10.1109/OCEANS.2007.4449297>
- Sreenivasan, K.R., 1995. On the universality of the Kolmogorov constant. *Phys. Fluids* 7, 2778–2784. <https://doi.org/10.1063/1.868656>
- Stoeckmann, A., 2003. Physiological energetics of Lake Erie dreissenid mussels: a basis for the displacement of *Dreissena polymorpha* by *Dreissena bugensis*. *Can. J. Fish. Aquat. Sci.* 60, 126–134. <https://doi.org/10.1139/f03-005>
- Trowbridge, J.H., 1998. On a Technique for Measurement of Turbulent Shear Stress in the Presence of Surface Waves. *J. ATMOSPHERIC Ocean. Technol.* 15, 9.
- Troy, C., Cannon, D., Liao, Q., Bootsma, H., 2016. Logarithmic velocity structure in the deep hypolimnetic waters of Lake Michigan. *J. Geophys. Res. Oceans* 121, 949–965. <https://doi.org/10.1002/2014JC010506>

- Turschak, B., Bootsma, H., 2015. Lake Michigan trophic structure as revealed by stable C and N isotopes. *J. Gt. Lakes Res.* 41. <https://doi.org/10.1016/j.jglr.2015.04.004>
- van Duren, L.A., Herman, P.M.J., Sandee, A.J.J., Heip, C.H.R., 2006. Effects of mussel filtering activity on boundary layer structure. *J. Sea Res.* 55, 3–14. <https://doi.org/10.1016/j.seares.2005.08.001>
- Vanderploeg, H.A., Johengen, T.H., Liebig, J.R., 2009. Feedback between zebra mussel selective feeding and algal composition affects mussel condition: did the regime changer pay a price for its success? *Freshw. Biol.* 54, 47–63. <https://doi.org/10.1111/j.1365-2427.2008.02091.x>
- Vanderploeg, H.A., Liebig, J.R., Nalepa, T.F., Fahnenstiel, G.L., Pothoven, S.A., 2010. Dreissena and the disappearance of the spring phytoplankton bloom in Lake Michigan. *J. Gt. Lakes Res.* 36, 50–59. <https://doi.org/10.1016/j.jglr.2010.04.005>
- Wang, B., Liao, Q., 2016a. Field observations of turbulent dissipation rate profiles immediately below the air-water interface: NEAR SURFACE STRUCTURES OF TURBULENCE. *J. Geophys. Res. Oceans* 121, 4377–4391. <https://doi.org/10.1002/2015JC011512>
- Wang, B., Liao, Q., 2016b. Field observations of turbulent dissipation rate profiles immediately below the air-water interface: NEAR SURFACE STRUCTURES OF TURBULENCE. *J. Geophys. Res. Oceans* 121, 4377–4391. <https://doi.org/10.1002/2015JC011512>
- Wang, B., Liao, Q., Bootsma, H.A., Wang, P.-F., 2012. A dual-beam dual-camera method for a battery-powered underwater miniature PIV (UWMPIV) system. *Exp. Fluids* 52, 1401–1414. <https://doi.org/10.1007/s00348-012-1265-9>
- Wang, B., Liao, Q., Fillingham, J.H., Bootsma, H.A., 2015. On the coefficients of small eddy and surface divergence models for the air-water gas transfer velocity. *J. Geophys. Res. Oceans* 120, 2129–2146. <https://doi.org/10.1002/2014JC010253>
- Wang, B., Liao, Q., Xiao, J., Bootsma, H.A., 2013. A Free-Floating PIV System: Measurements of Small-Scale Turbulence under the Wind Wave Surface. *J. Atmospheric Ocean. Technol.* 30, 1494–1510. <https://doi.org/10.1175/JTECH-D-12-00092.1>
- Westerweel, J., 1994. Efficient detection of spurious vectors in particle image velocimetry data. *Exp. Fluids* 16–16, 236–247. <https://doi.org/10.1007/BF00206543>
- Westerweel, J., Elsinga, G.E., Adrian, R.J., 2013. Particle Image Velocimetry for Complex and Turbulent Flows. *Annu. Rev. Fluid Mech.* 45, 409–436. <https://doi.org/10.1146/annurev-fluid-120710-101204>
- Westerweel, J., Scarano, F., 2005. Universal outlier detection for PIV data. *Exp. Fluids* 39, 1096–1100. <https://doi.org/10.1007/s00348-005-0016-6>
- Widdows, J., Pope, N.D., Brinsley, M.D., Gascoigne, J., Kaiser, M.J., 2009. Influence of self-organised structures on near-bed hydrodynamics and sediment dynamics within a mussel (*Mytilus edulis*) bed in the Menai Strait. *J. Exp. Mar. Biol. Ecol.* 379, 92–100. <https://doi.org/10.1016/j.jembe.2009.08.017>
- Willert, C.E., Gharib, M., 1991. Digital particle image velocimetry. *Exp. Fluids* 13.

APPENDIX. SELECTED TIME INTERVAL

The selected time intervals were shown below.

	Start time	End time
1	'24-Jul-2018 18:00:00'	'25-Jul-2018 06:00:00'
2	'25-Jul-2018 11:00:00'	'26-Jul-2018 00:00:00'
3	'26-Jul-2018 08:00:00'	'26-Jul-2018 20:00:00'
4	'27-Jul-2018 00:00:00''	'28-Jul-2018 02:00:00'
5	'28-Jul-2018 06:00:00'	'29-Jul-2018 04:00:00'
6	'29-Jul-2018 08:00:00'	'30-Jul-2018 02:00:00'
7	'30-Jul-2018 06:00:00'	'30-Jul-2018 14:00:00'
8	'10-Aug-2018 00:00:00''	'10-Aug-2018 20:00:00'
9	'11-Aug-2018 02:00:00'	'11-Aug-2018 20:00:00'
10	'12-Aug-2018 00:00:00''	'12-Aug-2018 22:00:00'
11	'13-Aug-2018 02:00:00'	'14-Aug-2018 04:00:00'
12	'14-Aug-2018 18:00:00'	'16-Aug-2018 00:00:00'
13	'16-Aug-2018 04:00:00'	'17-Aug-2018 21:00:00'
14	'18-Aug-2018 02:00:00'	'19-Aug-2018 05:00:00'
15	'19-Aug-2018 08:00:00'	'20-Aug-2018 00:00:00''
16	'20-Aug-2018 05:00:00'	'20-Aug-2018 21:00:00'
17	'21-Aug-2018 00:00:00''	'21-Aug-2018 23:00:00'

18	'24-Jul-2018 18:00:00'	'25-Jul-2018 06:00:00'
19	'25-Jul-2018 11:00:00'	'26-Jul-2018 00:00:00''
20	'26-Jul-2018 08:00:00'	'26-Jul-2018 20:00:00'
21	'27-Jul-2018 00:00:00''	'28-Jul-2018 02:00:00'
22	'22-Aug-2018 08:00:00'	'24-Aug-2018 02:00:00'
23	'24-Aug-2018 07:00:00'	'25-Aug-2018 01:00:00'
24	'25-Aug-2018 04:00:00'	'26-Aug-2018 00:00:00''
25	'26-Aug-2018 03:00:00'	'28-Aug-2018 01:00:00'
26	'28-Aug-2018 04:00:00'	'29-Aug-2018 09:00:00'
27	'29-Aug-2018 19:00:00'	'31-Aug-2018 20:00:00'

CURRICULUM VITAE

Name: Tong Jin

Place of birth: Nantong, China

Education:

Ph.D. University of Wisconsin-Milwaukee, Dec. 2019
Major: Civil and Environmental Engineering,

B.S., University of Science and Technology of China, June, 2009
Major: Mechanical Engineering

M.S., University of Science and Technology of China, June, 2012
Major: Mechanical Engineering

Dissertation Title:

Underwater Particle Image velocimetry(PIV) measurement of turbulence over mussel bed in a deep site of Lake Michigan

Publication:

Jin, Tong, and Qian Liao. "Application of large scale PIV in river surface turbulence measurements and water depth estimation." *Flow Measurement and Instrumentation* 67 (2019): 142-152.